Editorial corner – a personal view
Chemical hybridizations of polyurethanes with fillers

B. K. Kim[*]

Department of Polymer Science and Engineering, Pusan National University, Busan 609-735, Korea

Polyurethanes (PUs) are most versatile engineering materials whose properties are closely tailored by the structure-property relationship. This leads to a broad property spectrum including foam, coating, adhesive, sealant, and elastomer with an annual production over 12 million tons. Recently, functionalization or hybridization with reinforcing materials opened up even a broad spectrum with value added products in market.

Among others, waterborne type (WPU) was the first commercialized in late 1980s to reduce the solvent emission. This was done by introducing ionic groups viz. carboxylic or sulfonate groups, and/or nonionic hydrophilic polymer segments such as polyethylene oxide into the PU. When the isocyanate termini of the PU prepolymer (hereafter called IPU) are exposed to water or moisture, unstable carbamic acid is formed. This gives off carbon dioxide to form amine ends which react with the isocyanate termini to make chain extension or cross-linking. Water curable PUs are applied for molding the orthopedic socket and gypsum.

IPUs are the key for chemical hybridization. They are directly reacted with the OH groups of many inorganic and organic fillers such as silica, graphene, clay, starch, gelatin, cellulose etc to form chemical hybrids. Among them, hybrids with sustainable raw materials (starch, gelatin, cellulose etc) become biodegradable. Moreover, fillers carrying multiple OH groups provide the hybrids with multifunctional cross-links which give much higher strength and modulus, especially in rubbery state as compared with the conventional cross-links. The enhanced rubbery modulus augmented the elastic recoil with minimum cyclic hysteresis.

A second way of modification is done by capping the IPU with hydroxyl acrylates, typically hydroxyethylacrylate, which is generally followed by UV curing to render cross-linking or hybrids with inorganic fillers such as fumed silica. Prior to the incorporation, acrylic functionality such as vinyltrimethoxysilane (VTMS) or allyl isocyanate (DOI: 10.1002/pola. 24473) is introduced into the fillers. Silica acted as multifunctional cross-link as well as reinforcing filler to provide over 99% shape fixity and shape recovery with only 1% (DOI: 10.1039/b922775j). The UV curing of PU or WPU synergistically combined the advantages of WPU (tack-free) and UV cure (fast), which is a great advantage for coating applications.

The IPU can directly react with OH groups of fillers to form hybrids (DOI: 10.1039/c1jm10722d). Or, the IPU can be end capped with glycidol to introduce epoxy groups on the termini, which are subsequently reacted with 3-aminopropyltriethoxysilane (APTES) to form APTES extended PU. The ethoxy groups react with OH groups of fillers via sol-gel type reactions to form chemical hybrids (DOI: 10.1039/b816691a). In both cases, fillers act as multifunctional cross-links and reinforcement. Novel PUs are yet to come with multiple hybridization and functionalization along with non-isocyanate route.

Prof. Dr. Byung Kyu Kim
Member of International Advisory Board

[*]Corresponding author, e-mail: bkkim@pnu.edu

Plane-interface-induced lignin-based nanosheets and its reinforcing effect on styrene-butadiene rubber

C. Jiang, H. He, P. Yu, D. K. Wang, L. Zhou, D. M. Jia*

Department of Polymer Materials and Engineering, South China University of Technology, Guangzhou 510640, People's Republic of China

Abstract. Lignin was viewed as a spherical microgel in aqueous alkali. While spread out in a monolayer or adsorbed on a surface, lignin was made up of flexible, disk-like molecules with approximately the same thickness of 2 nm. According to this principle, we employed the lamina of montmorillonite (MMT) as a plane template to anchor cationic lignin (CL) on its two sides, resulting in the formation of CL-MMT hybrid materials (CLM). The isotherm adsorption behavior and structure characteristics of CLM were studied. The results showed that CLM was individually dispersed nanosheets with a thickness of about 5 nm when the mass ratio of CL to MMT is more than 2:1 and prepared at acidic or neutral pH. Compared to the co-coagulation of lignin and styrene-butadiene rubber (SBR), CLM obviously accelerated the coagulation rate, due to the reduction of surface activity of CL restricted by MMT. The nanoscale dispersion of CLM in SBR matrix significantly improved the tensile strength of CLM/SBR nanocomposites to 14.1 MPa by adding only 10 phr CLM and cardanol glycidyl ether (CGE) as compatibilizer. Dynamic mechanical analysis (DMA) showed that the glass transition temperature of SBR/CLM nanocomposites decreased with increasing CLM loading. Correspondingly, a special interfacial structure was proposed.

Keywords: *nanomaterials, lignin, montmorillonite, complete exfoliation, nanosheets*

1. Introduction

Lignin is the most abundant renewable aromatic biopolymer on earth, widely existing in the cell walls of all high-level plants. It mainly consists of three phenylpropanoid units such as p-hydroxyphenyl, guaiacyl and syringyl, which are attached to one another by a series of characteristic linkages (β-O-4, β-5, β-β, etc.) [1, 2]. Traditionally, lignin has been viewed as a waste material or a low value byproduct of pulp and paper industry, primarily used as fuel due to its high energy content. Only a small proportion is utilized for high value-added products [3]. As emerging biorefinery industries continue to evolve, lignin utilization will become significantly more important. Unfortunately, the heterogeneity of chemical structure of lignin seems to be a persistent challenge to fully realize the potential of lignin [4], although the complex molecule structure and various chemical functional groups (ether linkages, aliphatic and aromatic hydroxyl groups), render lignin lots of functionalities such as hydrophobicity, reinforcing effect, biodegradability and UV-adsorption [5, 6]. To address this issue and maximize the value of lignin-based products, it will be an effective strategy to develop nanostructured lignin or lignin-based nano-materials.

Nanostructured materials have attracted a great deal of attentions in the past decades, owing to their fascinating properties and potential applications in polymer composites [7], electrochemical energy storage and conversion [8], catalysis [9], sensor [10] and drug delivery [11]. Therefore, it will be a promising way to convert amorphous and strongly self-aggregated lignin into some nanostructured materials,

---

*Corresponding author, e-mail: pshuihe@scut.edu.cn

giving us more chances to exploit novel functional applications based on lignin. Actually, earlier studies have demonstrated that lignin dissolved in some solvents possesses a nanostructure, but the shape and size intensively depend on the chosen solvent and analytical methods [12]. It is rather difficult to get a general picture of the exact shape and the actual size of an isolated lignin particle. In addition, there are strong hydrogen bonding interactions [13, 14] and π-π interactions [15] in lignin molecules, thereby resulting in serious thermally irreversible aggregation when lignin is recovered from solutions. As a consequence, it is rather difficult to obtain nanostructured lignin. To date, just few literatures on nanostructured lignin or lignin-based nanomaterials were reported. For example, Hector M Caicedo and coworkers adopted alumina membranes as a sacrificial template to prepare lignin-based nanotubes, in which lignin was transformed into nanotubes with a wall thickness of approximately 15 nm or nanowires with a nominal diameter of 200 nm [16]. Moreover, Jonathan Spender *et al.* [17] reported an extended ice-segregation-induced self-assembly methodology to produce carbon nanofibers (CNFs) with a diameter of less than 100 nm. Besides above-mentioned one-dimensional (1D) lignin-based nanotubes and nanofibers, zero-dimensional (0D) lignin nanoparticles or lignin-based carbon nanoparticles are also successfully prepared via kinds of strategies [18–20]. However, to our knowledge, there is no report on successful synthesis of two-dimensional (2D) lignin nanosheets so far. In this paper, we present a novel approach to prepare 2D lignin-based nanosheets by using montmorillonite (MMT) as a plane template. Montmorillonite, a naturally occurring layered clay, consists of stacks of platelets obtained by combining two tetrahedral silica layers with Mg or Al to form an octahedral metal oxide structure [21]. Each platelet (about 0.96 nm thick) is separated from the next by interlayer cations (Na^+, K^+, Ca^{2+} …), which can be easily replaced by other organic cations, thereby providing an essential way to introduce different functional groups so that design materials with required structure and performance [22–26]. Generally, MMT is used as a reinforcing filler to promote the mechanical, thermal and barrier properties of polymer, which essentially depend on the degree of interaction or exfoliation of MMT within polymer matrix [27, 28]. However, it is very difficult to obtain completely exfoliated MMT via a simple procedure. Especially in nonpolar polymer matrix, very few efforts have been made to obtain highly exfoliated MMT [29].

Commonly, lignin in solution is assumed to be an approximately spherical microgel between that of an Einstein sphere and a linear nonfree-draining random coil with different hydrodynamic sizes from several nanometers to several hundred nanometers [13]. While spread out in a monolayer or adsorbed onto a surface, lignin is envisaged as being made up of flexible, disk-like molecules having various shapes and sizes but all with approximately the same thickness of 2 nm [30]. Herein, because of the huge aspect ratio of MMT platelets, we employed MMT as a plane template and CL as adsorbate to exchange the layer cations of MMT. To our surprise, MMT was completely exfoliated and a large amount of CL as disk-like spots with a thickness of about 2 nm was anchored on the surface of MMT platelets, resulting in the formation of individually dispersed CL-decorated MMT (CLM) nanosheets with different surface charge status in aqueous solution. We successfully fabricated 2D lignin-based nanosheets for the first time by the template of MMT, thus providing a versatile and promising way to prepare high value-added lignin products with potential applications in reinforcement for polymer as nano-filler via latex compounding, universal building blocks for UV absorption through simple drop-coating method, etc. To elucidate one of its applications, we incorporated the resulting CLM into SBR via latex co-coagulating method. The morphology, mechanical and dynamic mechanical properties of the CLM/SBR composites and the interface structure between CLM and SBR matrix were investigated in detail.

2. Materials and methods
2.1. Materials
Lignin (industrial sulfate lignin), with an average molecular weight (M_W) of 3801 and polydispersity index of 2.15, was purchased from Tralin Paper Co., Ltd. (Shandong, China). Na^+-MMT, with a cationic exchange capacity of 100 meq/100 g, was supplied by Nanhai Inorganic Factory (Guangdong, China). Sodium hydroxide (NaOH), hydrochloric acid (HCl) and sulfuric acid (H_2SO_4) were analytical grade, purchased from Guangzhou Chemical Reagent Factory, China. The reagents for synthesis of CL including epichlorohydrin (98%) and trimethylamine water solution (33%) were obtained from Lingfeng Chemi-

cal Reagent (Shanghai, China) and used as received. Deionized water (resistivity >18 MΩ·cm) was obtained from a Millipore water purification system. SBR latex (intex 132, solid content 65 wt%) was purchased from Shanghai Nessen international Trading Co., Ltd. Cardanol glycidyl ether (CGE) was kindly provided by Shanghai Meidong biological material co., Ltd.. All the rubber ingredients were industrial grade and used as received.

2.2. Synthesis of cationic lignin

Prior to use, lignin was purified by a repetitive alkali-dissolving-acid-precipitating method as previously described [31]. Subsequently, CL was synthesized according to the previous procedure [32, 33]. In a typical experiment, trimethylamine (60 mmol) was added into equimolar HCl solution to convert to a salt form, then dropwise added epichlorohydrin (50 mmol) and reacted at 52°C for 4 h to obtain glycidyltrimethylammonium chloride. After that, lignin (10 g) was dissolved in 100 mL of 1 M NaOH solution, and the pre-synthesized glycidyltrimethylammonium chloride was added to the lignin solution. The reaction mixture was stirred at 52°C for 19 h. Finally, the resultant CL was recovered by precipitation in 2 L ethanol solution (95%) and washed with diethyl ether, followed by drying in a vacuum oven at 50°C for 24 h. By employing a colloid titration method described by Ueno and Kina [34], the charge density of CL at pH = 2, which can be used for analyzing the mechanism of ion-exchange reaction, was measured to be 1.03 meq/g CL.

2.3. Synthesis of CLM hybrid materials

CL solutions containing 0.05, 0.1, 0.2 and 0.4 g of CL in 25 mL deionized water were slowly added into a 2% MMT suspension (0.5 g of Na^+-MMT in 25 mL of deionized water) to obtain hybrid materials with initial CL-MMT mass ratios of 0.1:1, 0.2:1, 0.4:1 and 0.8:1, respectively. For the preparation of CLM with CL-MMT mass ratio of 2:1, 4:1, 6:1 and 8:1, CL solutions with 1 g of CL in 125 mL, 2, 3 and 4 g in 250 mL respectively, were mixed with the MMT suspension. In order to investigate the effect of pH on the adsorption of CL to MMT, three groups of CL-MMT solutions with all CL-MMT mass ratios were prepared in total. The pH of the three groups was adjusted to 12, 7 and 3 by adding a few drops of 0.1, 0.01 or 0.001 N HCl/NaOH solutions, respectively. Subsequently, the CL-MMT solutions were

stirring at 50°C for 48 h. The resulting solutions were filtrated through a nylon membrane (0.22 μm) and washed with deionized water of corresponding pH. The filtrate was collected for determination of the adsorbed amount of CL on MMT. The purified supernatants, namely CLM hybrid materials, were centrifuged at 4000 rpm to exclude the un-exfoliated and un-suspended part, then vacuum dried at 50°C and ground to powder or redispersed in deionized water of corresponding pH for further analysis.

2.4. Determination of adsorbed amount of CL on MMT

The adsorbed amount of CL was estimated from the difference in the initial CL mass and the mass in the filtrate. The amount of CL in filtrate was determined with a UV756CRT UV-vis spectrophotometer (Shanghai Youke Instrument CO. Ltd., China) using a calibration curve, which was obtained from measurements of five samples of CL diluted in 0.01 M HCl to different concentrations at 277 nm. The absorption coefficient for CL was determined to be $13.47 \, L \cdot g^{-1} \cdot cm^{-1}$.

2.5. Preparation of CLM/SBR composites

SBR latex was first diluted with deionized water to a solid content of about 10 wt% and then adjusted the pH to 7. A desired amount of CLM suspensions with pH of 7 was added into SBR latex and the mixture subsequently was coagulated by adding $CaCl_2$ (2 wt%). The co-coagulated compounds were washed with deionized water and vacuum dried over night at 50°C. Then the dried compounds were compounded with rubber ingredients with a two-roll mill and subjected to compression at 150°C for the optimum curing time determined by the U-CAN UR-2030 vulcameter. The composite that contained 2 phr CLM was abbreviated as S-CLM-2. The meanings of other codes were deduced by analogy. The formulation of the composite is listed as follow, SBR 100 phr; zinc oxide 5 phr; stearic acid 1 phr; N-tert-butyl-2-benzothiazole sulfonamide 1 phr; dibenzothiazole disulfide 1.5 phr; sulfur 1.5 phr. In addition, 2 phr CGE was used as compatibilizer. Note that phr refers to parts per hundred of rubber.

2.6. Characterizations

Zeta potential and dynamic light scattering (DLS) were performed on a 90 Plus Particle Size Analyzer (Brookhaven Inst., Huntsville, NY, USA). Sample

solution was diluted to the appropriate concentration with deionized water of corresponding pH. For DLS, each analysis lasted for 180 s and was performed at 25°C with angle detection of 90°. Zeta potential of CLM and CL was determined by dipping a palladium electrode in sample solution. All the measurements were repeated 3 times and the average value was reported.

X-ray diffraction (XRD) experiments were conducted at ambient temperature on a Rigaku Dmax/III diffractometer (Rigaku Corporation,Tokyo, Japan) using a Cu Kα radiation (λ = 1.54 Å). The generator was operated at 40 kV and 30 mA. The samples were scanned from 2 to 10°, with a step length of 0.02°.

The microstructure and morphology of CLM, CL and SBR/CLM composites were visualized by a Hitachi H-7650 transmission electron microscope (TEM) at an accelerating voltage of 80 kV. The samples for TEM measurement were prepared by dropping sample solution or by ultramicrotome technology on Cu grids of 200 meshes.

The surface characteristics of CLM and CL were studied on a Multimode Pico-Force Atomic Force Microscopy (AFM, Veeco Instruments Inc., Santa Barbara, CA). All images were obtained using the tapping mode in air at ambient temperature. Real time scanning was performed with scan rates around 1.0 Hz, scan angle 0°, and tapping frequencies ranging from 270 to 320 kHz. The samples were prepared by depositing the suspensions on freshly-cleaved mica surface and drying at room temperature.

Glass transition temperatures of CL, lignin and CLM were measured by differential scanning calorimeter (DSC, TA Instruments Q2000) using 3–5 mg samples in aluminum pans at a heating rate of 10 °C/min from 30C to 250°C.

Thermogravimetric analysis (TGA) was performed under nitrogen atmosphere with a TG 209 F1 (NETZSCH Company, Germany) at a heating rate of 10 °C/min.

Scanning electron micrographs (SEM) of the composites were taken with a Nova NanoSEM 430 instrument (FEI, Netherlands) at an acceleration voltage of 10 kV. The fracture surface was obtained by splitting bulk sample being quenched in liquid nitrogen. Before the observation, a thin gold was evaporated on the fractured surface.

Dynamic mechanical analysis (DMA) spectra of the samples were obtained by using a DMA 242D

dynamic mechanical analyzer (NETZSCH Company, Germany). The specimens with the size of 30 mm×6 mm×2 mm were analyzed in tensile mode at a constant frequency of 1 Hz, a strain of 0.5%, and a temperature range from –100 to 100°C at a heating rate of 3°C/min.

Tensile tests were performed with U-CAN UT-2060 (Taiwan) instrument, according to ISO standard 37-2005 at 25°C.

3. Results and discussion

A wealth of studies on adsorption of polymer by clay, including positively charged, negatively charged and neutral polymer, has revealed distinct adsorption processes for the three types of polymer [35]. Actually, as shown in Figure 1, the CL we synthesized is a zwitterionic polymer and simultaneously possesses quaternary ammonium cations and ionizable anionic groups such as carboxylic groups ($pK_{COOH} < 4.75$) and phenolic hydroxyls ($pK_{OH} \approx$ 10.5–11) [36], conferring a special property of tunable charge status to CL by changing pH. Considering that carboxylic groups and phenolic hydroxyls of CL are completely ionized at pH of 12 whereas phenolic hydroxyls are protonated at pH of 7 and only quaternary ammonium cations remain at pH of 3, we prepared CLM hybrid materials at this three pH values to investigate the effect of pH on adsorption process and degree of exfoliation of MMT. It is worthy to note that the CLM are denoted with the initial CL-MMT ratio employed in their preparation; nevertheless, such a ratio does not indicate the final CL amount adsorbed on MMT.
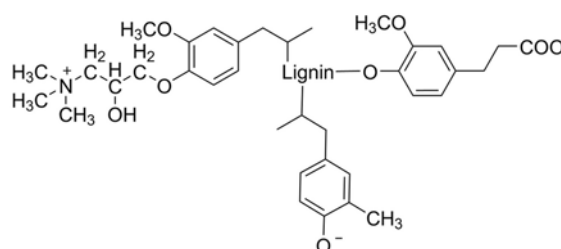

Figure 1. The possible chemical structure of CL

3.1. Adsorption isotherms

The adsorption isotherms at 50°C from CL solutions of three different pH onto MMT are presented in Figure 2. The data sets were fitted to the Langmuir Equation (1) using a nonlinear curve fitting program [37]:
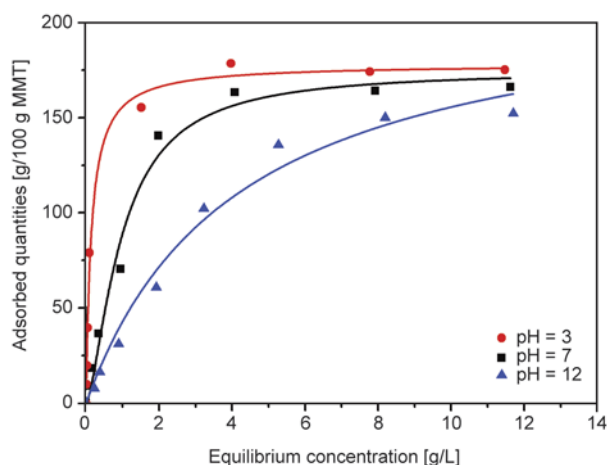
Figure 2. Adsorption isotherms of CL on MMT at different pH, in an aqueous dispersion at 50°C

$$\Gamma = \frac{bQC_e}{1 + bC_e} \qquad (1)$$

where Γ is the adsorbed amount of CL, b is the affinity constant between CL and clay interaction sites, C_e is the equilibrium CL concentration and Q is the maximum adsorbed amount. As shown in Figure 2, the good fitting curves of the three adsorption isotherms display distinct adsorption processes with different initial slopes, indicating the different affinities between CL and MMT. The affinity constant b from the fitting data were 0.23 ± 0.04 g$^{-1}\cdot$L for pH = 12, 1.04 ± 0.25 g$^{-1}\cdot$L for pH = 7 and 6.95 ± 1.01 g$^{-1}\cdot$L for pH = 3. The gradually increasing affinity constant from pH of 12 to 3 is indicative of the increase in the interactions between CL and MMT with decreasing pH. It can be ascribed to the fact that the anionic groups of CL are protonated and the net charges change from negative to positive with decreasing pH, providing intensively electrostatic interactions between CL and negatively charged MMT platelets, which can be confirmed by the zeta potential of CL in Table 1. For ionic species, b can be related to the Gibbs free adsorption energy ΔG_{ads} through the relation $K = (b\rho/4)^2$ where ρ is the ratio of the solvent (water) density to its molecular weight, $\rho \approx 55.6$ mol$\cdot$L^{-1}, as shown by Equation (2) [38]:

$$\Delta G_{ads} = -RT\ln K \qquad (2)$$

where R is the gas constant and T is the adsorption temperature. Since the positive charge amount of CL was determined to be 1.03 meq/g CL by colloid titration method, the affinity constants between quaternary ammonium cations on CL and negatively charged sites in MMT at the three pH were still the above values by calculation. Consequently, the Gibbs free adsorption energies for quaternary ammonium cations of CL onto MMT at pH of 12, 7 and 3 were -43.34, -51.45 and -61.65 kJ$\cdot$mol^{-1} respectively. Such a high Gibbs free adsorption energy at pH of 3 is comprehensible due to the strong coulombic interactions, whereas a relatively high Gibbs free adsorption energy at pH of 12 existing in an electrostatic repulsion system ($\zeta_{CL} = -19.8\pm2.0$ mV and $\zeta_{MMT} = -32.3\pm3.5$ mV, Table 1) may be ascribed to other strong interactions between CL and MMT except coulombic interactions or other reasons, which will be further discussed in the following text.

Additionally, the maximum adsorbed amount of CL onto MMT at pH of 12, 7 and 3, are 152.1, 175.6 and 177.3 g per 100 g of MMT respectively, which are much more than the estimated maximum adsorbed amount of CL, 97.1 g/100 g MMT. The excess of CL adsorbed onto MMT provides CLM hybrid materials with enough electrostatic repulsion force to sta-
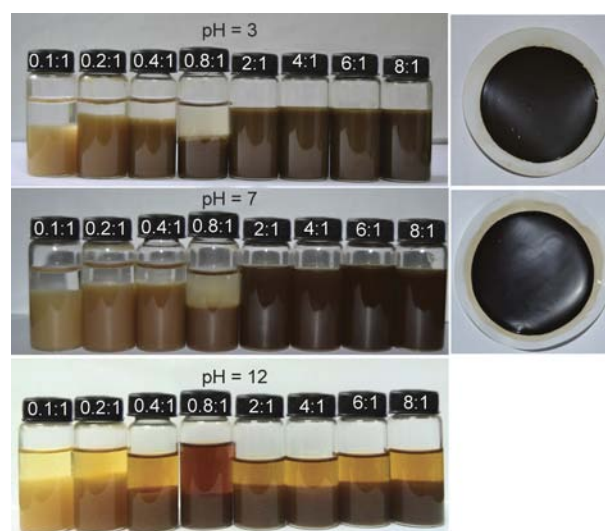

Figure 3. Digital photographs showing the suspensions of CLM hybrid materials in aqueous solutions at pH = 3, 7 and 12 (left) and the corresponding CLM papers with mass ratio of 2:1 (right)

Table 1. The zeta potential and hydrodynamic diameters by DLS of MMT, CL and CLM at pH of 3, 7 and 12

Sample	MMT	CL			2:1 CLM		
		pH = 3	pH = 7	pH = 12	pH = 3	pH = 7	pH = 12
Zeta potential, ζ [mV]	-32.3 ± 3.5	$+14.6\pm3.5$	-5.3 ± 1.3	-19.8 ± 2.0	$+33.5\pm0.9$	-35.9 ± 2.7	-40.4 ± 5.3
Hydrodynamic diameter, D [nm]	642 ± 31	179 ± 4	179 ± 4	240 ± 1	286 ± 2	431 ± 19	300 ± 3

bly disperse in aqueous solution, which can also be verified by the zeta potential of CLM in Table 1 and be visualized in Figure 3. The CLM suspensions with a mass ratio < 2:1 or prepared at alkaline pH undergo sedimentation after 48 h, whereas the CLM suspensions with a mass ratio ≥ 2:1 prepared at acidic and neutral pH are stable. Furthermore, the stable CLM suspensions can build a paper material just by vacuum filtration (Figure 3, right), implying structure change of CLM hybrid materials.

3.2. Structure and morphology of CLM

The degree of exfoliation or intercalation of MMT is usually characterized by XRD. The XRD patterns of MMT, CL and CLM hybrid materials prepared at different pH are shown in Figure 4. The diffraction peaks of MMT prepared at pH of 3, 7 and 12 are located at $2\theta = 5.85$, 5.91 and 7.14°, respectively corresponding to basal spacing d_{001} of 1.24, 1.49 and 1.50 nm calculated by the Bragg equation. It can be observed that no diffraction peak appears in the sample of CL, thereby having no effect on the detection of XRD for CLM hybrid materials. In the XRD patterns of the CLM with mass ratios of 0.1:1 and 0.2:1 prepared at pH of 7 and 3, weak and broad peaks appear at lower angles corresponding to $d_{001} = 1.53–1.57$ nm, indicating the slight intercalation of

CL into the interlayer gallery of MMT. Taking account of the thickness of MMT platelets (0.96 nm), the interlayer distances (Δd) of those CLM are 0.57–0.61 nm, which roughly represents the layer thickness of CL intercalated into MMT. Such small layer thicknesses of CL imply very low M_W for the intercalated CL. However, it is widely recognized that the small chain length polycations in a polydisperse mixture may be displaced by high M_W polycations [35]. Hence, when the mass ratio increases to 1:1 (near stoichiometric point), the high M_W CL replaces the low M_W CL, giving the CLM larger d_{001} of 2.89–3.66 corresponding to $\Delta d = 1.93–2.70$ nm, which coincides with the thickness of one layer of disk-like lignin flat on solid surface as mentioned above (about 2 nm). Continuing to increase the mass ratio in the pH = 7 and 3 systems, no obvious peak is found in the 2θ range from 2° (corresponding to $d_{001} = 4.41$ nm) to 10°, implying possible exfoliation of MMT or basal spacing larger than 4.41 nm. For the CLM prepared at pH of 12, XRD results show an intercalated structure for the CLM and the basal spacing increases with increasing the mass ratio of CL to MMT. The basal spacing is mainly divided into two parts: low M_W CL intercalated d_{001} (1.38–1.57 nm, corresponding to $\Delta d = 0.42–0.61$ nm) and high M_W CL intercalated d_{001} (1.94–3.94 nm, corre-
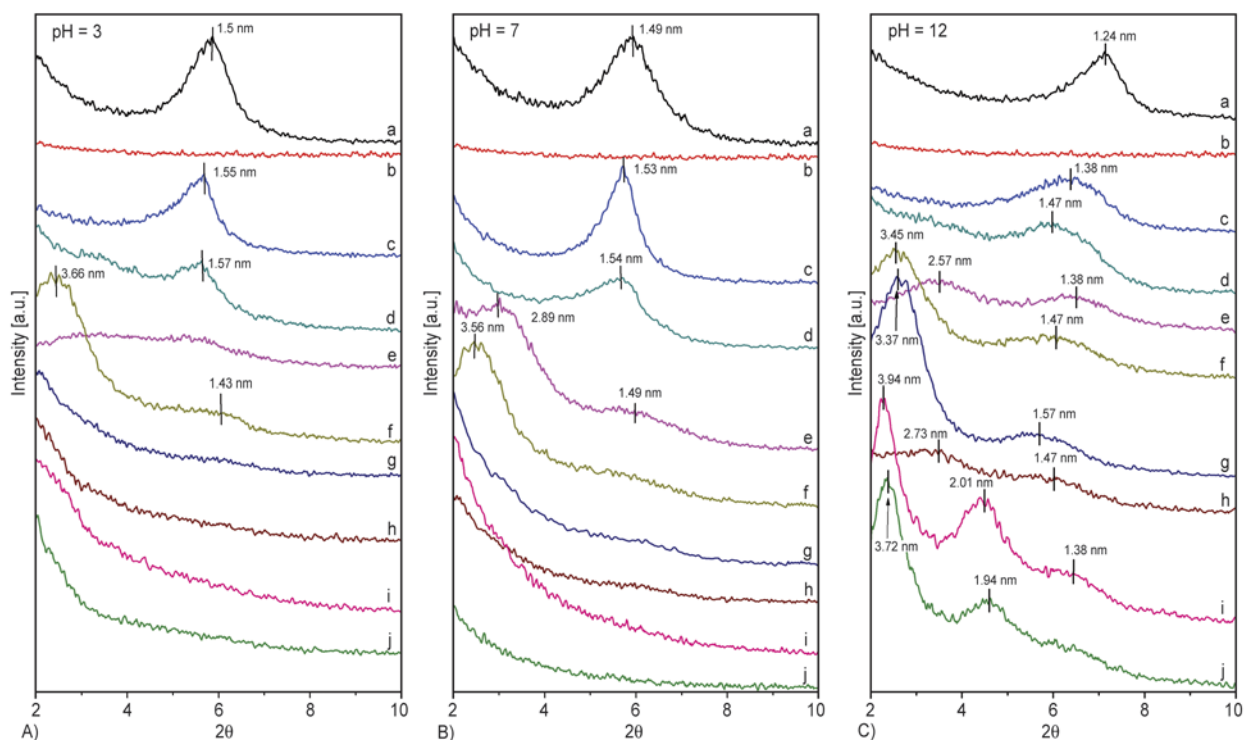

Figure 4. XRD patterns of (a) MMT, (b) CL and CLM hybrid materials with CL-MMT mass ratio of (c) 0.1:1, (d) 0.2:1, (e) 0.4:1, (f) 0.8:1 (g) 2:1, (h) 4:1, (i) 6:1 and (j) 8:1, prepared at pH of (A) 3, (B) 7 and (C) 12
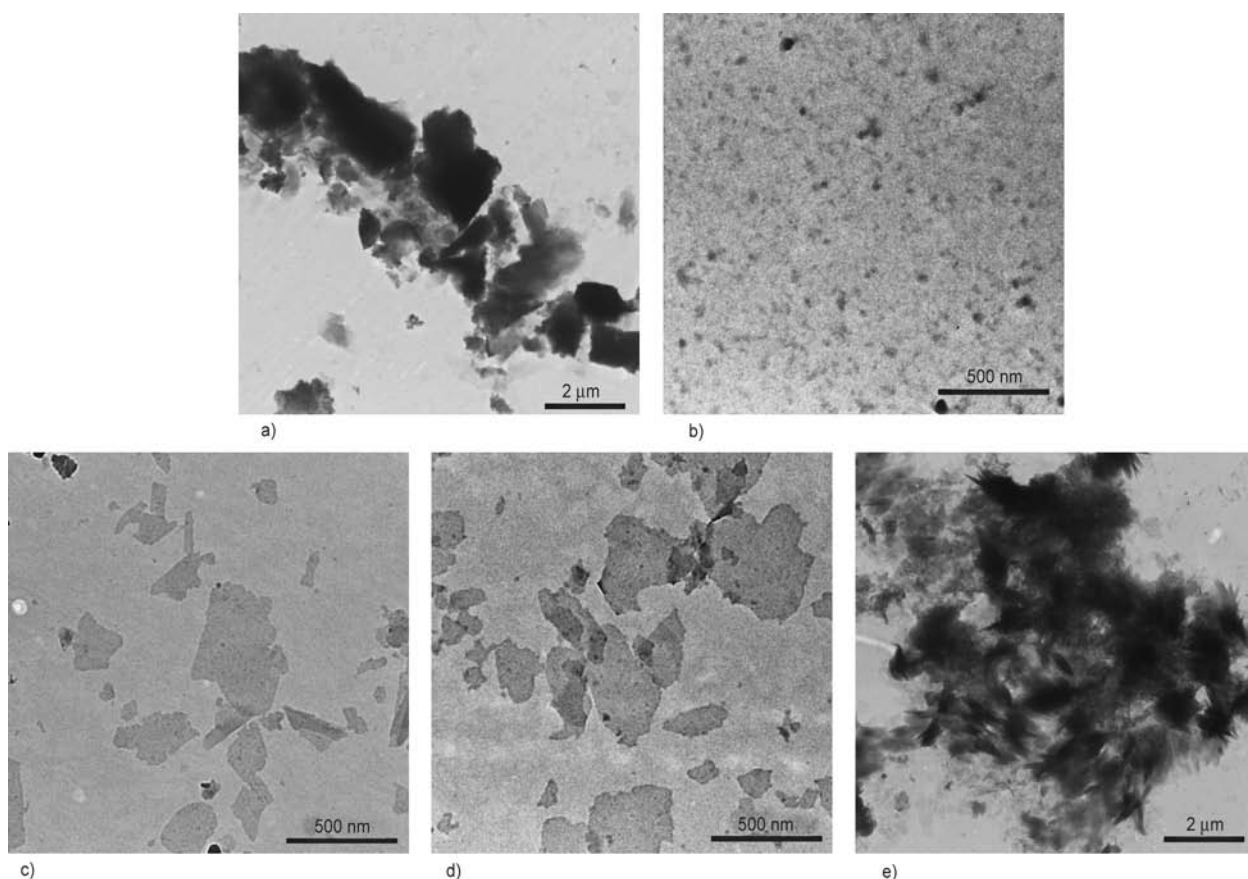
Figure 5. TEM images of (a) pristine MMT, (b) CL and CLM with mass ratio of 2:1 prepared at pH of (c) 3, (d) 7 and (e) 12

sponding to Δd = 0.98–2.98 nm). On the basis of the XRD results, the structure of CLM is tunable by adjustment of pH and the mass ratio of CL to MMT. Owing to the limitation of detection range of XRD measurements, basal spacing larger than 4.41 nm or fully exfoliated structure cannot be found. To further reveal the structure of CLM hybrid materials, TEM and AFM measurements are employed. As shown in Figure 5a, MMT forms dense tactoids without any exfoliation once drying. CL displays a spotted structure with a diameter less than 100 nm (Figure 5b), which is very different from the hydrodynamic diameter of CL in aqueous solution obtained from DLS measurement (Table 1). It is reasonable to believe
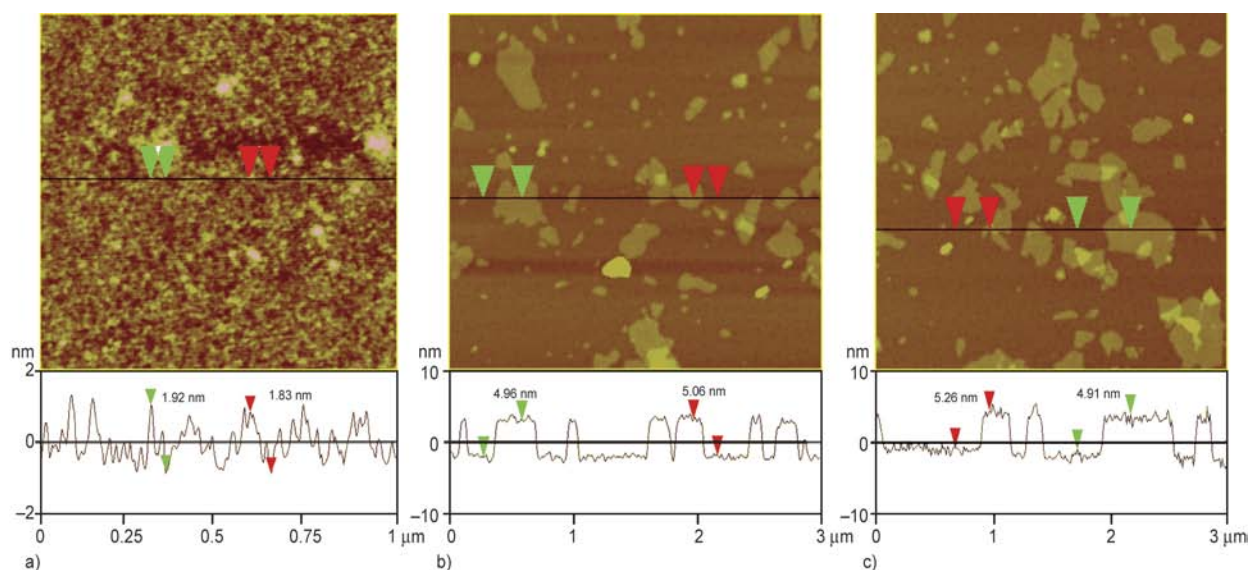
Figure 6. Representative AFM height images and corresponding thickness analysis of (a) CL and CLM with mass ratio of 2:1 prepared at pH of (b) 3 and (c) 7

that CL as swollen spherical polyelectrolyte in aqueous solution will seriously shrink once drying. Moreover, from the AFM height image of CL, the thickness of CL granules is about 2 nm (Figure 6a), indicating the disk-like conformation of CL on solid surface. In comparison to pristine MMT, the CLM hybrid materials with mass ratio of 2:1 prepared at pH of 3 and 7 are individual dispersed irregular lamellas on carbon film with lateral dimension of about several hundred nanometers (Figure 5c and 5d). On the lamellas surface, a large amount of obscure CL spots can be found. In addition, from the AFM height images of the CLM with a mass ratio of 2:1 prepared at pH of 3 and 7, the thickness of the CLM sheets is about 5 nm (Figure 6b and 6c), which is approximately equal to the combined thickness of one MMT platelet and two disk-like CL layers. The same results are also found in the CLM with mass ratio ≥ 2:1 prepared at pH of 3 and 7. Hence, combined with the results of TEM and AFM measurements, we can sufficiently confirm that MMT can be completely exfoliated into individually dispersed nanosheets as plane templates to anchor two layers of disk-like CL, when the CLM hybrid materials with mass ratio ≥ 2:1 are prepared at pH of 3 and 7. In Figure 5e, it can be seen that the CLM with a mass ratio of 2:1 prepared at pH of 12 exhibits swollen morphologies, indicating that CL is trapped in the MMT interlayer galleries to form an intercalated structure. Overall, the TEM and AFM observations are highly consistent with the above XRD results.

3.3. Adsorption mechanism and interactions between CL and MMT

The schematic illustration of adsorption mechanism and interactions between CL and MMT are depicted in Figure 7. It is generally accepted that little adsorption and no intercalation into clay interlayer galleries occur with negatively charged polymer due to the initial electrostatic repulsion between the polymer and clay surface [39]. In our investigated systems, the intercalated structure of the CLM prepared at pH of 12 seems to be at odds with the theoretical expectation. It may imply some special interactions between CL and MMT. Beall and Gross [40] reported that ion-dipole interactions could drive organic compounds with partial negative charges into MMT interlayer galleries. This phenomenon was also observed by Dang in the system of silk fibroin and MMT [41]. Although many polar groups in CL can interact with the interlayer cations via ion-dipole interactions, we propose that stronger noncovalent interactions, cation-π interactions between the interlayer cations and aromatic rings of CL, are dominant driving force for the adsorption of negatively charged CL onto MMT. Cation-π interactions are of the strongest noncovalent interactions and operate over van der Waals distances (instead of typical ion-dipole distances). Typically, water soluble cations have greater interaction energy with benzene rings than with water [42]. Since the intercalation of negatively charged organic molecules into MMT interlayer galleries can be realized via ion-dipole interactions, the stronger cation-π inter-
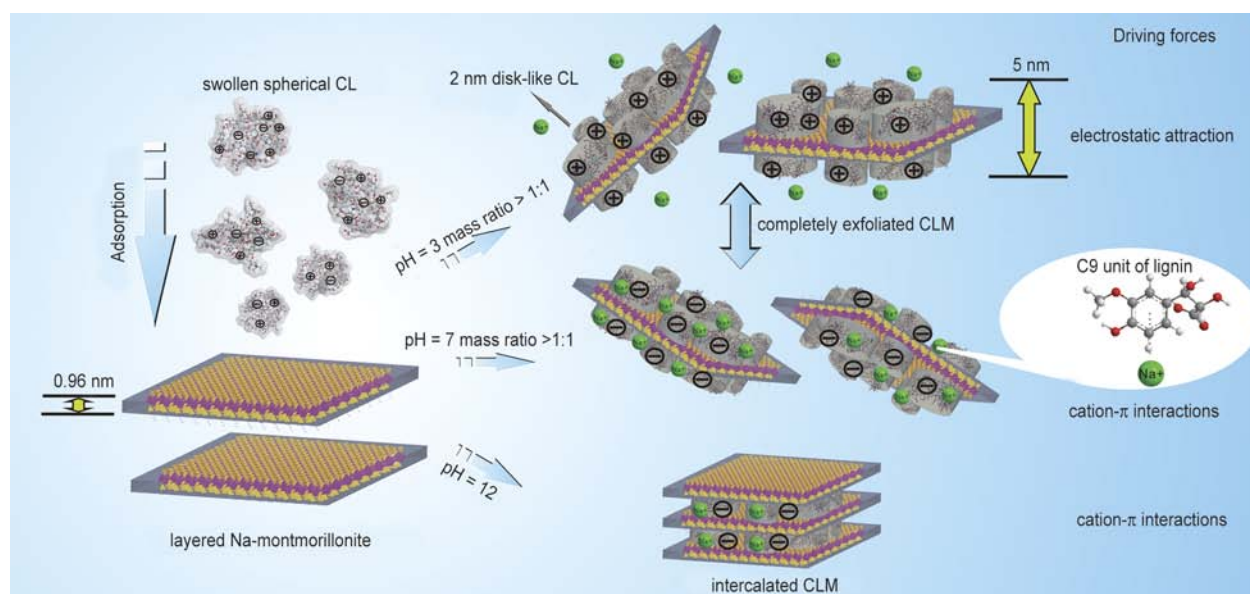

Figure 7. Schematic illustration of adsorption mechanism and interactions between CL and MMT

actions should be more responsible for the intercalated structure of the CLM hybrid materials prepared at pH of 12. On the other hand, because of the polydispersity of lignin molecules, low M_W lignin has a relatively small amount of anionic groups and thus the synthesized CL with low M_W has a relatively large amount of positive charges in return. At high pH, some low M_W CL molecules are even positively charged, which are easier to interact with MMT and enter into MMT interlayer galleries via electrostatic attractive interactions or cation-π interactions. However, the intercalation by low M_W CL just results in relatively small expansion in basal spacing. The larger basal spacing and even the exfoliated structure must arise from the intercalation of high M_W CL via cation-π interactions. Nonetheless, low M_W CL must firstly enter the MMT interlayer galleries to enlarge the interlayer distance for the subsequent entrance of high M_W CL via cation-π interactions. Disappointingly, only intercalated structure is achieved at pH of 12 for all investigated mass ratios. This can be attributed to weak attractive interactions between natively charged MMT and CL, which cannot completely overcome the electrostatic repulsion at such high pH. However, cation-π interactions are more remarkable for the CLM prepared at pH of 7, which results in an exfoliated structure. Although the CL at pH of 7 exhibits a nearly electroneutral polymer (–5.3±1.3 mV, Table 1), the CLM with mass ratio of 2:1 prepared at pH of 7 has a zeta potential of –35.9±2.7 mV, which is just a little bit lower than that of pristine MMT (–32.3±3.5 mV, Table 1), demonstrating that the CL adsorbed onto the MMT platelet surfaces exhibits much more electronegativity. It can be explained as below: the nearly electroneutral CL has the lower electrostatic repulsion towards MMT. As a result, the positively charged sites of CL are able to approach MMT platelets to balance the negatively charged sites at MMT platelet surfaces. Simultaneously, the interlayer cations of MMT can bond to the aromatic rings of CL via cation-π interactions to compensate the negative charges of CL. In this way, the electrostatic repulsion between the MMT and negatively charged CL is inhibited to avoid desorption of CL from MMT. For the CLM prepared at pH of 3, the CL is positively charged at such pH and can interact with negatively charged MMT via electrostatic attractive interactions. As electrostatic attractive interactions are stronger than cation-π interactions, the affinity

constant and Gibbs free adsorption energy at pH of 3 are highest. Additionally, on basis of the results of DLS and AFM measurements for CL, the conformation of CL molecules changes from extended spherical microgel with a mean hydrodynamic diameter of about 200 nm to disc -like sheet with a thickness of about 2 nm, when CL adsorbed onto MMT. This conformation change can provide entropy gain to drive the adsorption of CL onto MMT. Overall, the repulsion interactions decrease gradually and the attractive interactions become stronger with decreasing pH, resulting in stronger adsorption of CL onto MMT and different charge status.

3.4. Glass transition behavior
Further information can be estimated from the glass transition temperature (T_g) of CLM hybrid materials (Figure 8). Compared to the T_g of lignin (170°C), CL has a higher T_g of 211°C due to strong intramolecular cation-π interactions between quaternary ammonium cations and aromatic rings in CL macromolecules. For CLM hybrid materials, the thermal transition behavior of CLM is mainly originated from the segment motion of CL molecules, which can be completely confined by MMT platelets only if the interaction between CL and MMT platelets is strong enough. Beall *et al.* reported that there are three regions around the clay platelets: the surface modifier region, the constrained polymer region, and the unconstrained polymer region. The surface modifier region is about 1–2 nm, while the constrained polymer region may extend 50–100 nm away from the clay platelet surface [43]. Therefore, DSC does not detect any traces of thermal transitions for the CLM with a complete exfoliated structure, where the motion of disk-like CL with a thickness of about 2 nm is completely constrained by MMT platelets (i.e., the DSC curves of the CLM with mass ratio ≥2:1 prepared at pH of 7 and 3). Similarly, the neatly intercalated CLM should have no thermal transition since the intercalated distance is usually less than the constrained polymer region. Obviously, the CLM prepared at pH of 12 is neatly intercalated without any CL adsorbed on the external surfaces of MMT tactoids. However, other CLM hybrid materials prepared at pH of 3 and 7 with an intercalated structure exhibit a lower T_g at 140–148°C or original T_g. This can be attributed to the fact that lots of CL is adsorbed on the external surfaces of MMT tactoids at pH of 3 and 7, which cannot be
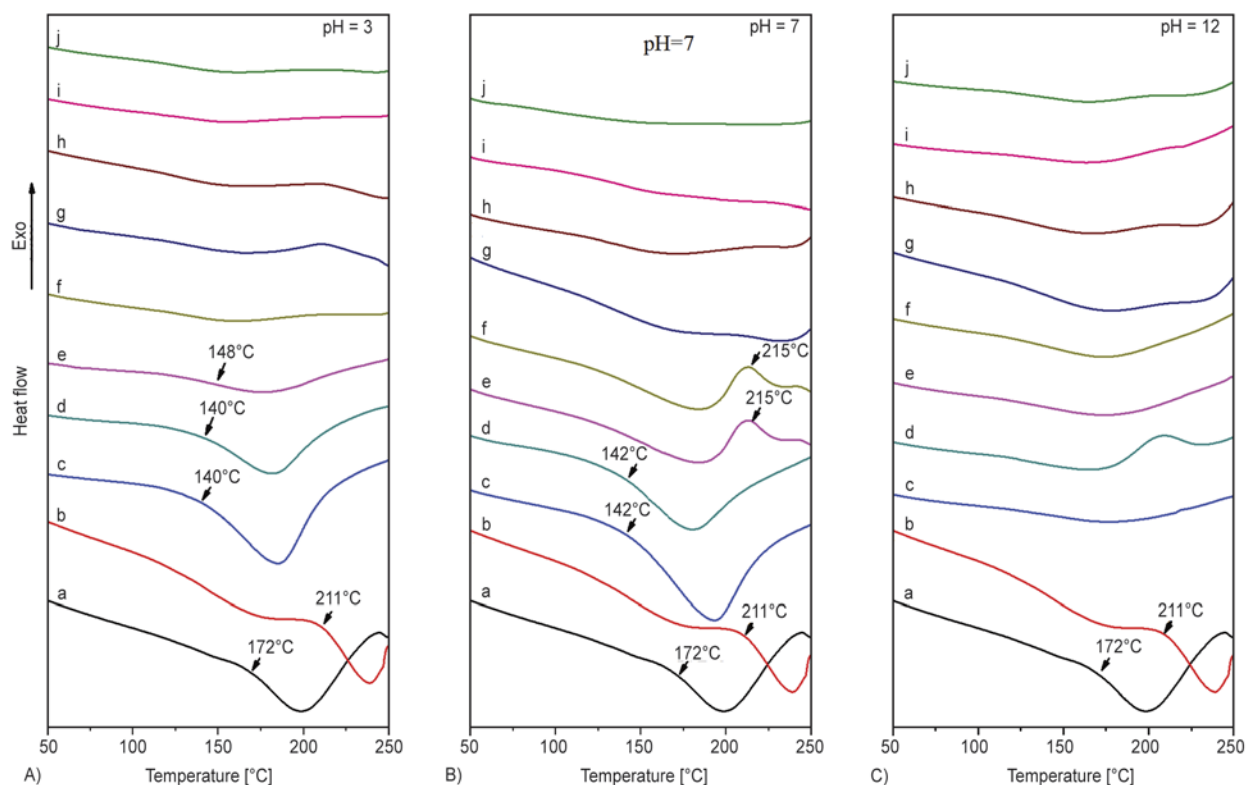
Figure 8. DSC curves of (a) lignin, (b) CL and CLM hybrid materials respectively prepared at pH of 3, 7 and 12, having CL-MMT mass ratio of (c) 0.1:1, (d) 0.2:1, (e) 0.4:1, (f) 0.8:1, (g) 2:1, (h) 4:1, (i) 6:1 and (j) 8:1

restricted by MMT platelets. Moreover, the hydrogen bonding between CL and MMT can weaken the interactions among CL molecules, thus resulting in lower T_g. DSC results have demonstrated that the mobility of CL molecules adsorbed onto MMT platelet surface is completely confined. In another word, the CL anchored onto MMT platelets is a steady 2D-nanosheet.

3.5. SBR/CLM composites

In previous reports, lignin has been proved to be an effective carbon black replacement for SBR via complicated latex co-coagulating procedure [44, 45]. In fact, the applications of lignin in rubber industry are seriously limited due to the extremely slow coagulating rate, as shown in Figure 9a. Even if the rate can be improved by heating the mixture solution, not all lignin can be incorporated into rubber and lignin will form thermal irreversible agglomerates to deteriorate the performance of rubber. However, the coagulating rate is substantially improved for SBR/CLM mixture, which can be attributed to the reduction of surface activity of lignin caused by the restriction effect of MMT.

The dispersion status of CLM in SBR matrix is also studied by XRD. As shown in Figure 9b, there is no obvious diffraction peak in all of sample as pure CLM exhibits, implying homogenous dispersion of CLM in SBR matrix. But the absence of peaks is also possibly originated from the lack of sensitivity of apparatus. Hence, the actual mass ratio of CL to MMT is determinated by TGA. As shown in Figure 9c, according to the residual char rate of MMT, CL and CLM, the actual mass ratio of CL to MMT is 4.16:1. Namely, in 10 phr CLM filled SBR matrix, the loading of CL is equivalent to about 8 phr while MMT is about 2 phr. Such a MMT loading is able to be detected by XRD, at least in the sample of S-CLM-10. Due to the barrier characteristic of MMT, the decomposition peaks of CL at 264.7 and 365.3°C shift to higher temperatures of 319.6 and 375.7°C in the sample of CLM respectively, and the weight loss rate of CLM is obviously reduced, demonstrating excellent thermal stability of CLM.

SEM images of SBR/CLM composites are shown in Figure 10a and 10b. It is clearly seen that CLM as protuberances showing an obvious aspect ratio is well dispersed and embedded into SBR matrix. The
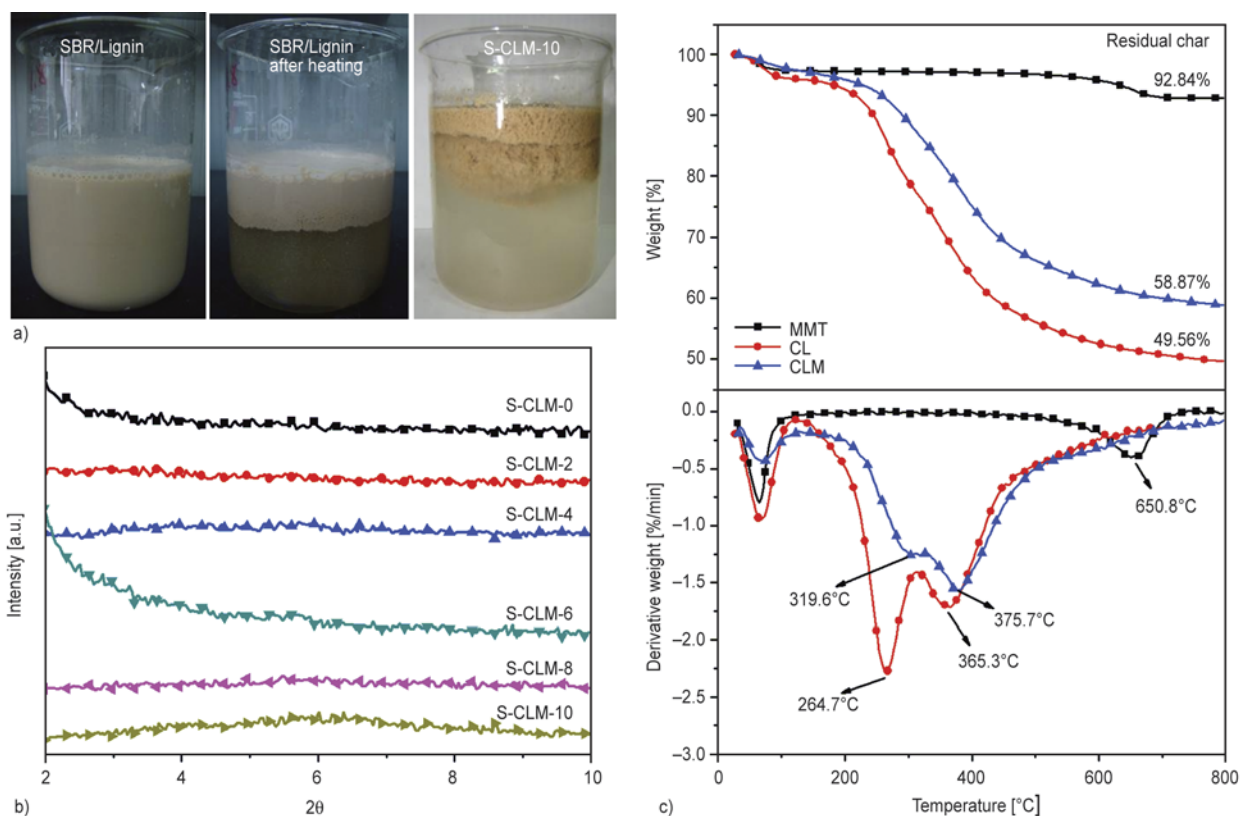
Figure 9. (a) Digital photos of co-coagulation of SBR latex with 10 phr lignin and CLM, (b) XRD patterns of SBR/CLM vulcanizates, (c) TG (top right) and DTG (bottom right) curves of MMT, CL and CLM

interface between CLM and SBR matrix is very blurry, implying good compatibility and strong interface adhesion between them. Actually, the interface structure is very special with the presence of compatibilizer CGE, which will be disclosed by DMA in the following text. The dispersion of CLM is further investigated by TEM. As shown in Figure 10c and 10d, CLM nanosheets are observed as plane-on dark domains throughout SBR matrix with a lateral dimension of several hundred nanometers, indicating the completely exfoliation of CLM. In addition, some CLM nanosheets are embedded into SBR matrix as edge-on dark lines with interlayer distance more than 5–10 nm. The results adequately demonstrate the uniform dispersion of CLM in SBR matrix.

As shown in Figure 11a, the tan δ peaks of SBR/CLM composites shift to lower temperature and the glass transition temperature (T_g) continually decreases from –46.2 to -52.2°C as increasing CLM loading, accompanying with increased loss tangent peak height. Additionally, the curves of the storage modulus E' vs. Temperature of the composites are also shown in Figure 11b. The E' of SBR/CLM composites increases with the CLM loading above 0°C, indicating the increase of the stiffness of the materials.

For polymer nanocomposites, T_g has been reported to increase, decrease or remain unchanged in previous researches, depending on the interface interactions of composites [46–48]. In our system, CGE is used as compatibilizer for SBR/CLM composites, which owns two different functional groups (epoxy groups and double bonds). Owing to the double bonds of CGE, it can be grafted onto the SBR molecule during curing process and acts as a plasticizer to lower T_g. when no CLM is added, CGE grafted SBR molecule is analogous to comb-like polymer chain and can mutually crosswise arrange in a relatively compact formation due to steric hindrance, as shown in Figure 12. However, once loading CLM, the comb-like SBR molecules are separated from each other by CLM. Moreover, not all epoxy groups of CGE can be opened under heating and bonded to the surface of CLM. Some of those can interact with CLM through hydrogen bonding. Consequently, in this way, the free volume of chain segments of SBR molecule is enlarged and the T_g of composites decreases with increasing CLM loading.

In rubber based nanocomposites, very strong chemical bonding or excessive chemical bonds between the rubber matrix and nanofillers are not acknowledged, because it may greatly restrict the slippage
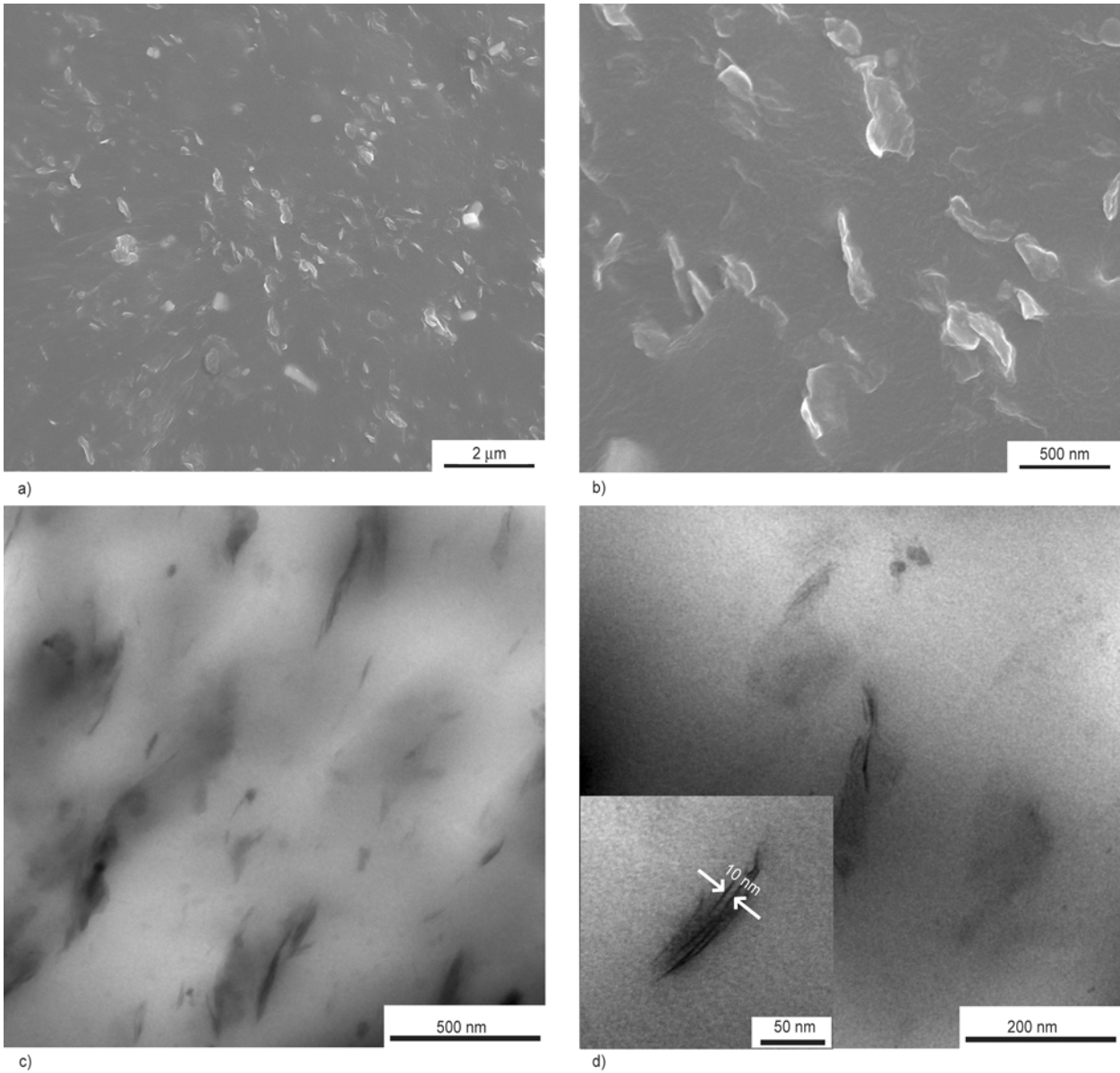
Figure 10. SEM (a, b) and TEM (c, d) photos of S-CLM-10 at different magnifications
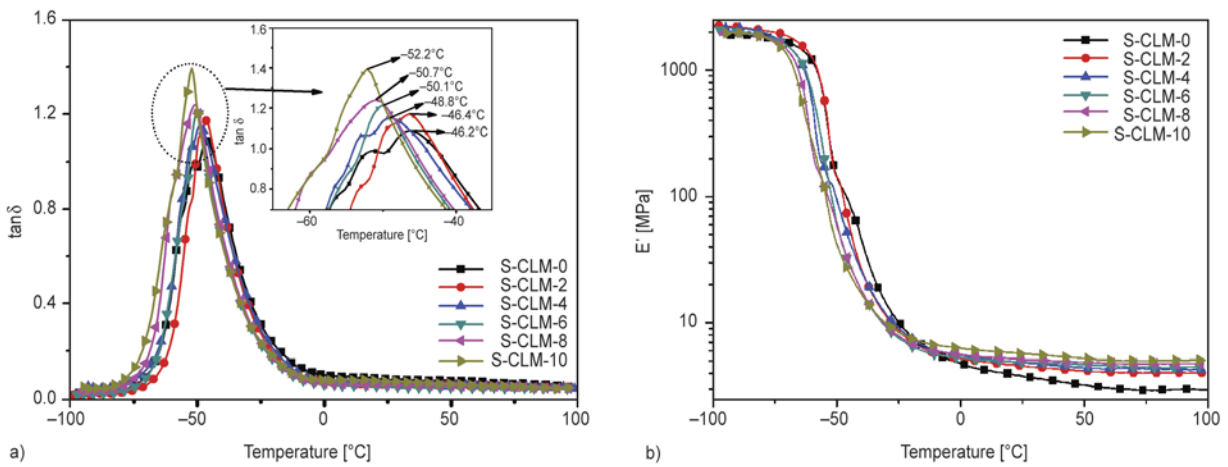

Figure 11. tan δ (a) and storage modulus *E'* (b) of SBR/CLM composites as a function of temperature

of rubber molecule chain, leading to the occurrence of fracture at decreased strain for centralized stress.

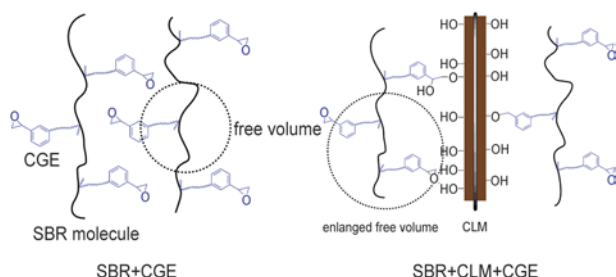In contrast, the CGE grafted SBR can interact with CLM via moderate chemical bonds and lots of

Figure 12. Schematic illustration of the interface structure of SBR/CLM composites

hydrogen bonding, which is in favor of SBR chains slipping along the surface of CLM to form orientated induced straight chains and uniformly distribute the external force. Hence, as shown in Figure 13 and Table 2, the ultimate stress of SBR/CLM composites can be extremely improved at higher deformation and the tensile modulus is also increased with increasing CLM loading, owing to the slippage of SBR chains to relieve stress concentration and moderate covalent bonding to transfer stress from matrix to CLM. Especially, the 300% modulus is substantially improved as increasing CLM loading, indicating a stronger filler-rubber interactions. With the inclusion of only 10 phr CLM, the ulti-

mate stress for S-CLM-10 can be increased to about 14.14 MPa, which is obviously superior to the properties of S-lignin-10 and those lignin-based SBR composites at the same lignin loading as previously reported [49].

4. Conclusions

The adsorption of CL onto MMT gave rise to a series of CLM hybrid materials with different structures. The adsorption isotherms showed very high and pH-dependent affinity between CL and MMT. The structures of CLM were characterized by XRD, TEM and AFM. It was found that MMT was neatly intercalated by CL at pH of 12, whereas MMT could be completely exfoliated into individually dispersed nanosheets covered by two layers of CL at pH of 7 and 3. The differences in structure strongly depended on the interactions between CL and MMT. Therefore, a schematic illustration was proposed to describe the adsorption mechanism, interactions between CL and MMT as well as the conformation features of CL anchored onto the surface of MMT platelets. The zeta potential measurements combined with aforementioned characterization techniques revealed that cation-π interactions was a dominant driving force for adsorption at alkaline and neutral pH, while the electrostatic attractive interactions drove the adsorption at acidic pH. Moreover, the different sizes of CL in AFM and DLS measurement confirmed the conformation change of CL from swollen spherical microgel to disk-like CL with a thickness of about 2 nm. DSC results indicated the strong confinement of CL molecules by MMT platelets. Finally, the incorporation of CLM into SBR via latex co-coagulating showed a higher coagulating rate compared to lignin, and the performance of composites was substantially improved by just adding 10 phr CLM. Hence, the plane-interface-induced method for preparing individually dispersed 2D CLM nanosheets provides a promising

Figure 13. Stress-strain curves of SBR/CLM composites and S-lignin-10

Table 2. The mechanical properties of SBR/CLM composites and S-lignin-10

Sample	Modulus at 100% [MPa]	Modulus at 300% [MPa]	Tensile strength [MPa]	Elongation at break [%]	Permanent set [%]	Hardness Shore A
S-CLM-0	0.80	1.62	2.73	421	6	43
S-CLM-2	1.06	2.29	3.46	431	6	47
S-CLM-4	1.18	2.58	3.39	407	4	48
S-CLM-6	1.33	3.04	4.98	473	6	48
S-CLM-8	1.27	2.88	7.20	588	9	48
S-CLM-10	1.47	3.88	14.14	718	16	48
S-lignin-10	1.45	3.38	6.71	516	8	47

way to explore value-added applications based on lignin.

Acknowledgements

References

[1] Gosselink R. J. A., Abächerli A., Semke H., Malherbe R., Käuper P., Nadif A., van Dam J. E. G.: Analytical protocols for characterisation of sulphur-free lignin. Industrial Crops and Products, **19**, 271–281 (2004).
DOI: 10.1016/j.indcrop.2003.10.008

[2] Saito K., Kato T., Tsuji Y., Fukushima K.: Identifying the characteristic secondary ions of lignin polymer using ToF–SIMS. Biomacromolecules, **6**, 678–683 (2005).
DOI: 10.1021/bm049521v

[3] Lora J. H., Glasser W. G.: Recent industrial applications of lignin: A sustainable alternative to nonrenewable materials. Journal of Polymers and the Environment, **10**, 39–48 (2002).
DOI: 10.1023/A:1021070006895

[4] Stewart D.: Lignin as a base material for materials applications: Chemistry, application and economics. Industrial Crops and Products, **27**, 202–207 (2008).
DOI: 10.1016/j.indcrop.2007.07.008

[5] Pouteau C., Dole P., Cathala B., Averous L., Boquillon N.: Antioxidant properties of lignin in polypropylene. Polymer Degradation and Stability, **81**, 9–18 (2003).
DOI: 10.1016/S0141-3910(03)00057-0

[6] Hambardzumyan A., Foulon L., Chabbert B., Aguié-Béghin V.: Natural organic UV-absorbent coatings based on cellulose and lignin: Designed effects on spectroscopic properties. Biomacromolecules, **13**, 4081–4088 (2012).
DOI: 10.1021/bm301373b

[7] Lalwani G., Henslee A. M., Farshid B., Lin L., Kasper F. K., Qin Y-X., Mikos A. G., Sitharaman B.: Two-dimensional nanostructure-reinforced biodegradable polymeric nanocomposites for bone tissue engineering. Biomacromolecules, **14**, 900–909 (2013).
DOI: 10.1021/bm301995s

[8] Aricò A. S., Bruce P., Scrosati B., Tarascon J-M., van Schalkwijk W.: Nanostructured materials for advanced energy conversion and storage devices. Nature Materials, **4**, 366–377 (2005).
DOI: 10.1038/nmat1368

[9] Walsh M. J., Yoshida K., Kuwabara A., Pay M. L., Gai P. L., Boyes E. D.: On the structural origin of the catalytic properties of inherently strained ultrasmall decahedral gold nanoparticles. Nano Letters, **12**, 2027–2031 (2012).
DOI: 10.1021/nl300067q

[10] Shamsipur M., Asgari M., Mousavi M. F., Davarkhah R.: A novel hydrogen peroxide sensor based on the direct electron transfer of catalase immobilized on nano-sized NiO/MWCNTs composite film. Electroanalysis, **24**, 357–367 (2012).
DOI: 10.1002/elan.201100453

[11] Panyam J., Labhasetwar V.: Biodegradable nanoparticles for drug and gene delivery to cells and tissue. Advanced Drug Delivery Reviews, **64**, 61–71 (2012).
DOI: 10.1016/S0169-409X(02)00228-4

[12] Vainio U., Maximova N., Hortling B., Laine J., Stenius P., Simola L. K., Gravitis J., Serimaa R.: Morphology of dry lignins and size and shape of dissolved kraft lignin particles by X-ray scattering. Langmuir, **20**, 9736–9744 (2004).
DOI: 10.1021/la048407v

[13] Lindströmn T.: The colloidal behaviour of kraft lignin. Colloid and Polymer Science, **257**, 277–285 (1979).
DOI: 10.1007/BF01382370

[14] Kubo S., Kadla J. F.: Hydrogen bonding in lignin: A Fourier transform infrared model compound study. Biomacromolecules, **6**, 2815–2821 (2005).
DOI: 10.1021/bm050288q

[15] Deng Y., Feng X., Zhou M., Qian Y., Yu H., Qiu X.: Investigation of aggregation and assembly of alkali lignin using iodine as a probe. Biomacromolecules, **12**, 1116–1125 (2011).
DOI: 10.1021/bm101449b

[16] Caicedo H. M., Dempere L. A., Vermerris W.: Template-mediated synthesis and bio-functionalization of flexible lignin-based nanotubes and nanowires. Nanotechnology, **23**, 105605/1–105605/12 (2012).
DOI: 10.1088/0957-4484/23/10/105605

[17] Spender J., Demers A. L., Xie X., Cline A. E., Earle M. A., Ellis L. D., Neivandt D. J.: Method for production of polymer and carbon nanofibers from water-soluble polymers. Nano Letters, **12**, 3857–3860 (2012).
DOI: 10.1021/nl301983d

[18] Gonugunta P., Vivekanandhan S., Mohanty A. K., Misra M.: A study on synthesis and characterization of bio-based carbon nanoparticles from lignin. World Journal of Nano Science and Engineering, **2**, 148–153 (2012).
DOI: 10.4236/wjnse.2012.23019

[19] Frangville C., Rutkevičius M., Richter A. P., Velev O. D., Stoyanov S. D., Paunov V. N.: Fabrication of environmentally biodegradable lignin nanoparticles. ChemPhysChem, **13**, 4235–4243 (2012).
DOI: 10.1002/cphc.201200537

[20] Lu Q., Zhu M., Zu Y., Liu W., Yang L., Zhang Y., Zhao X., Zhang X., Zhang X., Li W.: Comparative antioxidant activity of nanoscale lignin prepared by a supercritical antisolvent (SAS) process with non-nanoscale lignin. Food Chemistry, **135**, 63–67 (2012).
DOI: 10.1016/j.foodchem.2012.04.070

[21] Ray S. S., Okamoto M.: Polymer/layered silicate nanocomposites: A review from preparation to processing. Progress in Polymer Science, **28**, 1539–1641 (2003).
DOI: 10.1016/j.progpolymsci.2003.08.002

[22] Wicklein B., Darder M., Aranda P., Ruiz-Hitzky E.: Bio-organoclays based on phospholipids as immobilization hosts for biological species. Langmuir, **26**, 5217–5225 (2010).
DOI: 10.1021/la9036925

[23] Radian A., Mishael Y. G.: Characterizing and designing polycation–clay nanocomposites as a basis for imazapyr controlled release formulations. Environmental Science and Technology, **42**, 1511–1516 (2008).
DOI: 10.1021/es7023753

[24] Darder M., Colilla M., Ruiz-Hitzky E.: Biopolymer–clay nanocomposites based on chitosan intercalated in montmorillonite. Chemistry of Materials, **15**, 3774–3780 (2003).
DOI: 10.1021/cm0343047

[25] Gilman J. W., Awad W. H., Davis R. D., Shields J., Harris R. H., Davis C., Morgan A. B., Sutto T. E., Callahan J., Trulove P. C., DeLong H. C.: Polymer/layered silicate nanocomposites from thermally stable trialkylimidazolium-treated montmorillonite. Chemistry of Materials, **14**, 3776–3785 (2002).
DOI: 10.1021/cm011532x

[26] Podsiadlo P., Kaushik A. K., Arruda E. M., Waas A. M., Shim B. S., Xu J., Nandivada H., Pumplin B. G., Lahann J., Ramamoorthy A., Kotov N. A.: Ultrastrong and stiff layered polymer nanocomposites. Science, **318**, 80–83 (2007).
DOI: 10.1126/science.1143176

[27] Choi J. H., Park Y. W., Park T. H., Song E. H., Lee H. J., Kim H., Shin S. J., Fai V. L. C., Ju B.: Fuzzy nanoassembly of polyelectrolyte and layered clay multicomposite toward a reliable gas barrier. Langmuir, **28**, 6826–6831 (2012).
DOI: 10.1021/la300831p

[28] Joly S., Garnaud G., Ollitrault R., Bokobza L., Mark J. E.: Organically modified layered silicates as reinforcing fillers for natural rubber. Chemistry of Materials, **14**, 4202–4208 (2002).
DOI: 10.1021/cm020093e

[29] Rooj S., Das A., Stöckelhuber K. W., Reuter U., Heinrich G.: Highly exfoliated natural rubber/clay composites by 'propping-open procedure': The influence of fatty-acid chain length on exfoliation. Macromolecular Materials And Engineering, **297**, 369–383 (2012).
DOI: 10.1002/mame.201100185

[30] Goring D. A. I., Vuong R., Gancet C., Chanzy H.: The flatness of lignosulfonate macromolecules as demonstrated by electron microscopy. Journal of Applied Polymer Science, **24**, 931–936 (1979).
DOI: 10.1002/app.1979.070240406

[31] Jiang C., He H., Jiang H., Ma L., Jia D. M.: Nanolignin filled natural rubber composites: Preparation and characterization. Express Polymer Letters, **7**, 480–493 (2013).
DOI: 10.3144/expresspolymlett.2013.44

[32] Pulkkinen E., Mäkelä A., Mikkonen H.: Preparation and testing of cationic flocculants from kraft lignin. ACS Symposium Series, **397**, 284–293 (1989).
DOI: 10.1021/bk-1989-0397.ch021

[33] Laszlo J. A.: Solubility and dye-binding properties of quaternized and peroxidase-polymerized kraft lignin. Environmental Technology, **20**, 607–615 (1999).
DOI: 10.1080/09593332008616855

[34] Ueno K., Kina K.: Colloid titration-A rapid method for the determination of charged colloid. Journal of Chemical Education, **62**, 627–629 (1985).
DOI: 10.1021/ed062p627

[35] Breen C.: The characterisation and use of polycation-exchanged bentonites. Applied Clay Science, **15**, 187–219 (1999).
DOI: 10.1016/S0169-1317(99)00024-1

[36] Moreva Y. L., Alekseeva N. S., Chernoberezhskii Y. M.: Influence of NaOH, HCl, NaCl, and $CaCl_2$ electrolytes on aggregation stability of aqueous craft lignin dispersion according to data of filtration through track membranes. Colloid Journal, **73**, 363–367 (2011).
DOI: 10.1134/S1061933X11030082

[37] Giles C. H., MacEwan T. H., Nakhwa S. N., Smith D.: Studies in adsorption. Part XI. A system of classification of solution adsorption isotherms, and its use in diagnosis of adsorption mechanisms and in measurement of specific surface areas of solids. Journal of the Chemical Society, **1960**, 3973–3993 (1960).
DOI: 10.1039/JR9600003973

[38] Miller R., Fainerman V. B., Möhwald H.: Adsorption behavior of oxyethylated surfactants at the air/water interface. Journal of Colloid and Interface Science, **247**, 193–199 (2002).
DOI: 10.1006/jcis.2001.8120

[39] Theng B. K. G.: Clay-polymer interactions: Summary and perspectives. Clays and Clay Minerals, **30**, 1–10 (1982).
DOI: 10.1346/CCMN.1982.0300101

[40] Beall G. W., Goss M.: Self-assembly of organic molecules on montmorillonite. Applied Clay Science, **27**, 179–186 (2004).
DOI: 10.1016/j.clay.2004.06.006

[41] Dang Q., Lu S., Yu S., Sun P., Yuan Z.: Silk fibroin/montmorillonite nanocomposites: Effect of ph on the conformational transition and clay dispersion. Biomacromolecules, **11**, 1796–1801 (2010).
DOI: 10.1021/bm1002398

[42] Pillai K. V., Renneckar S.: Cation–π interactions as a mechanism in technical lignin adsorption to cationic surfaces. Biomacromolecules, **10**, 798–804 (2009).
DOI: 10.1021/bm801284y

[43] Adame D., Beall G. W.: Direct measurement of the constrained polymer region in polyamide/clay nanocomposites and the implications for gas diffusion. Applied Clay Science, **42**, 545–552 (2009).
DOI: 10.1016/j.clay.2008.03.005

[44] Davidson M. J. G., Wunder R. H.: Latex coagulation process using lignin compound. U.S. Patent 4025711, USA (1977).

[45] Sirianni A. F.: Puddington I. E.: Laundered amorphous reinforcing lignin. U.S. Patent 3817974, USA (1974).

[46] Harton S. E., Kumar S. K., Yang H., Koga T., Hicks K., Lee H., Mijovic J., Liu M., Vallery R. S., Gidley D. W.: Immobilized polymer layers on spherical nanoparticles. Macromolecules, **43**, 3415–3421 (2010).
DOI: 10.1021/ma902484d

[47] Lee K. J., Lee D. K., Kim Y. W., Choe W., Kim J. H.: Theoretical consideration on the glass transition behavior of polymer nanocomposites. Journal of Polymer Science Part B: Polymer Physics, **45**, 2232–2238 (2007).
DOI: 10.1002/polb.21178

[48] Ash B. J., Siegel R. W., Schadler L. S.: Glass-transition temperature behavior of alumina/PMMA nanocomposites. Journal of Polymer Science Part B: Polymer Physics, **42**, 4371–4383 (2004).
DOI: 10.1002/polb.20297

[49] Košíková B., Gregorová A.: Sulfur-free lignin as reinforcing component of styrene–butadiene rubber. Journal of Applied Polymer Science, **97**, 924–929 (2005).
DOI: 10.1002/app.21448

Preparation of aromatic polyamidines and their transformation in polybenzimidazoles

B. Ch. Kholkhoev[*], *V. F. Burdukovskii*, *D. M. Mognonov*

Baikal Institute of Nature Management, Siberian Branch of the Russian Academy of Sciences, Sakhyanova Str. 6, 670047 Ulan-Ude, Russia

Abstract. Polymers with amidine groups –NH–C(=NH)– in main chain were synthesized by two different approaches. The first strategy consists in polyaddition of dinitriles and diamines in acidic ionic liquids (ILs) which act as catalyst and solvent, while the second approach is based on polycondensation of 4,4′-oxybis(benzoic acid) diamide and diamines in Eaton's reagent (ER). The resulting polyamidines (PADs) with M_w up to 25 000 g/mol possess thermal stability on air up to 288°C, and good solubility in polar organic solvents. Moreover dehydrocyclization of obtained PADs into polybenzimidazoles (PBIs) under the action of various oxidants was also studied in this work. The crosslinked films based on PBI and poly(amino imide) resin (PAIR) possess high mechanical characteristics. It has been proved that the crosslinked films based on PBI matrix are perspective materials for design the phosphoric acid electrolyte membranes for the medium temperature fuel cells.

Keywords: polymer synthesis, polymer blends, polyamidines, polybenzimidazoles, proton exchange membrane fuel cells

1. Introduction

In recent years, considerable researchers' attention has been focused on PADs owing to the wide prospects for their use in optoelectronics, organometallic catalysis, medicine, enzymology, and other fields [1–6]. Although polymers of this class show much promise, they have not been studied to a great extent. In terms of the position of amidine groups in the polymer chain, there are two groups of PADs (Figure 1), among which PADs-I have been most extensively studied [7–10]. PADs with structure II are much less studied compounds. Only a few examples of synthesis of these PADs are known [5, 6, 11–14]. Therefore development of synthetic routs to PADs-II is important problem. In addition to the fundamental importance of PADs-II, they can be used as precursors for the preparation of PBIs. Brand *et al.* [14] outlined possibility of preparing PBIs by oxida-
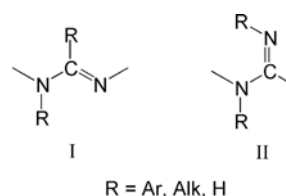

Figure 1. Structures of polyamidines

tive dehydrocyclization of PADs, which were synthesized by polyaddition of dinitriles with diamines in melt. However, the formed polymers had low molecular weights and were incapable to form films and press materials with satisfactory mechanical properties, and therefore they cannot be used in different areas of industry, in particular for proton exchange membrane fuel cells [15].

In this work successful modification of synthesis of aromatic PADs from dinitriles and diamines by using

acidic ILs as catalyst and solvent is described. Moreover we developed a new method of synthesis of such polymers consisting in polycondensation of 4,4′-oxybis(benzoic acid) diamide and diamines using ER as condensing agent and solvent. The dependence of reaction conditions on molecular weights of the obtained PADs has been investigated in details. Synthesized polymers were characterized by Fourier transform infrared (FTIR) and nuclear magnetic resonance (NMR) spectroscopies, thermogravimetry (TGA) and gel permeation chromatography (GPC). Moreover dehydrocyclization of PADs into PBIs under the action of various oxidants was studied. Also, the mechanical properties and proton conductivity of membranes based on a blend of PBIs and PAIR were also determined.

2. Experimental section

2.1. Materials

1-butyl-3-methylimidazolium chloride ([BMIm]Cl) (99.4%, 4900790100, Merck, Germany), 1-butyl-3-methylimidazolium bromide ([BMIm]Br) (99.8%, 4900870100, Merck, Germany), 1-butyl-3-methylimidazolium tetrafluoroborate ([BMIm]BF4) (99.9%, 4900490100, Merck, Germany), 1-butyl-2,3-dimethylimidazolium chloride ([BM2Im]Cl) (99.8%, 4900210100, Merck, Germany), 1-Ethyl-3-methylimidazolium chloride ([EMIm]Cl) (99.8%, 4900540100, Merck, Germany), methanesulfonic acid (MSA) ($\geq$99.5%, 471356, Sigma-Aldrich, Germany), terephthalonitrile (99%, 8210760250, Merck, Germany), isophthalonitrile (99%, 8413550100, Merck, Germany), all diamines ($\geq$99%, Sigma-Aldrich, Germany), aluminium chloride (99%, 563919, Sigma-Aldrich, Germany), phosphorus pentoxide ($\geq$98%, 298220, Sigma-Aldrich, Germany), sodium hypochlorite solution (1056142500, Merck, Germany) were used without further purification.

Reagent-grade N,N-dimethylformamide (DMF), N,N-dimethylacetamide (DMAc), N-methyl-2-pyrrolidone (MP), dimethylsulfoxide (DMSO), chloroform, dichloromethane, methanol were obtained from Sigma-Aldrich (Germany), and were purified by distillation over P_2O_5.

4,4′-oxybis(benzoic acid) diamide was synthesized by low-temperature condensation of 4,4′-oxybis(benzoic acid) dichloride with concentrated aqua ammonia solution as described previously [16]. 4,4′-dicyanodiphenyloxide was obtained by dehydration of 4,4′-oxybis(benzoic acid) diamide using thionyl chloride in DMF solution [17].

Acidic $Al_xHal_y^-$ containing ionic liquids were prepared by the slow addition of the desired amount of $AlHal_3$ to the imidazolium salt. The reaction was left to stir overnight at 0°C for 24 h, in order to allow a perfect homogenization of the resulting acidic ionic liquid [18].

For the preparation of Eaton's reagent (ER) following procedure was used. Phosphorus pentoxide and methanesulfonic acid were placed in a 50 mL round-bottom flask with a magnetic stirrer. The mixture was stirred at 60–70°C until there was complete dissolution of P_2O_5 [19]. This mixture was used as a solvent for polycondensation and was prepared just before use.

PAIR was supplied from 'Karbolit' plant (Kemerovo city, Russia) and was used as received.

2.2. Polymer synthesis

2.2.1. Synthesis of polyamidines in ionic liquids

PADs were synthesized in a 50 mL three-necked flask equipped with a stirrer and an inlet and an outlet for argon. The typical procedure is as follows. First, 0.12 g (0.9375 mmol) of terephthalonitrile and 0.1875 g (0.9375 mmol) of 4,4′-diaminodiphenyloxide were added to the clear liquid of [BMIm]Al_2Cl_7. Next, the reaction mixture was placed in a bath, and the temperature was raised up to 190–200°C. After about 15–16 h, viscous solution was poured into a 5% aqueous KOH solution. Finally, precipitate was filtrated, washed several times with water (typically three times) until neutral pH of the washing water, and dried in *vacuo* at 60°C for 24 h. Anal. Calcd for $C_{20}H_{16}N_4O$: C, 73.17%; H, 4.88%; N, 17.07%; O, 4.88%. Found: C, 72.05%; H, 4.72%; N, 18.93%. IR (KBr pellet): 3450 (m), 3000 (m), 2750 (m), 1605 (s, $v_{C=N}$), 1568 (w), 1500 (s), 1368 (w, v_{C-N}), 1200 (s, v_{C-O-C}) cm^{-1}.

2.2.2. Synthesis of polyamidines in Eaton's reagent

Typical example of the polycondensation follows. First, 4,4′-oxybis(benzoic acid) diamide 0.768 g (0.003 mol), 4,4′-diaminodiphenyloxide 0.6 g (0.003 mol) were stirred in ER for ~0.5 h at 100°C under argon. After the dissolution of the monomers, the temperature was raised up to 120°C, and the mixture was stirred for 4–5 h at this temperature.

The resulted extremely viscous solution was diluted with methanesulfonic acid. This polymer solution was poured into water, and neutralized with sodium carbonate solution. The polymer was collected by filtration, washed with hot water and dried in vacuo at 60°C for 24 h. Anal. Calcd for $C_{26}H_{20}N_4O_2$: C, 74.29%; H, 4.76%; N, 13.33%; O, 7.62%. Found: C, 73.42%; H, 4.84%; N, 14.72%. IR (KBr pellet): 3450 (m), 3010 (m), 2830 (m), 1620 (s, $v_{C=N}$), 1540 (w), 1500 (s), 1350 (w, $v_{C–N}$), 1210 (s, $v_{C–O–C}$) cm^{-1}.

2.2.3. Synthesis of polybenzimidazoles

A suspension of 0.5 g of PAD **2a** in 5 mL of 1 M aqueous HCl and 7 mL of methanol was refluxed with stirring for 30 min. After cooling the resulting solution to room temperature, 2 mL of a hydrogen peroxide solution (40.8%, 35 mmol) was added dropwise. The mixture was stirred for an additional 20 min. Then 15 mL of DMF was added to make the solution fully homogeneous. After adding 6 M aqueous KOH (0.6 mL), the mixture was heated at 100°C for 4 h. Then the reaction solution was poured into 300 mL of ice-cold water. The obtained polymer was filtered off and dried in a vacuum oven at 50°C to constant weight. Anal. Calcd for $C_{20}H_{12}N_4O$: C, 74.08%; H, 3.70%; N, 17.28%; O, 4.94%. Found: C, 73.81%; H, 3.87%; N, 16.93%. IR (KBr pellet): 3450 (m), 3000 (m), 2800 (m), 1630 (s, $v_{C=N}$), 1545 (w), 1450 (s), 1360 (w, $v_{C–N}$), 1110 (s), 1200 (s, $v_{C–O–C}$), 730 (s) cm^{-1}.

2.3. Measurements

Inherent viscosity [η] (IV) was measured with an Ubbelohde-type viscometer at 20°C in DMF or in H_2SO_4. FTIR spectra were recorded on Excalibur FTS 4000 spectrometer (Germany) in the wave number range 4000–400 cm^{-1}. The samples were prepared as KBr pellets. ^{13}C NMR spectra were recorded on a Varian VXR-500S spectrometer (USA) operating at 125 MHz. DMSO-d$_6$ was used as both solvent and internal standard ($\delta(^{13}C) = 39.50$ ppm). Dynamic TGA was performed on STA 449 C14/G Jupiter (Netzsch, Germany) 5°C/min. Al_2O_3 was used as a reference. Gel permeation chromatography (GPC) was performed on 'Waters' chromatograph (USA) at 20°C. Tetrahydrofuran was used as eluent (flow rate – 0.5 mL/min). Weight-average molecular weights (M_w) were calculated relative to polystyrene standards.

Film materials were prepared by casting a 10–15% polymer solution in DMF onto a glass support. PBI–PAIR films of various compositions were prepared by mixing 10–15% solutions of the initial polymers in DMF. The solution distributed on the substrate surface was dried on air at first, and then a crude film was post-dried *in vacuo* at 40–70°C to remove remains of DMF. The films were kept in the extended state under a load of 0.5 kPa in a vacuum oven at 160°C for 48 h. Membranes were obtained by soaking cured films into water solutions of H_3PO_4 with concentrations of 9 M for 5 days. After soaking, the membranes were removed from solutions of H_3PO_4, and acid residues were wiped with a filter paper. The membranes were dried in vacuo at room temperature up to a constant weight. Water content in obtained membranes does not exceed 8–10%.

A proton conductivity of a membrane was measured by van der Pauw four-probe method [20] at current frequency of 500 Hz under dry argon flow and calculated according to Equation (1):

$$\sigma = \frac{I_{12}}{4.53 \cdot h \cdot U_{34}} \qquad (1)$$

where σ is a proton conductivity [S/cm]; I_{12} is a current between flank probes of 1 and 2 [A]; U_{34} is a voltage between flank probes of 3 and 4 [V]; h is a thickness of a sample [cm].

3. Results and discussion
3.1. Preparation of polyamidines

The proposed concept to aromatic PADs with an improved molecular weight focuses on two different approaches. The first strategy consists in polyaddition of dinitriles and diamines in ionic liquids, while the second one is based on polycondensation of diamide and diamines in Eaton's reagent.

3.1.1. Polyamidines from dinitriles and diamines

It is known [21–23] that the reactions of aromatic nitriles with amines are well-catalyzed by protic and aprotic acids. Among many catalysts, the aprotic acids (Lewis acids) have been found to be very useful to provide good yields of desired amidines [21, 22], but in general, the yields are not high enough to consider their use in the formation of high molecular weight polymers. Along with this, acidic ILs on the basis of metal halides can be regarded as an alternative for the traditional heterogeneous and

homogeneous catalysts, in particular aluminium chloride [24]. These ILs were successfully used for different acid-catalyzed reactions, such as Friedel-Crafts alkylation and acylation [24–27], nitrations [24, 25] and halogenations [24, 25, 28].

These data altogether in combination with the ability of ILs to dissolve different organic compounds (in particular, nitriles and amines) and polymers served as the basis for the studying the possibility of synthesis of PADs from aromatic dinitriles and diamines in ionic media (Figure 2). Moreover, the efficacy of ILs in the synthesis of polyheteroarylenes was shown [29–32].

In order to determine the optimal conditions for the reaction, the polyaddition of terephthalonitrile and 4,4′-diaminodiphenyl oxide in [BMIm]Cl/AlCl$_3$ was studied (synthesis of polymer **1a**).

Molar ratio [BMIm]Cl/AlCl3 strongly influences on catalytic activity of IL in acid-catalyzed reactions [24]. Therefore, at first, the effect of amount of aluminium chloride in IL system on [η] of the PAD was examined. It has been found that in the mixtures [BMIm]Cl/AlCl$_3$ containing 0÷1 equivalents of AlCl$_3$, which are, in fact, eutectic mixtures of [BMIm]Cl and [BMIm]AlCl$_4$, only low-molecular weight PADs are formed ([η] = 0.07–0.11 dL/g). Molecular weight of the obtained PAD significantly increases when polymerization was carried out in the systems containing >1 equivalents of AlCl$_3$ (Figure 3). The best results were achieved in IL containing 2 equivalents of AlCl$_3$, i.e. under conditions where strongly acidic IL [BMIm]Al$_2$Cl$_7$, generated
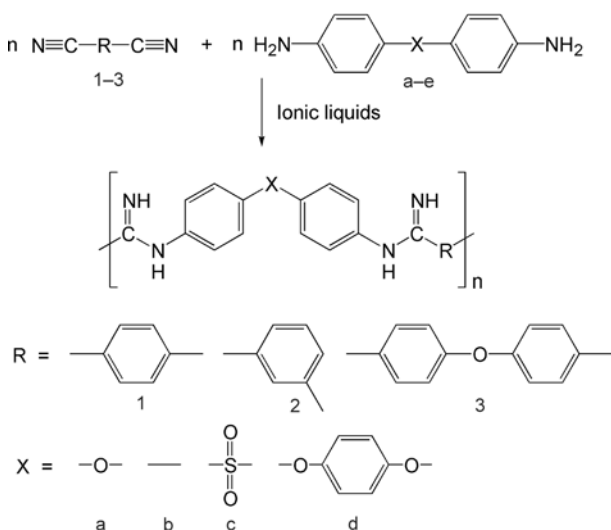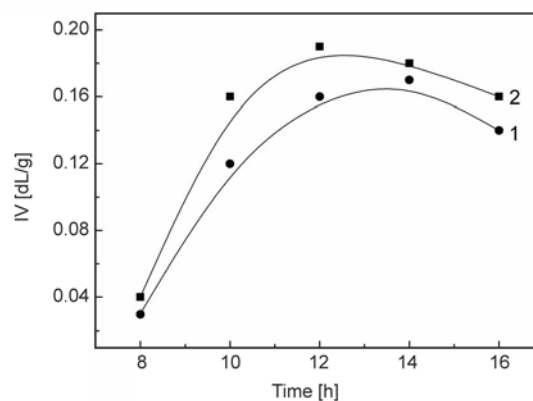

Figure 3. Effect of reaction time on IV of PAD **1a** obtained by the polyaddition in IL: [BMIm]Cl/AlCl$_3$ = 1:1.1 (1), [BMIm]Cl/AlCl$_3$ = 1:2 (2), at 160°C and monomer concentration of 0.6 mol/L

from [BMIm]AlCl$_4$ and AlCl$_3$, serves as the reaction medium [24].

The IV of the synthesized polymer also depends on the temperature and concentration of the initial monomers. The temperature of 190–200°C and the concentration of monomers 1.0 mol/L are optimal (Figure 4). Further increase in the temperature and the concentration of the monomers results in noticeable reduction of the [η] of the PAD.

Under the optimal reaction conditions, the polymerization also occurs in other studied ILs (Table 1). The PAD with the highest molecular weight ([η]) is formed in [BMIm]Al$_2$Br$_7$ and [BMIm]Al$_2$Cl$_7$, while the [η] of PAD obtained in conventional organic solvents (nitrobenzene, sulfolane) and in melt does not exceed 0.13 and 0.28 dL/g, respectively [33].

On the basis of these studies, then, the polyaddition of various dinitriles with diamines was carried out
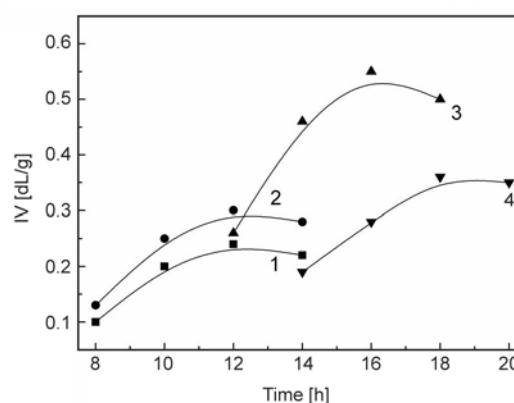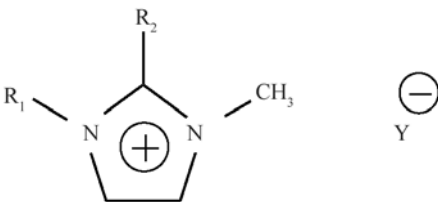

Figure 2. Synthesis of polyamidines from dinitriles and diamines

Figure 4. Effect of reaction time and monomer concentration on IV of PAD **1a** obtained by the polyaddition in [BMIm]Al$_2$Cl$_7$, at 190–200°C and monomer concentration of 0.6 (1), 0.8 (2), 1.0 (3) and 1.2 (4) mol/L

Table 1. Effect of nature of ionic liquids on intrinsic viscosity of polyamidine **1a**

№	IL	R₁	R₂	Y⁻	IVᵃ [dL/g]
		R₁	**R₂**	**Y⁻**	
1	[BMIm]Cl	C_4H_9	H	Cl	0.07
2	[BMIm]Al₂Cl₇	C_4H_9	H	Al₂Cl₇	0.55
3	[EMIm]Al₂Cl₇	C_2H_5	H	Al₂Cl₇	0.19
4	[BM₂Im]Al₂Cl₇	C_4H_9	CH₃	Al₂Cl₇	0.30
5	[BMIm]Al₂Br₇	C_4H_9	H	Al₂Br₇	0.42
6	[BMIm]BF₄	C_4H_9	H	BF₄	0.23

ᵃMeasured in sulfuric acid at 20°C

under found optimal reaction conditions (Figure 2). The results are shown in the Table 2. The polyaddition proceeded in homogeneous solution and gave quantitative yields of polymers with IV up to 0.55 dL/g.

One of the advantages of ILs is the ability to use them in the recycle. Therefore it was interesting to re-use of [BMIm]Al₂Cl₇ after polymerization of aromatic dinitriles and diamines. The recycle was performed as follows: first, reaction solution was poured into chloroform or dichloromethane; second, the obtained precipitate was collected by filtration; and finally, mixture of IL and organic solvent was separated by vacuum distillation. It was found that yield of regenerated IL was 60–70%. The reason for the loss of IL could be due to strong complexation of IL

with the formed PAD. Investigation of precipitate obtained after pouring of reaction mixture in chlorinated solvent confirmed this assumption. PAD/IL complexes can be easily hydrolyzed by dissolution in a mixture of 1N aqua HCl and CH₃OH (1/1, v/v) and further precipitation of PAD with 5% aqua KOH solution.

So, we not only successfully synthesized aromatic PADs based on dinitriles and diamines in chloroaluminate ILs, but also regenerated ionic solvent.

3.1.2. Polyamidines from 4,4′-oxybis(benzoic acid) diamide and diamines

With consideration for the fact that diamides transform into dinitriles under the action of dehydrating agents, it was advisable to examine the synthesis of PADs through the 'direct polycondensation', which is based on the interaction of diamines and diamides in a condensing medium. Being one of the most effective agents for obtaining various polyheteroarylenes [34–36], Eaton's reagent (CH₃SO₃H:P₂O₅ = 10:1, wt/wt) was selected as a condensing medium. Aromatic PADs were synthesized according to the Figure 5. The main features of polycondensation were investigated for the interaction of 4,4′-oxybis(benzoic acid) diamide and 4,4'-diaminodiphenyl oxide (synthesis of polymer **4a** Figure 5).

The effect of the synthesis temperature on the molecular mass of the PAD was studied in the range of 100–140°C, because the rate of reaction was very low at temperatures below 100°C, whereas decomposition of the main component of Eaton's reagent, methanesulfonic acid, began at a temperature above 150°C. Polycondensation performed at 120°C and a concentration of initial monomers of 0.6 mol/L for

Table 2. Characteristics of polyamidines obtained from dinitriles and diamines in [BMIm]Al₂Cl₇

№	PAD	IVᵃ [dL/g]	Decomposition temperatureᵇ [°C]
1	1a	0.55ᶜ	275
2	2a	0.51	272
3	3a	0.32	–
4	1b	0.52	288
5	2b	0.44	278
6	3b	0.27	–
7	1c	0.40	282
8	2c	0.33	–
9	3c	0.22	–
10	1d	0.53	–
11	2d	0.46	–
12	3d	0.29	–

ᵃMeasured in sulfuric acid at 20°C
ᵇTemperature of 10% weight loss determined by TGA at a heating rate of 5°C/min
ᶜM_w = 19 000 g/mol, M_w/M_n = 1.62 (GPC). Film properties: tensile strength (σ) = 29.5 MPa, elongation (ε) = 4.2%.
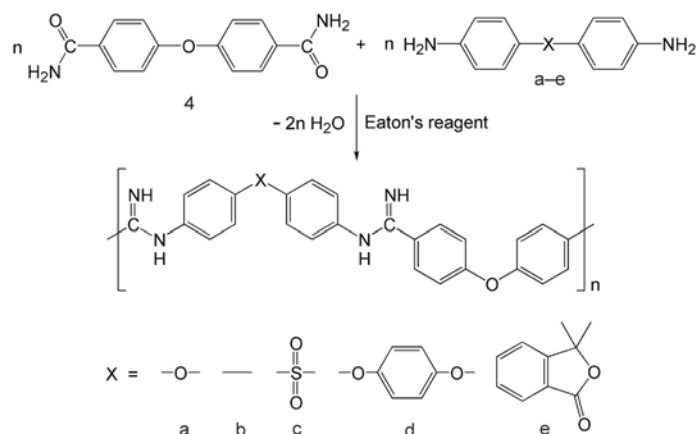
Figure 5. Synthesis of polyamidines from 4,4′-oxybis(benzoic acid) diamide and diamines

10 h yielded the PAD with the highest [η] value, 0.20 dL/g. At a temperature of 100–120°C, the poly-condensation proceeded with the formation of a transparent light brown solution, whereas at 140°C, after 6–8 h, the reaction solution became dark brown probably owing to the degradation of monomers and/or polymer.

Further study of polycondensation showed that the molecular mass of the formed PAD is strongly affected by the concentration of the initial mono-mers. It was found that the highest molecular mass PAD is formed at a concentration of monomers of 0.8 mol/L; a further increase in concentration leads to a marked decline in the molecular mass of the PAD. The molar ratio of phosphorus pentoxide to diamide for a concentration of monomers of 0.8 mol/L in Eaton's reagent ($CH_3SO_3H:P_2O_5$ = 10:1, wt/wt) was 1.32. Because the polymer prepared under these con-ditions had the highest [η] value, it was advisable to investigate polycondensation at the found optimum ratio, but at higher both monomer concentrations and content of phosphorus pentoxide. As shown in reference [37], the use of additional amounts of P_2O_5 leads to a considerable increase in the molecu-lar masses of the polymers.

Experiments demonstrated that the addition of P_2O_5 during polycondensation resulted in the formation of polymers showing limited solubility in conventional organic solvents, although this reaction occurred under homogeneous conditions. However, if addi-tional amounts of the dehydrating agent were added at the reaction onset (immediately during prepara-tion of the reaction solution) well soluble polymers were formed. It was shown (Figure 6) that the high-est molecular mass products are formed at a mono-mer concentration of 1.0 mol/L ([η] = 0.51 dL/g).
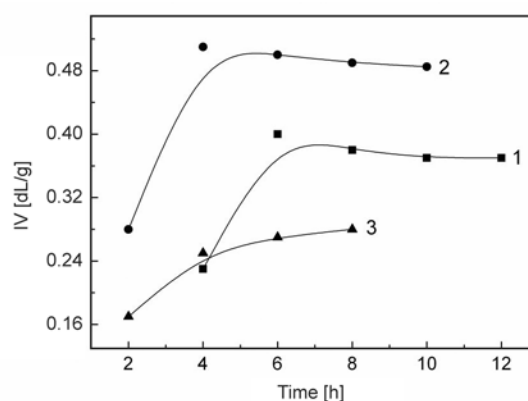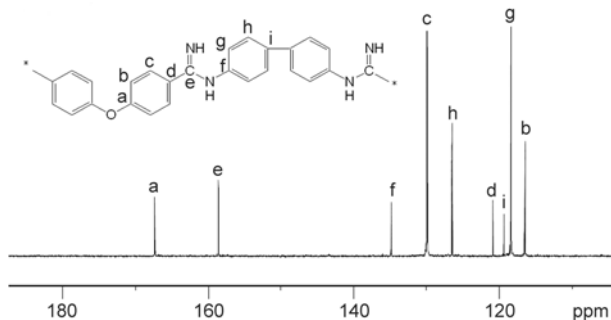

Figure 6. Effect of reaction time and monomer concentra-tion on IV of PAD **4a** obtained by the polycon-densation in ER (mole ratio monomer/P_2O_5 = 1/1.32), at 120°C and monomer concentrations of 0.8 (1), 1.0 (2), 1.2 (3) mol/L

With allowance for the found optimum conditions (*T* = 120°C, *t* = 4–5 h, a phosphorus pentoxide to monomer molar ratio of 1.32, and a monomer con-centration of 1 mol/L), various PADs were synthe-sized via the above described Figure 5.

The polycondensation of 4,4′-oxybis(benzoic acid) diamide and a number of aromatic diamines occurred under homogeneous conditions and produced PADs with high yields and [η] = 0.23–0.65 dL/g (Table 3). However, in the case of diamides of iso- and tereph-thalic acids and diamines, only low-molecular-mass products were obtained. This fact makes it possible to assume that imino carbocations –C_6H_4–C^+=NH serve as active intermediates in polycondensation. In fact, the best results were attained in the case of 4,4′-oxybis(benzoic acid) diamide, which forms an imino carbocation stabilized by an electron-donor ether group. In the case of diamides of iso- and terephthalic acids, the formation of imino carboca-tions is extremely difficult because of the presence of

Table 3. Characteristics of polyamidines obtained from 4,4′-oxybis(benzoic acid) diamide and diamines in Eaton's regent

№	PAD	IV[a] [dL/g]	Decomposition temperature[b] [°C]
1	4a	0.51[c]	268
2	4b	0.48	280
3	4c	0.44	274
4	4d	0.65[d]	269
5	4e	0.23	246

[a]Measured in DMF at 20°C
[b]Temperature of 10 % weight loss determined by TGA at a heating rate of 5°C/min
[c]M_w = 20 000 g/mol, M_w/M_n = 1.56 (GPC)
[d]M_w = 25 000 g/mol, M_w/M_n = 1.54 (GPC). Film properties: tensile strength (σ) = 32.1 MPa, elongation (ε) = 3.5%.

electron-acceptor groups. Similar relationships were observed in references [34–36] for the synthesis of polybenzazoles and poly(ether ketones) in Eaton's reagent.

Thus, high-molecular-mass PADs may be easily prepared via the direct polycondensation of 4,4′-oxybis (benzoic acid) diamide with various diamines in Eaton's reagent. This approach differs from conventional procedures by a high rate of polymer formation and mild reaction conditions.

3.1.3. Characterization of polyamidines

The structures of PADs were investigated by a combination of elemental analysis, IR investigation, and ^{13}C NMR spectroscopy. The chemical shift of the amidine carbon atom is observed in the ^{13}C NMR spectrum at ≈158 ppm. Typical NMR spectrum of PAD **4b** is presented in Figure 7. Elemental analysis data are in a good agreement with the calculated values. The IR spectra of the polymers show characteristic absorption bands at 1608–1615 (C=N), 1360–1370 (C–N), and 3500–2500 (N–H, C$_{Ar}$–H)

cm^{-1}, thereby indicating the formation of amidine functional groups [38].

The thermal properties of PADs were evaluated via TGA in the air and argon atmospheres and the data are summarized in Tables 2 and 3. All the samples used for studying the TGA were subjected to exhaustive drying in a vacuum oven at 60°C. Typical TG curves of PADs **4b** and **1b** are shown in Figure 8. For all the samples two distinct different weight losses on TG curves on air are observed. We believe that oxidative dehydrocyclization of PAD in more thermally stable PBI under the action of oxygen occurs during TG experiment on air. In argon atmosphere one-step degradation of PADs is observed, which indirectly indicates the formation of benzimidazole rings during TGA in the presence of oxygen. These assumptions, however, need to be further examined with more effective characterization techniques. The 10% weight loss temperatures both in air and argon were at around 246–288°C.

The polymers are fully soluble in concentrated sulfuric acid, concentrated formic acid and in polar organic solvents (DMF, DMAA, MP, THF, etc.) at room temperature or under slight heating. Moreover, all of the synthesized polymers are soluble in a mixture of 1N aqua HCl/methanol (1/1, v/v). Solubility of polymers in conventional organic solvents allowed to determine their molecular masses by GPC. As noted in Tables 2 and 3 the PADs have moderate molecular masses (M_w) up to 25 000 g/mol. Films prepared by casting of polymer solutions in DMF had tensile strength of 29.5–32.1 MPa and elongation of 3.5–4.2%.

Figure 7. NMR ^{13}C spectrum of PAD **4b**
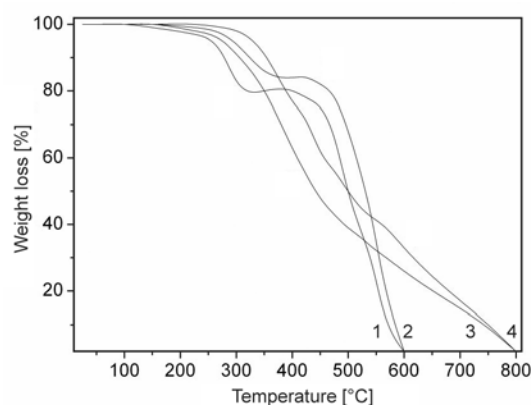
Figure 8. TG curves of PADs **4b** (1, 3) and **1b** (2, 4) in air and argon atmosphere, respectively

3.2. Preparation of polybenzimidazoles by oxidative dehydrocyclization of polyamidines

Practical importance of synthesized PADs increases if they can be used as precursors for the preparation of high-performance PBIs. Therefore, it seemed appropriate to study oxidative dehydrocyclization of these PADs in detail (Figure 9) and to analyze the operation characteristics of PBI membranes prepared by this procedure.

The idea of preparing benzimidazole from N-aryl substituted amidine hydrochloride (proposed by Grenda *et. al.* [39]) consist in generation from the azomethine bond in amidine hydrochloride of an uncharged electron-deficient species, nitrene, which, being extremely reactive, undergoes addition at the *o*-position of the benzene ring, thus closing the benzimidazole heterocycle.

In order to investigate the oxidative dehydrocyclization, transformation of PAD **2a** was studied in detail. Also cyclization of PAD **4d** was carried out under the optimal reaction conditions.

The transformation was performed in solution using hydrogen peroxide or sodium hypochlorite as oxidants. The PAD was converted to the soluble form using 1 M aqueous HCl and methanol. After vigorous stirring with heating for 30 min, the polymer dissolved virtually fully. Subsequent addition of the oxidant caused formation of a precipitate, which was dissolved by adding a small amount of DMF. To initiate the generation of nitrenes, we added to the reaction mixture 6 M aqueous KOH and heated to 100°C.

The course of oxidative dehydrocyclization was monitored by IR spectroscopy (Figure 10), namely, by changes in the intensities of the characteristic absorption bands of the N–H (3400 and 3050 cm^{-1}) and C–N (1360–1365 cm^{-1}) groups. The other char-
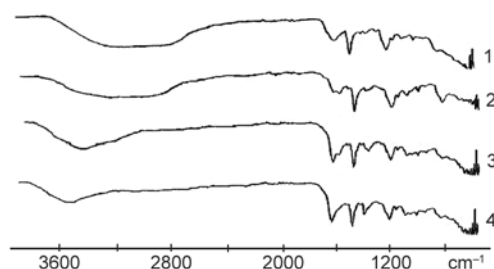

Figure 10. Evolution of the FTIR spectrum of PAD in the course of its transformation into PBI: PAD (1), intermediate states (2, 3), and PBI (4)

acteristic changes observed in the spectrum are shift of the C=N absorption band at 1610 cm^{-1} ($\Delta \nu = 20$ cm^{-1}), caused by transformation of the acyclic form into the cyclic form, and appearance of a new band at 730 cm^{-1}, corresponding to 1,2-disubstituted benzene ring.

A study of the PAD transformation showed that the degree of conversion was not noticeably influenced by the polymer concentration in solution and by its molecular weight, whereas the oxidant content exerted appreciable influence. For example, when hydrogen peroxide was taken in an equimolar amount relative to PAD repeat unit, only 70% conversion was attained in 8 h (Figure 11, curve 4), after that the reaction became very slow. Threefold excess of the oxidant led to practically complete conversion in 6 h at 80°C (Figure 11, curve 2). It is interesting that the rates in both processes in the first hour were similar, but then the kinetics became different, apparently because of hindered diffusion in the polymer solution and limited accessibility of the amidine bond in the polymer chain to the oxidant molecules. With sodium hypochlorite used instead of hydrogen peroxide (Figure 11, curve 3), the cyclization rate slightly decreased. The maximal rate was attained with increasing temperature to 100°C: the cyclization was complete in 4 h (Figure 11, curve 1). Further increase
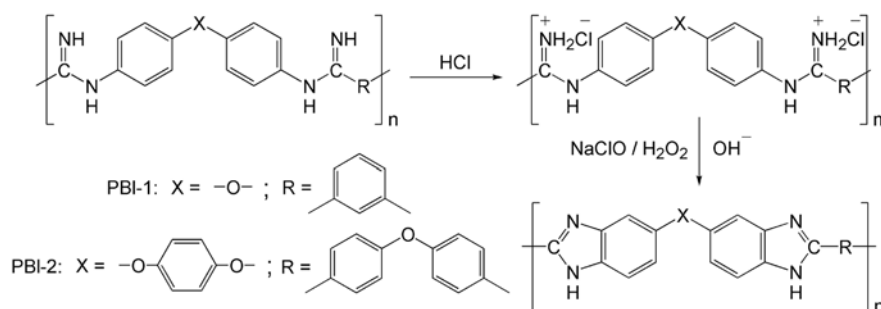

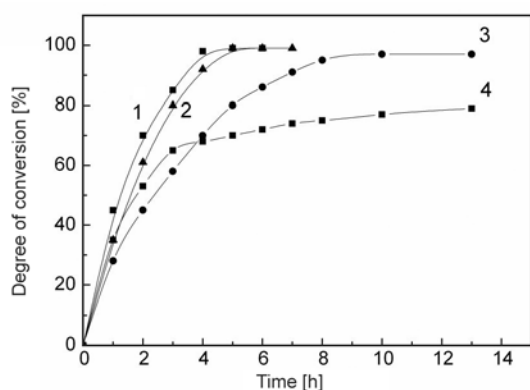**Figure 9.** Oxidative dehydrocyclization of polyamidines in polybenzimidazoles

Figure 11. Degree of conversion γ of PAD into PBI as a function of time τ: [NaClO]/[PAD] = 3, 100°C (1); [H$_2$O$_2$]/[PAD] = 3, 80°C (2); [NaClO]/[PAD] = 3, 80°C (3) and [H$_2$O$_2$]/[PAD] = 1, 80°C (4)

in temperature led to considerable deceleration of the reaction, probably because of decomposition of sodium hypochlorite.

The structure of thus obtained PBI-1 was confirmed by IR spectroscopy (Figure 10): characteristic absorption bands of 1,2-disubstituted benzene ring at 730 cm^{-1} and of C=N (1630 cm^{-1}) and C–N (1360 cm^{-1}) bonds are observed. In the ^{13}C NMR spectrum of PBI-1, compared to those of the pristine PAD, new signals at 134.6 ppm appear, confirming formation of the *o*-substituted aromatic ring; in addition, the signal of the amidine carbon atom at 158.6 ppm transforms into the signal of the benzimidazole carbon atom at 152.1 ppm.

According to TGA, the temperature of 10% weight loss on air for PBI-1 is 490°C whereas for corresponding PAD this value is 275°C. This fact also indirectly confirms the occurrence of cyclization.

PBI-2 was obtained similar to PBI-1 using sodium hypochlorite as oxidant at 100°C.

The viscosity characteristics of PBIs suggest that the transformation of PADs is not accompanied by a change in their molecular weights.

Both obtained PBIs are fully soluble in concentrated sulfuric and formic acids and dissolve in amide solvents at slight heating. By casting 10–15% solutions of PBIs in DMF onto glass supports, we obtained films with tensile strength of 68.0–71.6 MPa and elongation of 2–3%.

One of the most practically important properties of membranes based on PBI is ionic conductivity, allowing their use in fuel cells. However, doping the PBI-1 with orthophosphoric acid drastically decreased the strength of the membrane, making it practically unsuitable for use. For example, tensile strength of

membrane decreased by 67.5%, becoming as low as 23.27 MPa. Therefore, to improve the strength characteristics of film materials, we performed structuring of PBI with three-dimensional PAIR prepared from N,N′-(4,4′-diphenylmethane) bis-maleimide and 4,4′-diaminodiphenylmethane. For this purpose, we mixed solutions of PBI and PAIR, prepared film materials, and heat-treated them at 230°C for 7 h. Opening of the unsaturated bond of the terminal maleimide ring led to the formation of a 3D network in which PBI was retained owing to mechanical interweaving of macromolecular chains. It should be noted, however, that intermolecular interaction of the C=C bonds of the resin with secondary amino groups of the benzimidazole ring of PBI, with the formation of a graft copolymer, can occur along with PAIR polymerization. Correspondingly, we observed in the IR spectra a low-frequency shift of the absorption band of the carbonyl groups, caused by formation of the less strained succinimide ring. Thus, we prepared film materials with satisfactory strength characteristics from the PBI–PAIR blends of various compositions (Figure 12).

As seen from the obtained data, addition of 10 wt% PAIR to PBI results in a sharp increase in the tensile strength. Further increase in the amount of the resin in a blend with both PBIs leads to a decrease in the film strength. Obviously, the 90:10 weight ratio of PBI and PAIR in the blend is optimal. The 90:10 PBI-1–PAIR membrane was doped with 9M orthophosphoric acid to constant weight. After that, the strength characteristics decreased by only 10–15%, and the ionic conductivity of the membrane was 1.15·10^{-3} S/cm. With an increase in temperature, the membrane conductivity also increased with the activation energy of 28±2 kJ/mol, reaching 3·10^{-2} S/cm
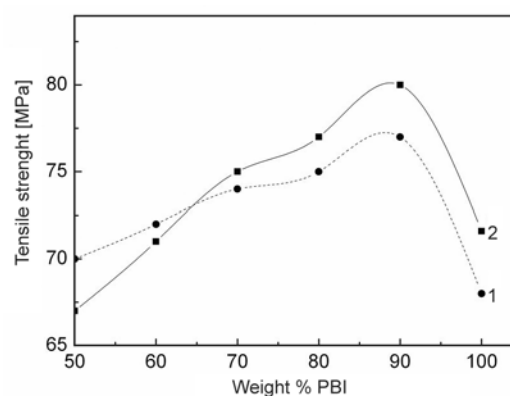

Figure 12. Tensile strength as a function of composition of PBI–PAIR blends. PBI-1 (1) and PBI-2 (2)
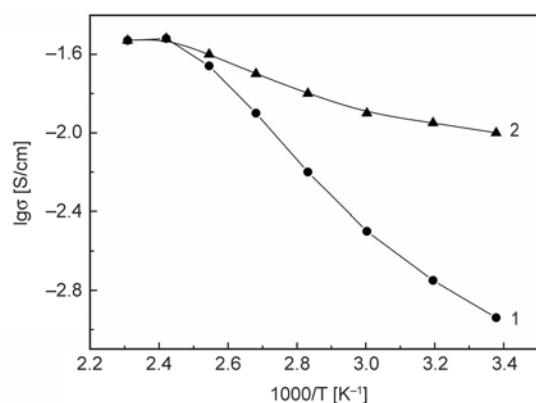
Figure 13. Temperature dependence of the ionic conductivity σ of the 90:10 PBI–PAIR membrane doped with phosphoric acid (1) and of the same membrane additionally modified with acidic zirconium phosphate (2)

at 160°C (Figure 13, curve 1). These values are similar to the conductivity of conventional membranes based on PBIs. However mechanical properties of doped blend membrane of PBI and PAIR are considerably higher than those of common membranes on the base of PBIs [15].

It is interesting that additional treatment of the doped membrane with acidic zirconium phosphate leads to an increase in the conductivity at low temperatures by almost an order of magnitude ($1.0 \cdot 10^{-2}$ S/cm at 23°C) and to a decrease in the activation energy to 8.5 ± 0.5 kJ/mol. However, further increase in temperature leads to only a slight increase in the conductivity, and already at 120°C the conductivities of the doped membrane and membrane treated with zirconium phosphate become virtually equal, varying synchronously on further heating (Figure 13, curve 2). Presumably, an increase in the low-temperature ionic conductivity of the membranes modified with acidic zirconium phosphate is due to the high intrinsic ionic conductivity of finely dispersed $Zr(HPO_4)_2 \cdot nH_2O$ [40] and to sorption processes occurring at the boundary of the organic and inorganic phases [41].

4. Conclusions

We showed that aromatic PADs with moderate molecular weights could be prepared by polyaddition of dinitriles and diamines in acidic ILs. It has been shown that nature of ionic solvent influences on inherent viscosities of resulting polymers. Also we were able to regenerate ionic solvent after polyaddition. Moreover we developed new method of synthesis of such polymers consisting in polycon-

densation of 4,4′-oxybis(benzoic acid) diamide and diamines using ER. Molecular weights of synthesized polymers reached 25 000 g/mol, and 10% weight losses were up to 288°C, films prepared by casting of PADs solutions in DMF had satisfactory mechanical properties. Resulted PADs were used as precursors for preparation of aromatic PBIs by oxidative dehydrocyclization. It was found that the degree of conversion was not noticeably influenced by the polymer concentration in solution and by its molecular weight, whereas the oxidant content exerted appreciable influence. After doping with phosphoric acid, the ionic conductivity of blend membrane of PBI and PAIR reaches $3 \cdot 10^{-2}$ S/cm at 160°C. Additional treatment of the doped membrane with acidic zirconium phosphate leads to an increase in the conductivity at low temperatures by almost an order of magnitude ($1.0 \cdot 10^{-2}$ S/cm at 23°C) and to a decrease in the activation energy to 8.5 ± 0.5 kJ/mol.

References

 [1] Wang Z-T., Zhang Y-S., Zhao Y-X., Zhu G-M.: Recent progress of polyamidine (in Chinese). Polymer Materials Science and Engineering, **23**, 6–9 (2007).
 DOI: 10.3321/j.issn:1000-7555.2007.05.002
 [2] Nikolaeva M. N., Osadchev A. Yu.: Supramolecular structure of the polyamidine-bisphenol system. Russian Journal of Applied Chemistry, **78**, 613–616 (2005).
 DOI: 10.1007/s11167-005-0353-5
 [3] Aleksandrova E. L., Dudkina M. M., Ten'kovtsev A. V.: A mechanism of charge-carrier photogeneration in polyamidine supramolecular structures. Semiconductors, **38**, 1284–1290 (2004).
 DOI: 10.1134/1.1823060
 [4] Dudkina M. M., Tenkovtsev A. V., Komber H., Häussler L., Böhme F.: Competitive influence of carboxylic groups in ionic complex formation of 4-hydroxybenzylidene alkanones with polyamidines. Macromolecules, **37**, 8389–8393 (2004).
 DOI: 10.1021/ma049466i
 [5] Tang R., Ji W., Wang C.: Synthesis and characterization of new poly(ortho ester amidine) copolymers for non-viral gene delivery. Polymer, **52**, 921–932 (2011).
 DOI: 10.1016/j.polymer.2010.12.057
 [6] Hwang S. J., Bellocq N. C., Davis M. E.: Effects of structure of β-cyclodextrin-containing polymers on gene delivery. Bioconjugate Chemistry, **12**, 280–290 (2001).
 DOI: 10.1021/bc0001084
 [7] Böhme F., Klinger C., Komber H., Häußler L., Jehnichen D.: Synthesis and properties of polyamidines. Journal of Polymer Science Part A: Polymer Chemistry, **36**, 929–938 (1998).
 DOI: 10.1002/(SICI)1099-0518(19980430)36:6<929::AID-POLA8>3.0.CO;2-B

[8] Toktonov A. V., Mognonov D. M., Mazurevskaya Zh. P., Botoeva S. O.: Synthesis of polyamidines based on aromatic bis(imidoyl) chlorides in solution. Polymer Science Series A, **48**, 1–10 (2006).
DOI: 10.1134/S0965545X06010019

[9] Ogata S-I., Kakimoto M-A., Imai Y.: Direct synthesis of new aromatic polyamidines from aromatic diamines and benzoic acids by using poly(trimethylsilylphosphate). Die Makromolekulare Chemie, Rapid Communications, **6**, 835–839 (1985).
DOI: 10.1002/marc.1985.030061208

[10] Sharavanan K., Komber H., Böhme F.: Synthesis and properties of aliphatic polyacetamidines. Macromolecular Chemistry and Physics, **203**, 1852–1858 (2002).
DOI: 10.1002/1521-3935(200208)203:12<1852::AID-MACP1852>3.0.CO;2-5

[11] Lee I-H., Kim H., Choi T-L.: Cu-catalyzed multicomponent polymerization to synthesize a library of poly (*N*-sulfonylamidines). Journal of the American Chemical Society, **135**, 3760–3763 (2013).
DOI: 10.1021/ja312592e

[12] Gol'din G. S., Poddubnyi V. G., Fedorov S. G., Fedotova T. P.: Method for producing polyamidines. SU Patent 248972, USSR (1969).

[13] Fuks R.: *N*-alkylation of nitriles[1]–II. Synthesis polymerization and quaternization of *N*-substituted acrylamidines. A new class of acrylic monomers[16]. European Polymer Journal, **9**, 835–845 (1973).
DOI: 10.1016/0014-3057(73)90016-5

[14] Brand R. A., Bruma M., Kellman R., Marvel C. S.: Low-molecular-weight polybenzimidazoles from aromatic dinitriles and aromatic diamines. Journal of Polymer Science: Polymer Chemistry Edition, **16**, 2275–2284 (1978).
DOI: 10.1002/pol.1978.170160916

[15] Li Q., Jensen J. O., Savinell R. F., Bjerrum N. J.: High temperature proton exchange membranes based on polybenzimidazoles for fuel cells. Progress in Polymer Science, **34**, 449–477 (2009).
DOI: 10.1016/j.progpolymsci.2008.12.003

[16] Barton D., Ollis W. D.: Comprehensive organic chemistry. Vol 2: Nitrogen compounds. Pergamon, Oxford (1979).

[17] Jacques R., Reppelin M., Seigneurin L.: Preparation of aromatic/aliphatic nitriles. U.S. Patent 4436669, USA (1984).

[18] DeCastro C., Sauvage E., Valkenberg M. H., Hölderich W. F.: Immobilised ionic liquids as lewis acid catalysts for the alkylation of aromatic compounds with dodecene. Journal of Catalysis, **196**, 86–94 (2000).
DOI: 10.1006/jcat.2000.3004

[19] Eaton P. E., Carlson G. R., Lee J. T.: Phosphorus pentoxide-methanesulfonic acid. Convenient alternative to polyphosphoric acid. Journal of Organic Chemistry, **38**, 4071–4073 (1973).
DOI: 10.1021/jo00987a028

[20] Farion I. A., Mognonov D. M., Il'Ina O. V., Bal'Zhinov S. A.: Crosslinking benzotriazolylimides and polymeric materials on base of them. Journal of Applied Polymer Science, **126**, 1797–1807 (2012).
DOI: 10.1002/app.34475

[21] Oxley P., Partridge M. W., Short W. F.: Amidines. Part VII. Preparation of amidines from cyanides, aluminium chloride, and ammonia or amines. Journal of the Chemical Society, **1947**, 1110–1116 (1947).
DOI: 10.1039/JR9470001110

[22] Cooper F. C., Partridge M. W.: N-phenylbenzamidine. Organic Syntheses, **4**, 769–533 (1963).

[23] Oxley P., Short W. F.: Amidines. Part I. Preparation of amidines from cyanides. Journal of Chemical Society, **1946**, 147–150 (1946).
DOI: 10.1039/JR9460000147

[24] Wasserscheid P., Welton T.: Ionic liquids in synthesis. Wiley-VCH, Weinheim (2007).

[25] Boon J. A., Lander S. W., Levisky J. A., Pflug J. L., Skrznecki-Cooke L. M., Wilkes J. S.: Catalysis and reactivity of electrophilic reactions in room temperature chloroaluminate molten salts. in 'Proceedings of the Joint International Symposium on Molten Salts, Pennington, USA' 979–990 (1987).

[26] Boon J. A., Levisky J. A., Pflug J. L., Wilkes J. S.: Friedel-Crafts reactions in ambient-temperature molten salts. Journal of Organic Chemistry, **51**, 480–483 (1986).
DOI: 10.1021/jo00354a013

[27] Piersma B. J., Merchant M.: Friedel-Crafts alkylation reac-tions in a room temperature molten salt. in 'Proceedings of the 7th International Symposium on Molten Salts, Montreal, Canada' 805–821 (1990).

[28] Newman D. S., Kinstle T. H., Thambo G.: The acylation of coal and model coal compounds in room temperature molten salts. in 'Proceedings of the Joint International Symposium on Molten Salts, Pennington, USA' 991–1001 (1987).

[29] Vygodskii Y. S., Lozinskaya E. I., Shaplov A. S.: Ionic liquids as novel reaction media for the synthesis of condensation polymers. Macromolecular Rapid Communications, **23**, 676–680 (2002).
DOI: 10.1002/1521-3927(20020801)23:12<676::AID-MARC676>3.0.CO;2-2

[30] Vygodskii Y. S., Lozinskaya E. I., Shaplov A. S., Lyssenko K. A., Antipin M. Y., Urman Y. G.: Implementation of ionic liquids as activating media for polycondensation processes. Polymer, **45**, 5031–5045 (2004).
DOI: 10.1016/j.polymer.2004.05.025

[31] Lozinskaya E. I., Shaplov A. S., Vygodskii Ya. S.: Direct polycondensation in ionic liquids. European Polymer Journal, **40**, 2065–2075 (2004).
DOI: 10.1016/j.eurpolymj.2004.05.010

[32] Mallakpour S., Yosefian H.: Direct polyamidation in molten tetrabutylammonium bromide: Novel and efficient green media. Polymer Bulletin, **60**, 191–198 (2008).
DOI: 10.1007/s00289-007-0855-9

[33] Kholkhoev B. C., Burdukovskii V. F., Mognonov D. M.: Polyamidines based on dinitriles and diamines. Russian Journal of Applied Chemistry, **84**, 510–511 (2011). DOI: 10.1134/S1070427211030311

[34] Ueda M., Sato M., Mochizuki A.: Poly(benzimidazole) synthesis by direct reaction of diacids and diamines. Macromolecules, **18**, 2723–2726 (1985). DOI: 10.1021/ma00154a060

[35] Ueda M., Sato M.: Synthesis of aromatic poly(ether ketones). Macromolecules, **20**, 2675–2678 (1987). DOI: 10.1021/ma00177a007

[36] Rusanov A. L., Komarova L. G.: Synthesis of heterochain and heterocyclic condensation polymers in novel reaction media. Polymer Science Series B, **47**, 284–303 (2005).

[37] Ponomarev I. I., Rybkin Yu. Yu., Volkova Y. A., Razorenov D. Yu.: Method for producing polybenzimidazoles based on 4,4′-diphenylphthalide-dicarboxylic acid. International Patent WO2008/103066 (2008).

[38] Pretsch E., Buhlmann P., Affolter C.: Structure determination of organic compounds. Springer, Berlin (2000).

[39] Grenda V. J., Jones R. E., Gal G., Sletzinger M.: Novel preparation of benzimidazoles from N-arylamidines. New synthesis of thiabendazole. Journal of Organic Chemistry, **30**, 259–262 (1965). DOI: 10.1021/jo01012a061

[40] Casciola M., Bianchi D.: Frequency response of polycrystalline samples of $\alpha-Zr(HPO_4)_2 \cdot H_2O$ at different relative humidities. Solid State Ionics, **17**, 287–293 (1985). DOI: 10.1016/0167-2738(85)90073-6

[41] Volkov V. V., Mchedlishvili B. V., Roldugin V. I., Ivanchev S. S., Yaroslavtsev A. B.: Membranes and nanotechnologies. Nanotechnologies in Russia, **3**, 656–687 (2008). DOI: 10.1134/S1995078008110025

Electrogenerated networks from poly [4-(diphenylamino)benzyl methacrylate] and their electrochromic properties

O. I. Negru[*], *L. Vacareanu, M. Grigoras*

'P. Poni' Institute of Macromolecular Chemistry, Electroactive Polymers Department, 41A Gr. Ghica Voda alley, Iasi-700487, Romania

Abstract. Poly[4-(diphenylamino)benzyl methacrylate] with well-defined molecular weight and low polydispersity was prepared by atom transfer radical polymerization (ATRP) using 4-(diphenylamino) benzyl 2-bromo-2-methyl-propanoate as initiator and CuBr/2,2′-bipyridine as catalytic complex. Electrochemical behavior and optical properties of the polymers were investigated by cyclic voltammetry and UV-Vis and fluorescence spectroscopy. Cyclic votammetric studies revealed that the redox processes were accompanied by dimerization of triphenylamine pendant groups. The initial polymer was post-modified, in solution or bulk, by electrochemical oxidation leading to a crosslinked and insoluble network with electrochromic properties, accompanied by strong color changes with high coloration efficiency. The crosslinking reaction took place between triphenylamine groups through *para* free positions leading to tetraphenylbenzidine bridges. The structure of polymers was confirmed by Fourier transform infrared (FT-IR) spectroscopy and ^{1}H and ^{13}C-nuclear magnetic resonance spectroscopy. Morphology studies of the cross-linked film have evidenced a smooth and continuous aspect without any pin-holes or defects.

Keywords: *polymer synthesis, triphenylamine-based polymers, crosslinking, electrochromic networks*

1. Introduction

Conjugated polymers have been extensively investigated in the last decades and continue to attract scientific interest due to their wide range of applications. Among the large variety of conjugated polymers, triphenylamine-based oligomers and polymers have received much attention because they have good hole-transporting properties, high light-emitting efficiencies, photoconductivity and photorefractivity, large two-photon absorption cross-section, being attractive materials for optoelectronic applications [1–3]. Responsible for all these properties is triphenylamine, a well-known molecule that possesses interesting functions such as redox activity, fluorescence, high oxidability of nitro-

gen center and good hole-transporting properties via radical-cation species [4]. Thus, oligomers and polymers containing triphenylamine group in the main or side chain have found applications as photoconducting materials in xerography, organic field-effect transistors, photorefractive systems, light emitting diodes [5–7], solar cells [8, 9] or electrochromic materials [10, 11].

Electrochromic materials have ability to change reversible their absorption and transmittance upon electrochemical oxidation or reduction. For electrochromic applications these materials have to possess good film-forming properties, long-term stability, high coloration efficiency and fast switching of color. To increase the long-term stability an efficient

---

route is to use cross-linked materials. Electrochromic networks can be obtained as films with fine control of the layer thickness from vinyl polymers containing carbazole or triphenylamine substituents by anodic oxidation [12–14]. Generally, vinyl polymers that contain pendant chromophore groups (carbazole, triphenylamine, etc.) have greater solubility than rigid-rod conjugated polymers, facilitating thus their processing as thin films from solution. In the class of carbazole-based polymers, an important place is taken by poly (N-vinylcarbazole) (PVK) because it is easily synthesized and soluble in common organic solvents [15]. The controlled radical polymerizations of N-vinyl carbazole (VK) monomers are considered to be difficult because radical precursors are highly reactive due to the nature and strong electron donating pendant groups [16, 17]. Nevertheless, several attempts to synthesize PVK using various controlled radical polymerization systems have been reported in the literature. Polymerization *via* reversible addition-fragmentation chain transfer (RAFT) can be only readily mediated using xanthates or dithiocarbamate as the chains transfer agent [16, 18–21] or nitroxide-mediated polymerization (NMP) [22] and by atom transfer radical polymerization (ATRP) [23, 24].

Several attempts for synthesis of vinyl polymers having triphenylamine as pendant groups, using controlled radical polymerization (NMP [25–28] and RAFT [29–32]) or living anionic route [33–40] have been recently reported. However, the controlled radical polymerization of triphenylamine-based (meth) acrylate monomers was less studied until now, only a paper revealing the group transfer polymerization of 4-(dimethylamino)benzyl methacrylate was published [41]. As a continuation of our previous studies regarding controlled radical polymerization of arylamine-based vinyl monomers [19, 42, 43], in this paper we have reported the synthesis and characterization of poly [4-(diphenylamino) benzyl methacrylate] employing the atom transfer radical polymerization method. This polymer was used in the next step in order to obtain electrochromic networks by electrochemical crosslinking of triphenylamine pendant sites.

2. Experimental
2.1. Materials
Methacryloyl chloride (97%), triethylamine (99,5%), copper (I) bromide (CuBr, 99,99%), 2,2-bipyridine (bpy) (98%) and tetrabutylammonium tetrafluoroborate (TBABF$_4$) were purchased from Aldrich (Steinheim, Germany) and used without further purification. Solvents (Aldrich) were dried by usual methods or used as received. 4-(diphenylamino) benzyl alcohol and 4-(diphenylamino) benzyl 2-bromo-2-methylpropanoate, were synthesized according to the reported methods [42].

2.2. Measurements
The infrared spectra of the polymers were recorded on FT-IR Bruker Vertex 70 Spectrophotometer in transmission mode using KBr pellets (Ettlingen, Germany). UV-Vis absorption and fluorescence spectra of polymers were recorded with a Specord 200 spectrophotometer (Analytik Jena AG, Jena, Germany) and Perkin Elmer LS 55 apparatus (United Kingdom), respectively, by using diluted polymer solutions and very thin films deposited on quartz plates by drop-cast technique. ^{1}H and ^{13}C-NMR spectra were recorded on a Bruker NMR spectrometer, Avance DRX 400 MHz (Rheinstetten, Germany), using deuterated chloroform (CDCl$_3$) and tetramethylsilane as an internal standard. Gel permeation chromatography (GPC) analyses were carried out on PL-EMD 950 Evaporative light Detector instrument using chloroform (CHCl$_3$) as an eluent phase and standard polystyrene sample for calibration. Samples were filtered through 0.45 μm syringe. The surface investigation was performed using atomic force microscopy (AFM) solver PRO-M (NT-MDT, Russia). Thin film of the cross-linked polymer was deposited upon ITO coated. Differential scanning calorimetry (DSC) measurements were conducted on a Pyris Diamond DSC, Perkin Elmer (USA), in nitrogen with a heating and cooling rate of 10°C/min. The glass transition temperatures (T_g) were determined from the second heating run.

Electrochemical studies were carried out with a Bioanalytical System, Potentiostat–Galvanostat (BASi 100B/W, SUA, Indiana, West Lafayette). All the experiments were performed in a one-compartment cell using a standard three-electrode cell arrangement with a working platinum electrode, an auxiliary electrode (platinum wire), and a reference electrode (consisted of a silver wire coated with AgCl). Before each experiment, the Pt working electrode was cleaned by polishing it successively with 0.3 and 0.05 μm Al$_2$O$_3$ slurry on emery paper to a mirror finish, and then washed with methanol and bi-dis-

tilled water. The electrochemical studies were carried out both in solution and film deposited on platinum electrode and tetrabutylammonium tetrafluorobo-rate (TBABF$_4$) as supporting electrolyte.

Electro-optical properties were investigated using an indium tin oxide (ITO, Adrich Sigma Aldrich with an active area of 1.1 cm×0.8 cm) electrode as well as a platinum wire as counter electrode and an AgCl reference electrode. A film of the cross-linked polymer was deposited upon ITO coated glass electrode by electrochemical polymerization using a solution of polymer in acetonitrile/toluene (1:1) and TBABF$_4$ as electrolyte. The film was prepared by sweeping the potential between 0 and +1.8 V for 14 scan cycles and after deposition, the ITO/polymer film was rinsed with distilled water and further used as working electrode in a standard spectroelectro-chemical cell (a quartz cuvette of 1cmx1cm dimen-sions) filled with supporting electrolyte (TBABF$_4$, solution 0.1M in acetonitrile/toluene, 1:1). The electrodes were connected to a BASi Potentiostat–Galvanostat and spectroelectrochemical spectra were recorded using an SEC-2000-UV/VIS-type spectrophotometer (Tokyo, Japan).

2.3. Synthesis of 4-(diphenylamino) benzyl methacrylate

Monomer was prepared according to the modified method described in the literature [44]. To a mix-ture of 4-(diphenylamino) benzyl alcohol (7.00 g, 25.42 mmol) and triethylamine (3.08 g, 4.05 mL, 30.5 mmol) in dry toluene (150 mL), methacryloyl chloride (3.18 g, 2.95 mL, 30.5 mmol) was slowly added at 0°C under argon atmosphere. The reaction mixture was then stirred for 24 h, at room tempera-ture. The Et$_3$N·HCl was separated by filtration and

the toluene solution was washed successively with Na$_2$CO$_3$ solution, water and finally dried on CaCl$_2$. After toluene evaporation in vacuum, monomer was purified by column chromatography (silica gel as stationary layer and a mixture of hexane: CH$_2$Cl$_2$ as eluent), giving 5.85 g (83%) as viscous oil. ^{1}H-NMR (CDCl$_3$, δ, ppm): 1.96 (s, 3H, –CH$_3$), 5.12 (s, 2H, –CH$_2$–O), 5.56 and 6.14 (s, 2H, =CH$_2$), 6.95–7.30 (m, 14H, aromatic protons). ^{13}C-NMR (CDCl$_3$, δ, ppm): 18.35, 66.17, 122.99, 123.91, 124.72, 125.68, 129.40, 129.80, 136.30, 147.58, 167.30.

2.4. Synthesis of poly [4-(diphenylamino) benzyl methacrylate]

An example for ATRP polymerization was as fol-lows (entry 2 in Table 1): In a two neck round bottom flask equipped with magnetic stirrer and nitrogen inlet-outlet, vacuumed and back-filled with nitrogen for several times, CuBr (8.48 mg, 0.059 mmol), 2,2-bipyridine (18.48 mg, 0.118 mmol), and the ATRP initiator (25.1 mg, 0.059 mmol) were added to a solu-tion of monomer (1.01 g, 2.95 mmol) in 3 mL toluene. The reaction mixture was degassed by nitro-gen for 60 min. The polymerization was carried out by immersing the flask into an oil bath thermostated at 103°C, for 24 hours. Then, the reaction mixture was precipitated twice in a large amount of cold hexane from dichloromethane. The polymer was fil-tered and dried at 40°C in vacuum. Yield = 33.1%. GPC measurements: M_n [g/mol] = 5370, M_w/M_n = 1.13.

3. Results and discussion
3.1. Synthesis

The atom transfer radical polymerization of 4-(diphenylamino)benzyl methacrylate monomer was

Table 1. Results and experimental conditions of polymerization of 4-(diphenylamino) benzyl methacrylate) using 4-(diphenylamino) benzyl 2-bromo-2-methylpropanoate as initiator in the presence of catalytic complex CuBr/bpy at 103°C

Sample	[Monomer]$_0$:[I]$_0$:[CuBr]$_0$:[bpy]$_0$	M_n th.$^{(a)}$ [g/mol]	$M_n^{(b)}$ [g/mol]	$M_w/M_n^{(b)}$	Yield [%]	T_g [°C]
P1	30:1:1:2	4330	4100	1.08	38.3	160
P2	50:1:1:2	6080	5370	1.13	33.1	161
P3	75:1:1:2	9400	8045	1.13	35.2	162
P4	150:1:1:2	9680	8920	1.18	18.6	162

$^{a)}$The theoretical number-average molecular weight is defined as follows:

$$\overline{M}_n\,(theor.) = \frac{[\text{Monomer}]_0}{[I]_0} \cdot M_{\text{Monomer}} \cdot \text{Conv.} + M_I$$

where: M_I and M_{Monomer} are the molecular weights of initiator (424) and of the monomer (343), and [Monomer]$_0$ and [I]$_0$ are the initial concentrations of the monomer and I, respectively. Conversion was determined by gravimetry.
$^{b)}$Number average molecular weight (M_n) and molecular weight distribution (M_w/M_n) are measured by gel permeation chromatography (GPC) using polystyrene as a standard in DMF.

carried out in dry toluene at 103°C temperature, in the presence of 4-(diphenylamino) benzyl 2-bromo-2-methylpropanoate as initiator and CuBr/bipyridyl as catalyst (Figure 1). This TPA-based initiator was previously used in ATRP polymerization of styrene to obtain triphenylamine end-functionalized polystyrenes with well-defined molecular weights and narrow polydispersities. The electrochemical and chemical oxidative polymerizations of these macromonomers led to soluble polytriphenylamine hairy-rod polymers having oligostyrene segments as grafts in every hairy structural unit [42]. On the other hand, this initiator was also used as monomer for interfacial and microemulsion chemical oxidative polymerization in the presence of ammonium peroxodisulfate as the oxidizing agent, obtaining functional polytriphenylamines [43]. In this paper, 4-(diphenylamino) benzyl 2-bromo-2-methylpropanoate was used as an ATRP initiator in controlled radical polymerization of methacrylate monomer containing triphenylamine moiety, (4-(diphenylamino)benzyl methacrylate) (TPMA) to get macromonomers with controlled molecular weight and narrow polydispersity index (Table 1). At the end of the polymerization reaction, the polymers were precipitated in hexane. They are completely soluble in organic solvents such as THF, DMF and in chlorinated solvents and have a well-defined molecular weight and narrow polydispersity. The polymers were purified by dissolution in a small amount of THF to which was added few drops of ammonium hydroxide (to prevent oxidation of nitrogen of the triphenylamine unit) and precipitated in hexane.

The molecular weight of the polymers was controlled by varying the $[\text{monomer}]_0/[\text{initiator}]_0$ ratios and these ratios were fixed in the range of 30 to 150, while all other experimental conditions were set to be the same. The M_n values proportionally increase by increasing the feed ratio and the polydispersity indices (M_w/M_n) for all samples are less than 1.2. In all cases, the molecular weights measured by GPC in D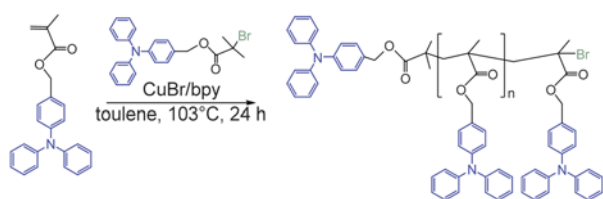MF, were lower than the theoretical values calculated from the monomer/initiator molar ratio and conversion of the monomer. The molecular weights obtained by conventional GPC using polystyrene calibration are just apparent values; moreover the conversion was approximated by gravimetry. The synthesized polymers have glass transition temperatures (T_g), determined by DSC at a heating rate of 10°C/min, in nitrogen atmosphere, after the second heating scan ranged between 160–162°C.

3.2. FT-IR and NMR spectra

The chemical structure of the polymer was proved by ^{1}H and ^{13}C-NMR and FT-IR measurements. In Figure 2 is shown the ^{1}H-NMR spectrum of poly [4-(diphenylamino) benzyl methacrylate] recorded in CDCl$_3$. By comparing both the ^{1}H-NMR spectrum for the monomer and polymer, in the last one it was observed the disappearance of the signals assigned to vinyl protons that in case of monomer spectra are located at 5.56 and 6.14 ppm region. At the same time, new signals emerge around 0.8 to 2.2 ppm, associated with the protons of poly [4-(diphenylamino) benzyl methacrylate] backbone, while the signals located at 4.85 ppm are assigned to methylene protons from the –CH$_2$–O- polymer segments. All other peaks are readily assigned on the pendant triphenylamine groups. Due to the structural similarity of both initiator and monomer, it was not possible to calculate the polymer molecular weight by using ^{1}H-NMR spectroscopy data. The ^{13}C-NMR spectral analysis of polymer, recorded in CDCl$_3$ shows the following signals: the region from 16.80 to 18.85 ppm is assigned to signals of methyl carbons (Ca), while the methylene carbon signals (Cb) are visible in 22.66 to 30.32 ppm region (Figure 3).
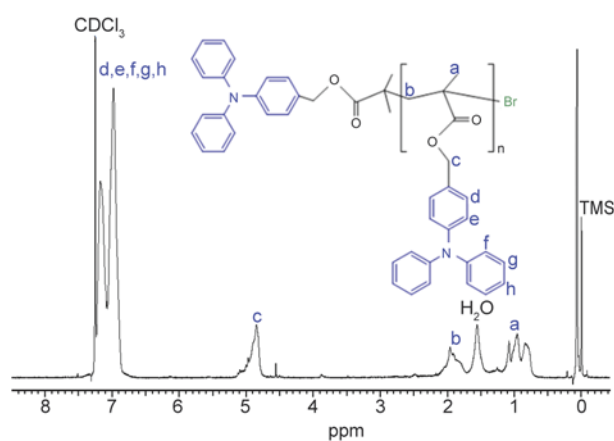

Figure 1. ATRP polymerization of 4-(diphenylamino)benzyl methacrylate

Figure 2. ^{1}H-NMR (CDCl$_3$) spectra of polymer

Figure 3. ^{13}C-NMR (CDCl$_3$) spectra of polymer

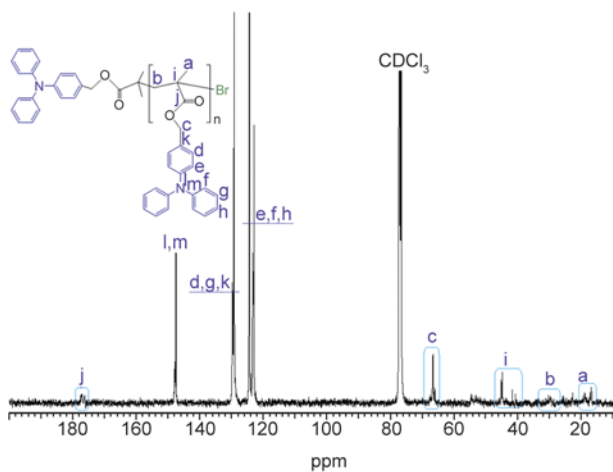**Figure 4.** FT-IR spectrum (KBr) of polymer

Quaternary carbons (Ci) show the signals in 40.69 to 44.18 ppm region, and the methylene carbons Cc are located at 66.64 ppm. Aromatic carbons located in the region 123.02 to 124.48 ppm are attributed to the carbon, Cf and Ch, while Cd, Cg, Ck are located in the region 128.86 to 129.77 ppm, and carbons Cl and Cm are located at 147, 95 and 147.60 ppm, respectively. The signals at 176.29 and 177.25 ppm are assigned to the Cj carbonyl carbon.

In Figure 4 is shown the FT-IR spectrum of the polymer. The bands assigned to the (H–C=) aromatic deformation vibrations are located at 3059 and 3033 cm^{-1}. The 2961 cm^{-1} band is characteristic to deformation vibration of the aliphatic (C–H) linkages. The band at 1729 cm^{-1} is attributed to the valence vibration of C=O bond while the bands located at 1140 and 1173 cm^{-1} are due to stretching vibrations of C–O–C bond. The bands at 1589 and 1492 cm^{-1} correspond to in-plane deformations of

aromatic rings. The bands at 1110 and 1028 cm^{-1} are assigned to the deformation vibration of the methyl and methylene groups. The spectrum shows a band of 1325–1273 cm^{-1} corresponding to the vibration of the C–N bond from the triphenylamine, and the bands at 753 and 695 cm^{-1} correspond to the out-of-plane deformation of the C–H monosubstituted benzene rings, while the band located at 806 cm^{-1} can be assigned to the C–H bond out-of-plane deformation from the 1,4-disubstituted benzene rings.

3.3. Optical properties

Absorption and emission spectra of polymer were recorded for polymers solution in dilute CHCl$_3$ (~10^{-5} M) and for thin film made from CHCl$_3$ solution (Figure 5). Absorption spectra for the polymer shows a single absorption band at 306 nm attributed to π-π* transitions of the triphenylamine pendant
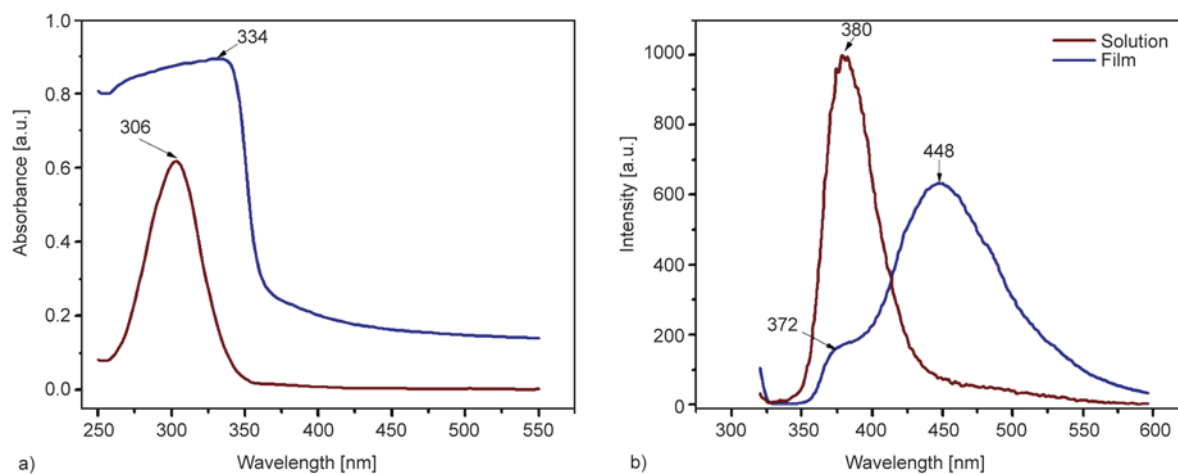

Figure 5. UV-Vis a) and fluorescence b) spectra of polymer recorded at an excitation wavelength of 306 nm. Sample/CHCl$_3$ = 0.100 mg/10 mL.

moiety. The polymer film cast from CHCl₃ exhibit main absorption maximum at 334 nm, which was found to be bathochromically shifted with 28 nm compared to the absorption of the polymer in solution state. The emission spectrum shows a single emission band at 370 nm for polymer solution and 448 nm for film, at an excitation wavelength of 306 nm. An identical red shift phenomenon was also observed for the emission spectra of polymer in solid state compared to polymer solution due to the intermolecular aggregation.

3.4. Electrochemical behavior

Electrochemical characteristics of polymer were investigated by running cyclic voltammogram. Thus, polymer (P2) was investigated by recording current intensity vs applied potential curves, for both solution state (using CH_2Cl_2 as solvent and $3.5 \cdot 10^{-3}$ M polymer concentration) and in film deposited on platinum electrode (using acetonitrile/toluene 1:1 solvent mixture). The working electrode potential was swept on the 0.0 to 1.8 V with 50 mV·s⁻¹ scan rate, for 14 cycles. The multiple cyclic voltammograms of polymer are shown in Figure 6. As it can be seen, in the first scan recorded for the polymer in solution, the voltammogram shows two anodic peaks located at $E_{ox1} = 0.981$ V and $E_{ox2} = 1.299$ V and on the reverse scanning, two cathodic peaks located at $E_{red1} = 0.861$ V and $E_{red2} = 0.743$ V appeared. The anodic peaks correspond to the oxidation processes of the triphenylamine units from the polymer structure. The first anodic peak is attrib-

uted to one electron removal from the nitrogen atom of triphenylamine, leading to formation of the radical-cation. Being unstable, chemical coupling processes of the radical cations occurred in the next step with the loss of two protons, leading to neutral tetraphenylbenzidine (TPB) dimer formation [45–48]. Starting with the second scan, the peaks current intensities associated with tetraphenylbenzidine oxidation processes increase, while the oxidation peaks are overlapping.

The increase of the current peaks intensities with each running cycle is correlated with the progress of dimerization reaction and formation of a green colored electroactive polymer film on the electrode surface. The shift of the oxidation potential at higher values is due to the increase of the electrical resistance of the polymer film when over-potential was needed to overcome the resistance. The polymer film in the undoped state was washed with CH_2Cl_2, removed mechanically, and then was characterized by FT-IR spectroscopy (Figure 7).

The electrochemical behavior of the polymer P2 as thin film deposited on the Pt electrode surface by drop-cast from CH_2Cl_2 solution was also investigated. For this, it was recorded the cyclic voltammogram in acetonitrile/toluene (1:1) mixture solution containing TBABF₄ (10⁻¹ M) as supporting electrolyte (Figure 6b). The first cycle shows one large reversible anodic peak located in the 0.852 and 1.446 V, which seems to be composed of two overlapping anodic peaks, corresponding to two successive oxidation processes of triphenylamine units,
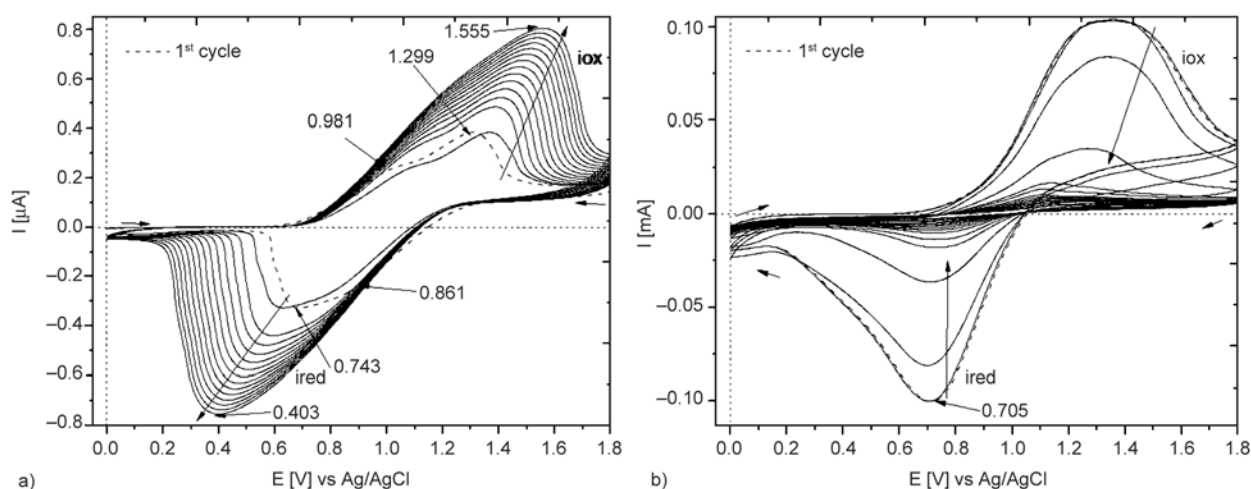

Figure 6. Multiple cyclic voltammograms (14 cycles) recorded for: a) polymer as CH_2Cl_2 solution, containing TBABF₄ (0.1 M) as supporting electrolyte, using Pt as working electrode (disk, diameter = 1.6 mm) and right) b) the polymer film deposited on Pt electrode surface and in acetonitrile/toluene (1:1) solvent mixture containing TBABF₄ (0.1 M) as supporting electrolyte; scan rate was 50 mV·s⁻¹

Table 2. The electrochemical data of polymer (P2)

Polymer	E_{ox}^{onset} [V]	E_{ox1} [V]	E_{ox2} [V]	E_{red}^{onset} [V]	E_{red1} [V]	E_{red2} [V]
CH$_2$Cl$_2$-solution	0.745	0.981	1.299	1.193	0.861	0.743
Film deposited on Pt	0.852	–	1.336	1.059	–	0.705
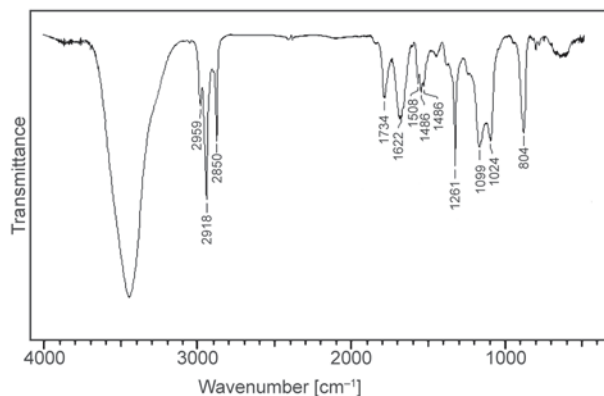
Figure 7. FT-IR spectra (KBr, cm^{-1}) of cross-linked polymer by electropolymerization in solution

while on the reverse scan only one cathodic peak appear at $E_{red} = 0.705$ V which is assigned to reduction process of the oxidized species. The large anodic peak can be due to a more reduced mobility of the electroactive sites in the solid state. At the end of 14 cycles, it was observed that the intensities of anodic and cathodic peaks currents decreased and this can be explained by the fact that during the electropolymerization process the triphenylamine units are consumed forming a cross-linking network. Comparing the onset oxidation potential values from both cases, it can be noted that the polymer is more easily oxidized as CH$_2$Cl$_2$-solution than as film (Table 2).

By comparing the FT-IR spectra of parent polymer (Figure 4) and cross-linked material (Figure 7) obtained by electropolymerization in solution, some differences can be evidenced:

– the disappearance of the characteristic bands 3059 and 3033 cm^{-1} assigned to the deformation vibrations of the (C–H) aromatic;
– the disappearance of the bands at 753 and 695 cm^{-1} assigned to the deformation vibrations of monosubstituted benzene ring.

3.5. Electrochromic properties of polymer films

Depending on the oxidation states, the electrochromic material shows different colors, and usually conjugated electrochromic polymers allow fast color changes when different potentials are applied. The applications of the electrochromic conjugated polymers are quite different due to avantages owned by these materials, because the oxidation states of the polymers are stable and 'resistant over time' [12]. It was observed that the film obtained by electropolymerization of polymer upon transparent ITO electrode surface shows different colors depending on the applied potential. For a more detailed study, in-situ UV-Vis spectroelectrochemistry was further employed, using a polymer film deposited on a transparent ITO/glass working electrode and cyclic voltammetry technique coupled with UV-Vis absorbance measurements. This procedure allowed simultaneous recording of the electronic absorption spectra in the range of 300–900 nm and the current intensity versus applied potential. The experiments were carried out in acetonitrile/toluene (1:1) solvent mixture containing TBABF$_4$ (0.1 M) as supporting electrolyte. Varying the applied potential in range of 0.0–(+1.5) V and then to 0.0 V, the film shows absorption bands in the range of 300–900 nm, which corresponds to the different oxidation states. In the neutral state of polymer (at 0 V), the film is transparent in the visible region. By increasing the applied potential value two absorption bands with maxima at 486 and 680 nm, were observed (Figure 8). The intensity of absorption bands increase simultaneously and gradually when the potential values reaches to 1.5 V. During the oxidation process, the polymer film switches its color from colorless, brown, and green to blue, respectively. During the reduction process, the intensities of absorption bands located at 486 and 680 nm, decrease and a third band at 396 nm can be observed, which is attributed to π-π* transitions due to expansion of the conjugations (Figure 8).

The potential of the working electrode have been applied to a range of positive values such as 0.0, 1.0, 1.2, 1.3 and 1.5 V for 3 minutes (Figure 9), and the polymer switches its color, like in previous case. Spectroelectrochemistry data presented above confirm the presence of the tetraphenylbenzidine (TPB) dimer, which is oxidized at about 0.65 V forming the TPB^{+} radical-cations which shows a maximum
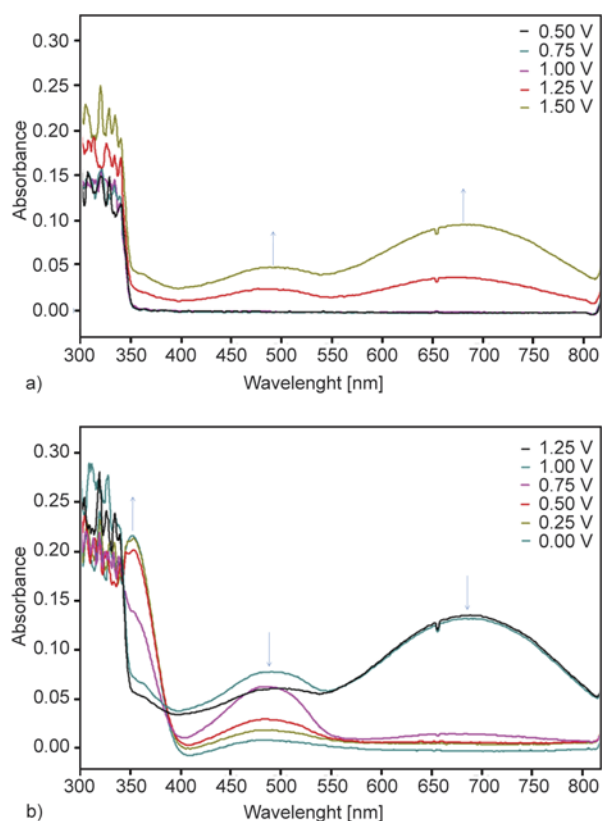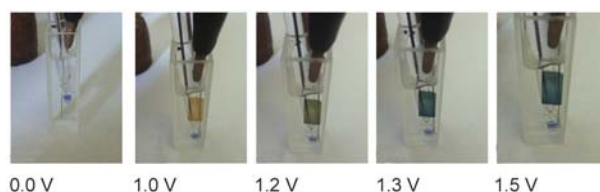
Figure 9. Evolution of the color of the polymer film from neutral to oxidized states

The color switching times were estimated by applying a potentials step and the transmittance profiles were followed. The switching time was defined as the time that was required to reach 95% of the full change in transmittance after switching potential. The ITO/P2 film oxidation state was switched by stepping the potential between 0.0 and 1.5 V, with time intervals of 15 s and the current and transmittance at 486 and 680 nm was monitored versus time. The film color changed from transparent to blue with high contrast of optical transmittance change (ΔT %) of 80% for 680 nm and only 29% for 486 nm. Moreover, the response time of the polymer film was found to be 10 s at 1.5 V from color switching and 5 s for bleaching (Figure 11). The amount of charge (Q_d) in each current curve for both processes was very similar and reveals a stable anodic electrochemical characteristic of P2 film. On the other hand, coloration efficiency (η) of the polymer film at 680 nm was also calculated to be 670 cm^2/C, using the equation $\eta = \Delta OD/Q_d = \log[T_{neut}/T_{oxi}]/Q_d$ [cm^2/C], where Q_d is the injected charge per unit electrode

Figure 8. Absorption spectra of P2 as film deposited on ITO/glass electrode, recorded during the electropolymerization process at different applied potentials: a) during the oxidation and b) during the reduction process

absorption band at 480 nm. The dication formation is observed at potentials more anodic and shows an absorption band at about 678 nm (Figure 10).
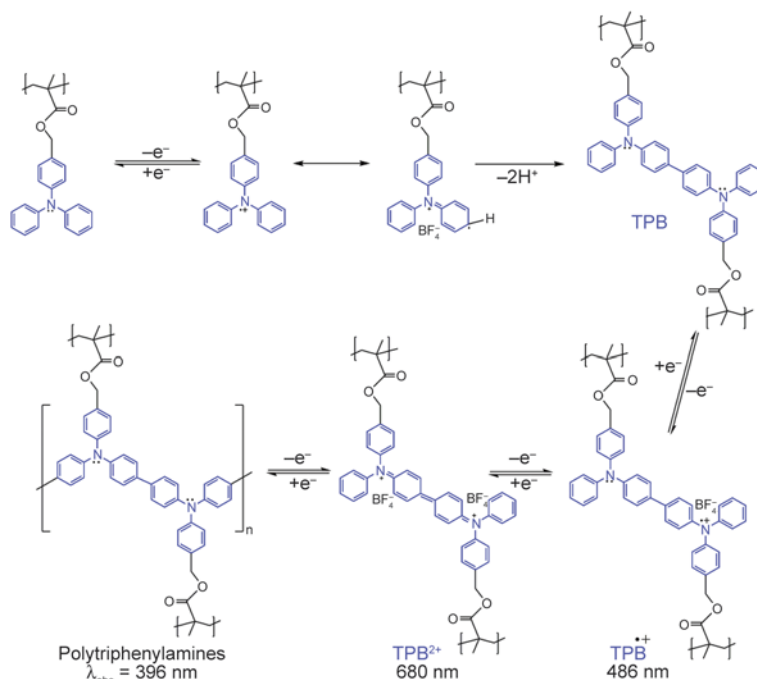
Figure 10. The proposed mechanism for the crosslinking process and the change of color with the applied potential
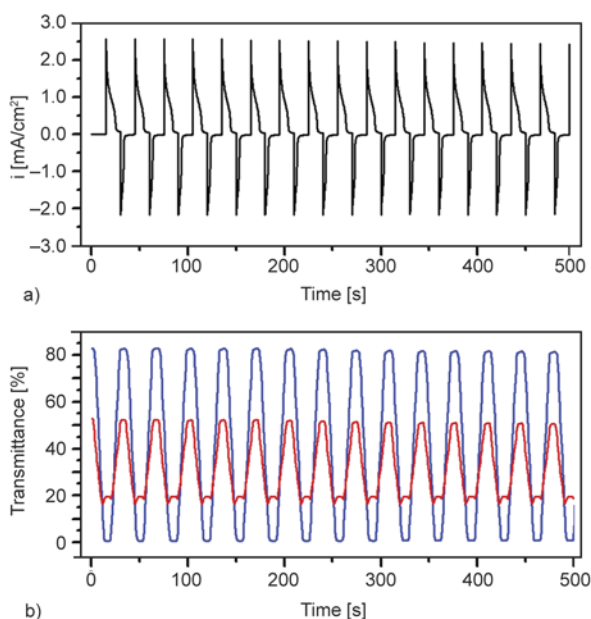
Figure 11. ITO/P2 electrochromic switching between 0 and 1.5 V (vs Ag/AgCl) applied to the electrode-posited film of P2 in CH_3CN/toluene with 0.1 M $TBABF_4$ with a cycle time of 15 s, the current (a) and optical (b) response. Absorption was recorded at 486 nm (red) and 680 nm (blue)

area during a redox step, and T_{neut} and T_{oxi} are the bleached and colored transmittance values, respectively [13].

After 17 continuous cycles the polymer film exhibited excellent stability of electrochromic characteristics. Considering these results it can be stated that the electropolymerized P2 film can be considered a promising materials for application in optoelectronic devices.

3.6. Surface morphology of polymer films

Atomic force microscopy (AFM) investigations were conducted to investigate the surface morphology of the polymer deposited on ITO/glass after electropolymerization. The micrographs recorded show that the film appears smooth and continuous over the whole image, without pinholes or defects and is characterized by morphology consisted of many crowded spheres with a mean diameter of 110 nm and root mean square (RMS) roughness of 2.75 nm (Figure 12).

4. Conclusions

Polymers based on triphenylamine with well-defined structure and characteristics, were successfully synthesized by atom transfer radical polymerization reactions. The optical properties of poly [4-(diphenylamino)benzyl methacrylate] were investigated by UV-Vis and fluorescence spectroscopy. The electrochemical properties of the synthesized polymers with triphenylamine pendant units were investigated using cyclic voltammetry technique. The synthesized polymers undergo cross-linking processes leading to a conductive film with electrochromic properties and stable color changes with coloration efficiency and high contrast of optical transmittance. The electrochemical cross-linking reaction was possible because the polymers contain in their structure triphenylamine as pendant groups with two free *para*-positions for direct coupling. The morphology of the resulting film with cross-linked structure was examined by AFM microscopy, the

Figure 12. The AFM images of film deposited by electropolymerization process (after 14 scan cycles)

film appears smooth and continuous without any pinholes or defects being formed from crowded spheres with a mean diameter of 110 nm.

Acknowledgements

References

[1] Feast W. J., Peace R. J., Sage I. C., Wood E. L.: Poly (4-vinyltriphenylamine): Synthesis and application as a hole transport layer in light-emitting diodes. Polymer Bulletin, **42**, 167–174 (1999).
DOI: 10.1007/s002890050449

[2] Park S-H., Ogino K., Sato H.: Synthesis and characterization of photorefractive polymers with triphenylamine unit and NLO chromophore unit on a side chain. Polymers for Advanced Technologies, **11**, 349–358 (2000).
DOI: 10.1002/1099-1581(200007)11:7<349::AID-PAT978>3.0.CO;2-Z

[3] Yeh K-M., Lee C-C., Chen Y.: Poly(4-vinyltriphenylamine): Optical, electrochemical properties and its new application as a host material of green phosphorescent Ir(ppy)₃ dopant. Synthetic Metals, **158**, 565–571 (2008).
DOI: 10.1016/j.synthmet.2008.04.001

[4] Iwan A., Sek D.: Polymers with triphenylamine units: Photonic and electroactive materials. Progress in Polymer Science, **36**, 1277–1325 (2011).
DOI: 10.1016/j.progpolymsci.2011.05.001

[5] Thelakkat M.: Star-shaped, dendrimeric and polymeric triarylamines as photoconductors and hole transport materials for electro-optical applications. Macromolecular Materials and Engineering, **287**, 442–461 (2002).
DOI: 10.1002/1439-2054(20020701)287:7<442::AID-MAME442>3.0.CO;2-H

[6] Thelakkat R., Hagen J., Haarer D., Schmidt H-W.: Poly(triarylamine)s- synthesis and application in electroluminescent devices and photovoltaics. Synthetic Metals, **102**, 1125–1128 (1999).
DOI: 10.1016/S0379-6779(98)01412-X

[7] Forrest S. R.: Ultrathin organic films grown by organic molecular beam deposition and related techniques. Chemical Reviews, **97**, 1793–1896 (1997).
DOI: 10.1021/cr941014o

[8] Zhan X., Zhu D.: Conjugated polymers for high-efficiency organic photovoltaics. Polymer Chemistry, **1**, 409–419 (2010).
DOI: 10.1039/B9PY00325H

[9] Cheng Y-J., Yang S-H., Hsu C-S.: Synthesis of conjugated polymers for organic solar cell applications. Chemical Reviews, **109**, 5868–5923 (2009).
DOI: 10.1021/cr900182s

[10] Yen H-J., Liou G-S.: Solution-processable triarylamine-based electroactive high performance polymers for anodically electrochromic applications. Polymer Chemistry, **3**, 255–264 (2012).
DOI: 10.1039/C1PY00346A

[11] Yen H-J., Liou G-S.: Solution-processable novel near-infrared electrochromic aromatic polyamides based on electroactive tetraphenyl-*p*-phenylenediamine moieties. Chemistry of Materials, **21**, 4062–4070 (2009).
DOI: 10.1021/cm9015222

[12] Mortimer R. J., Dyer A. L., Reynolds J. R.: Electrochromic organic and polymeric materials for display applications. Displays, **27**, 2–18 (2006).
DOI: 10.1016/j.displa.2005.03.003

[13] Monk P. M. S., Moritimer R. J., Rosseinsky D. R.: Electrochromism: Fundamentals and applications. VCH, Weinheim (1995).

[14] Lin H-Y., Liou G-S.: Poly(triphenylamine)s derived from oxidative coupling reaction: Substituent effects on the polymerization, electrochemical, and electro-optical properties. Journal of Polymer Science Part A: Polymer Chemistry, **47**, 285–294 (2009).
DOI: 10.1002/pola.23155

[15] Grazulevicius J. V., Strohriegl P., Pielichowski J., Pielichowski K.: Carbazole-containing polymers: Synthesis, properties and applications. Progress in Polymer Science, **28**, 1297–1353 (2003).
DOI: 10.1016/S0079-6700(03)00036-4

[16] Mori H., Ookuma H., Endo T.: Poly(*N*-vinylcarbazole) star polymers and amphiphilic star block copolymers by xanthate-mediated controlled radical polymerization. Macromolecules, **41**, 6925–6934 (2008).
DOI: 10.1021/ma801266h

[17] Keddie D. J., Guerrero-Sanchez C., Moad G.: The reactivity of *N*-vinylcarbazole in RAFT polymerization: Trithiocarbonates deliver optimal control for the synthesis of homopolymers and block copolymers. Polymer Chemistry, **4**, 3591–3601 (2013).
DOI: 10.1039/C3PY00487B

[18] Mori H., Ookuma H., Nakano S., Endo T.: Xanthate-mediated controlled radical polymerization of *N*-vinylcarbazole. Macromolecular Chemistry and Physics, **207**, 1005–1017 (2006).
DOI: 10.1002/macp.200600070

[19] Grigoras M., Negru O. I.: Synthesis of star poly(*N*-vinylcarbazole) by microwave-assisted reversible addition-fragmentation chain transfer polymerization (RAFT). Polymers, **4**, 1183–1194 (2012).
DOI: 10.3390/polym4021183

[20] Nakabayashi K., Mori H.: Novel complex polymers with carbazole functionality by controlled radical polymerization. International Journal of Polymer Science, **2012**, 170912/1–170912/18 (2012).
DOI: 10.1155/2012/170912

[21] Nakabayashi K., Mori H.: Recent progress in controlled radical polymerization of *N*-vinyl monomers. European Polymer Journal, **49**, 2808–2838 (2013).
DOI: 10.1016/j.eurpolymj.2013.07.006

[22] Baethge H., Butz S., Schmidt-Naake G.: 'Living' free radical copolymerization of styrene and N-vinylcarbazole. Macromolecular Rapid Communications, **18**, 911–916 (1997)
DOI: 10.1002/marc.1997.030181003

[23] Hua J., Chen D., Yu Y., Xu L., Zhang Y., Jing X., Wu A., Shi L.: Preparation of C60 bonded poly(N-vinylcarbazole) with C60Cln/CuCl/Bpy catalyst system. Polymer Bulletin, **48**, 135–141 (2002).
DOI: 10.1007/s00289-002-0023-1

[24] Hua J., Chen D., Jing X., Xu L., Yu Y., Zhang Y.: Preparation and photoconducting property of $C_{60}C_{ln-m}$-bonded poly(N-vinylcarbazole) with $C_{60}Cl_n$/CuCl/Bpy catalyst system. Journal of Applied Polymer Science, **87**, 606–609 (2003).
DOI: 10.1002/app.11320

[25] Behl M., Hattemer E., Brehmer M., Zentel R.: Tailored semiconducting polymers: Living radical Polymerization and NLO-functionalization of triphenylamines. Macromolecular Chemistry and Physics, **203**, 503–510 (2002).
DOI: 10.1002/1521-3935(20020201)203:3<503::AID-MACP503>3.0.CO;2-P

[26] Lindner S. M., Thelakkat M.: Fluorescent dye-labeled polymers carrying triphenylamine, styrene, or acrylate pendant groups. Macromolecular Chemistry and Physics, **207**, 2084–2092 (2006).
DOI: 10.1002/macp.200600385

[27] Lindner S. M., Kaufmann N., Thelakkat M.: Nanostructured semiconductor block copolymers: π–π stacking, optical and electrochemical properties. Organic Electronics, **8**, 69–75 (2007).
DOI: 10.1016/j.orgel.2006.11.002

[28] Schroot R., Friebe C., Altuntas E., Crotty S., Jäger M., Schubert U. S.: Nitroxide-mediated polymerization of styrenic triarylamines and chain-end functionalization with a ruthenium complex: Toward tailored photoredox-active architectures. Macromolecules, **46**, 2039–2048 (2013).
DOI: 10.1021/ma302631f

[29] Häussler M., Phei Lok Y., Chen M., Jasieniak J., Adhikari R., King S. P., Haque S. A., Forsyth C. M., Winzenberg K., Watkins S. E., Rizzardo E., Wilson G. J.: Benzothiadiazole-containing pendant polymers prepared by RAFT and their electro-optical properties. Macromolecules, **43**, 7101–7110 (2010).
DOI: 10.1021/ma1008572

[30] Williams P. E., Moughton A. O., Patterson J. P., Khodabakhsh S., O'Reilly R. K.: Exploring RAFT polymerization for the synthesis of bipolar diblock copolymers and their supramolecular self-assembly. Polymer Chemistry, **2**, 720–729 (2011).
DOI: 10.1039/C0PY00359J

[31] zur Borg L., Domanski A. L., Breivogel A., Bürger M., Berger R., Heinze K., Zentel R.: Light-induced charge separation in a donor–chromophore–acceptor nanocomposite poly[TPA-Ru(tpy)$_2$]@ZnO. Journal of Materials Chemistry C, **1**, 1223–1230 (2013).
DOI: 10.1039/C2TC00535B

[32] zur Borg L., Lee D., Lim J., Bae W. K., Park M., Lee S., Lee C., Char K., Zentel R.: The effect of band gap alignment on the hole transport from semiconducting block copolymers to quantum dots. Journal of Materials Chemistry C, **1**, 1722–1726 (2013).
DOI: 10.1039/C3TC00837A

[33] Tew G. N., Pralle M. U., Stupp S. I.: Supramolecular materials with electroactive chemical functions. Angewandte Chemie International Edition, **39**, 517–521 (2000).
DOI: 10.1002/(SICI)1521-3773(20000204)39:3<517::AID-ANIE517>3.0.CO;2-#

[34] Natori I., Natori S., Usui H., Sato H.: Anionic polymerization of 4-diphenylaminostyrene: Characteristics of the alkyllithium/*N,N,N′,N′*-tetramethylethylenediamine system for living anionic polymerization. Macromolecules, **41**, 3852–3858 (2008).
DOI: 10.1021/ma800222z

[35] Natori I., Natori S., Sekikawa H., Ogino K.: Synthesis of C$_{60}$ end-capped poly(4-diphenylaminostyrene): Addition of poly(4-diphenylaminostyryl)lithium to C$_{60}$. Reactive and Functional Polymers, **69**, 613–618 (2009).
DOI: 10.1016/j.reactfunctpolym.2009.04.003

[36] Higashihara T., Ueda M.: Living anionic polymerization of 4-vinyltriphenylamine for synthesis of novel block copolymers containing low-polydisperse poly(4-vinyltriphenylamine) and regioregular poly(3-hexylthiophene) segments. Macromolecules, **42**, 8794–8800 (2009).
DOI: 10.1021/ma901636a

[37] Natori I., Natori S., Sekikawa H., Takahashi T., Ogino K., Tsuchiya K., Sato H.: Poly(4-diphenylaminostyrene) with a well-defined polymer chain structure: Controllable optical and electrical properties. Polymer, **51**, 1501–1506 (2010).
DOI: 10.1016/j.polymer.2010.01.054

[38] Natori I., Natori S., Sekikawa H., Takahashi T., Sato H.: Bipolar polymer semiconductor blends of C$_{60}$-end-capped poly(4-diphenylaminostyrene) and poly(4-diphenylaminostyrene): One-pot synthesis and charge-transport properties. Journal of Applied Polymer Science, **121**, 3433–3438 (2011).
DOI: 10.1002/app.33864

[39] Natori I., Natori S., Sekikawa H., Tsuchiya K., Ogino K.: Synthesis of poly(*p*-phenylene)-poly(4-diphenylaminostyrene) bipolar block copolymers with a well-controlled and defined polymer chain structure. Journal of Polymer Science Part A: Polymer Chemistry, **49**, 1655–1663 (2011).
DOI: 10.1002/pola.24590

[40] Natori I., Natori S., Tsuchiya K., Ogino K.: Synthesis of novel semiconducting polymers consisting of *p*-phenylene, *p*-phenylenevinylene, and styrylamine structures: Copolymerization and dehydrogenation of 1,3-cyclohexadiene and 4-diphenylaminostyrene. Macromolecules, **44**, 256–262 (2011).
DOI: 10.1021/ma102183f

[41] Hsu J-C., Chen Y., Kakuchi T., Chen W-C.: Synthesis of linear and star-shaped poly[4-(diphenylamino)benzyl methacrylate]s by group transfer polymerization and their electrical memory device applications. Macromolecules, **44**, 5168–5177 (2011).
DOI: 10.1021/ma2006377

[42] Negru O. I., Grigoras M.: Grafted polytriphenylamines synthesized by atom transfer radical polymerization in tandem with oxidative polycondensation. Iranian Polymer Journal, **22**, 641–651 (2013).
DOI: 10.1007/s13726-013-0163-1

[43] Negru O. I., Grigoras M.: Polytriphenylamines synthesized by interfacial and microemulsion oxidative polymerization. Colloid and Polymer Science, **292**, 143–151 (2014).
DOI: 10.1007/s00396-013-3055-1

[44] Stolka M., Pai D. M., Renfer D. S., Yanus J. F.: Photoconductivity and hole transport in polymers of aromatic amine-containing methacrylates. Journal of Polymer Science: Polymer Chemistry Edition, **21**, 969–983 (1983).
DOI: 10.1002/pol.1983.170210406

[45] Seo E. T., Nelson R. F., Fritsch J. M., Marcoux L. S., Leedy D. W., Adams R. N.: Anodic oxidation pathways of aromatic amines. Electrochemical and electron paramagnetic resonance studies. Journal of the American Chemical Society, **88**, 3498–3503 (1966).
DOI: 10.1021/ja00967a006

[46] Petr A., Kvarström C., Dunsch L., Ivaska A.: Electrochemical synthesis of electroactive polytriphenylamine. Synthetic Metals, **108**, 245–247 (2000).
DOI: 10.1016/S0379-6779(99)00137-X

[47] Chiu K. Y., Su T. X., Li J. H., Lin T-H., Liou G-S., Cheng S-H.: Novel trends of electrochemical oxidation of amino-substituted triphenylamine derivatives. Journal of Electroanalytical Chemistry, **575**, 95–101 (2005).
DOI: 10.1016/j.jelechem.2004.09.005

[48] Oyama M., Nozaki K., Okazaki S.: Pulse-electrolysis stopped-flow method for the electrospectroscopic analysis of short-lived intermediates generated in the electrooxidation of triphenylamine. Analytical Chemistry, **63**, 1387–1392 (1991).
DOI: 10.1021/ac00014a010

Exploring nanocrystalline cellulose as a green alternative of carbon black in natural rubber/butadiene rubber/styrene-butadiene rubber blends

W. J. Chen, J. Gu[*]*, S. H. Xu*

College of Materials Science and Engineering, South China University of Technology, 510640 Guangzhou, China

Abstract. A series of nanocrystalline cellulose (NCC) reinforced natural rubber/butadiene rubber/styrene-butadiene rubber (NR/BR/SBR) blends were prepared via mastication of NR/NCC, BR/SBR and other ingredients. Resorcinol and hexamethylene tetramine (RH) was adopted to modify the interface between NCC and rubber matrix. The morphology, dynamic viscoelastic behavior, apparent crosslink density, mechanical performance and dynamic mechanical property of NR/BR/SBR/NCC blends were discussed in detail. The results showed that NCC was uniformly dispersed in composites and RH could enhance the adhesion of NCC and matrix. According to the dynamic mechanical analysis, NCC performed comparable reinforcing effect with carbon black (CB), and the modulus was improved with modification of RH. Mechanical tests showed that the replacement of CB by NCC in the blends did not deteriorate mechanical properties of composites. Besides, the blends exhibited best mechanical properties, when 10 phr NCC substituted CB.

Keywords: nanocomposites, nanocrystalline cellulose, NR/BR/SBR, reinforcements

1. Introduction

Carbon black is one of the most commonly used reinforcing fillers in rubber for its excellent reinforcement in combination with low cost. However, in the mixing process, CB has such defect as environmental pollution, energy consumption and time consumption. Additionally, CB is charged with consuming the depleting petroleum resources for its manufacture and more or less contributes to the accumulation of greenhouse gases. Considering the limited resource and the environmental burden, it is a meaningful topic to reduce the petroleum dependency of industrial products. Thus, many researchers tend to investigate various kinds of bio-based renewable materials as the alternatives of CB in rubber.

Cellulose, one of the most abundant biorenewable materials, has its advantages as a reinforcing filler in rubber: low cost, low density, low energy consumption; high specific strength and modulus; easy processability, reactive surface, easy recycling and degradable property [1, 2]. Actually, not few lectures have reported the application of cellulose in rubber. Since Favier and co-workers [3] firstly reinforced rubber latex with nano-scale cellulose, lots of researches have managed to extract cellulose from nature, namely, rattan [4], bagasse [5], cassava [6], kenaf [7], sisal [8], oil palm [9] etc., and to apply as the reinforcing agent in rubber. Results show that cellulose reinforces the rubber latex effectively. Besides, cellulose could bring additional benefits when serving as the filler in rubber, such as relatively easy-degradable property of rubber composites [10], reduced Payne effect of filler [11], improved abrasion resistance [12] and so on. Therefore, cellulose is the promising reinforcing filler of rubbers.

[*]Corresponding author, e-mail: psjgu@scut.edu.cn

The influences of fillers' properties on rubber composites mainly depend on the size, shape and surface properties; among them, the size distribution is the most important factor [13]. The smaller the size, the better the reinforcing effect. And the surface properties determine the compatibility and interaction of filler-rubber. Besides, the dispersion of fillers is also the premise of excellent reinforcing effect. It was reported that nanoscale cellulose could reinforce not only polar rubber latex [14, 15] but also apolar rubber latex [6]. For apolar matrix, modification of cellulose/matrix interaction would do a great favor to the properties [9, 16]. There were also literatures making comparisons of reinforcing effect between cellulose and commercial fillers, most of which showed negative results after replacing commercial fillers by cellulose, due to the difference of polarity and bad interaction [4, 12, 17].

The development of various rubber products and the requirement of elastomer with special behaviors motivate the development of rubber blends. Compounding two or more kinds of rubber with certain ratios usually contributes to the integration of behaviors, in spite of synergistic effect in some aspects. Until now, a great part of elastomer products consist of rubber blends, such as tyres, conveyors, tubes and so on. While, it is relatively uncommon in the literatures to study the rubber blends reinforced by cellulose.

In this paper, the masterbatch technique was adopted to fill NR/BR/SBR with NCC, which might be also acceptable for other rubber blends. The coagulation method was the approach used to get NR/NCC masterbatches, which was clean and simple to carry out and could ensure good dispersion of NCC in rubber. Then, the resulting masterbatches were used to mixing and reinforcing BR and SBR. In order to improve the interaction between rubber and cellulose, resorcinol and RH was added to modify the NCC/matrix interface, which was widely used as an coupling agent to improve the rubber-filler interaction [9, 18, 19]. Lastly, the structure, morphology and performance of NCC loaded NR/BR/SBR blends were investigated by scanning electron microscopy (SEM), rubber process analysis (RPA), apparent crosslink density, dynamic mechanical analysis (DMA) and mechanical properties tests.

2. Experimental
2.1. Materials
Microcrystalline cellulose (MCC, industrial grade) was provided by the Gaoli Chemical Company in Guangzhou, China. The sulfuric acid (95~98 wt%) of analytical grade was the product of Chemical R&D Center in Guangdong province, China. To get the NCC, sulfuric acid with a concentration of 64 wt% had been prepared and used to hydrolyze microcrystalline cellulose for 30 min at 45°C. After the acid hydrolysis process, NCC solution was washed repeatedly by distilled water until pH reached 6~8, via centrifugation.

Natural rubber latex (61 wt%) was purchased from Eleventh Rubber Factory of Guangzhou, China. Anhydrous calcium chloride (analytical grade) was produced by Tianjin Fuchen Chemical Company, China. BR9000 and SBR1500 were supplied by Guangzhou Rubber Industrial Product Research Institute Co., Ltd. N330 grade carbon black (nitrogen absorption surface area 78 m^2/g) was obtained from China Rubber Company (produced in Anshan). RH was the product of Guoli Chemical Industry and Technology in China. The molecule structure of RH was showed in Figure 1. Other rubber compounding ingredients were all of industrial grade.
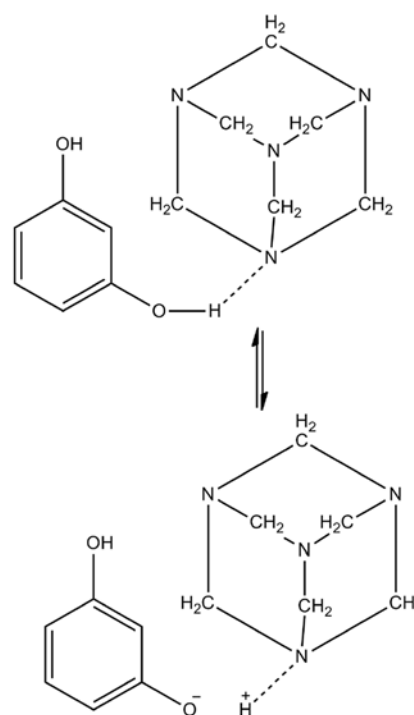

Figure 1. Molecular structure of RH

2.2. Preparation of NR/BR/SBR/NCC composites

With certain NR/NCC ratios (60/0, 60/5, 60/10, 60/15, 60/20), NCC suspension and NR latex were mixed by intense mechanical stirring in order to get a homogeneous mixture, followed by the coagulation step with the help of $CaCl_2$ solution. Then, the coagulated NR/NCC compound was washed with clean water for enough time to remove impurity. After that, the obtained NCC/NR materbatch was dried in a ventilated oven at 70°C until constant weight.

NCC and CB loaded rubber compounds were prepared in a two-roll mill (according to ASTM D3182-07), based on the formulation in Table 1. Mastication process of NCC/NR masterbatch, BR and SBR had to be continued about 3 minutes. Then certain amount of CB fillers (45, 40, 35, 30, 25 phr) were added to reach the total fillers volume of 45 phr, along with other ingredients, including the modifier RH. The nip-gap, mill roll, speed ratio and the number of passes were kept the same for all samples. The milling step was concluded by passing the compounds four times through the mill at a setting of 6 mm, taking care to maintain the direction of compounds and to ensure the orientation along the flow direction to some degree. The last step was followed by vulcanization, which was carried out at 150°C for a corresponding cure time (T_{90}) with a hot press, to obtain composite sheets with a 1 mm thickness. Additionally, the other ingredients of composites were fixed as: zinc oxide 5 phr, stearic acid 2 phr, CZ 1.5 phr, accelerator DM 0.5 phr, anti-aging agent 4010NA 1.5 phr, sulfur 1.5 phr.

Table 1. Compounding formulation [phr]

Sample codes	NR/NCC	BR	SBR	CB (N330)	RH
0/45/0	60/0	20	20	45	0
0/45/4					4
5/40/0	60/5	20	20	40	0
5/40/4					4
10/35/0	60/10	20	20	35	0
10/35/4					4
15/30/0	60/15	20	20	30	0
15/30/4					4
20/25/0	60/20	20	20	25	0
20/25/4					4

2.3. Characterization

Micrographs of NCC and vulcanizates were obtained with a field emission scanning electron microscope (Nova NanoSEM 430, FEI Company, Netherlands). A copper grid was used to salvage NCC from diluted NCC suspension. Then the NCC and fractured surfaces of various composites were sputter-coated with gold prior to taking pictures.

X-ray diffraction (XRD) tests were carried out using an X'Pert Pro MRD (PANalytical B. V.). The diffraction patterns were recorded using Cu-Kα radiation at 40 kV. Crystallinity was calculated by the following Equation (1) [20]:

$$Crystallinity = 1 - \frac{I_{am}}{I_{002}} \qquad (1)$$

where I_{002} is the maximum intensity of the peak at 2θ around 23° and I_{am} is the minimum intensity of the peak at 2θ around 18°.

Microstructure analysis of MCC and NCC was conducted by Fourier transform infrared spectroscopy (Migna 760, the Nicolet Company), after mixing it with spectroscopy grade potassium bromide (KBr) powder.

The experiments of strain sweeps were carried out by RPA2000 (Alpha technologies, US), under the following test configuration: preheat the samples at 60°C inside the cavity for 2 min with 0.1% strain and 1 Hz frequency, so as to get a stable temperature and release built-in stress of samples; then strain sweeping was done between 0.2 to 150% strain at 60°C and a frequency of 1 Hz.

Prediction of cured samples' apparent crosslink density (V_r) was done according to equilibrium swelling experiments, as reported in [21].

Dumbbell specimens (6 mm width in cross-section, 1 mm thickness) and un-nicked 90° angle test pieces (1 mm thickness) were prepared for the stress-strain (ASTM D412) and tear strength (ASTM D624) test respectively, via tensile strength tester (UT-2060, UCAN Dynatex Inc., Taiwan) with a crosshead speed of 500 mm/min. Shore A hardness was determined under the conditions given in ASTM-D2240. The dynamic mechanical behaviors of composites were measured by a dynamic mechanical analyzer (DMA242C NETZSCH; Germany) in tension mode (static force 0.5 N, dynamic force 5.0 N, force factor 1.1, amplitude 80.0 μm,). Samples were prepared with a size of 8 mm length, 1 mm thickness and 6 mm width. The scan temperature was run from –100 to 100°C with a heating ramp of 3 °C/min and a frequency of 10 Hz.

3. Results and discussion

3.1. Characterization of cellulose

NCC, prepared by acid hydrolysis of MCC, was analyzed via SEM as shown in Figure 2. The SEM image revealed the existence of isolated rod-like cellulose with diameters ranging from 20 to 140 nm and lengths below 2 μm. This rod-like nano-cellulose would become potentially excellent reinforcing filler [13].

According to the XRD pattern displayed in Figure 3, MCC and NCC had similar XRD curves. Both MCC and NCC had peaks at 2θ angles 15, 16.7, 22.9, 34.7°, which was attributed to the reflections from 11′0 and 110, 020 and 004 lattice planes, respectively; and the 2θ angles 15, 16.7, 22.9 implied a crystalline structure of cellulose I [10, 22]. Besides, the crystallinity of MCC and NCC were calculated to be 87.12 and 87.96%, respectively, which were almost the same. Thus, the acid hydrolysis hardly
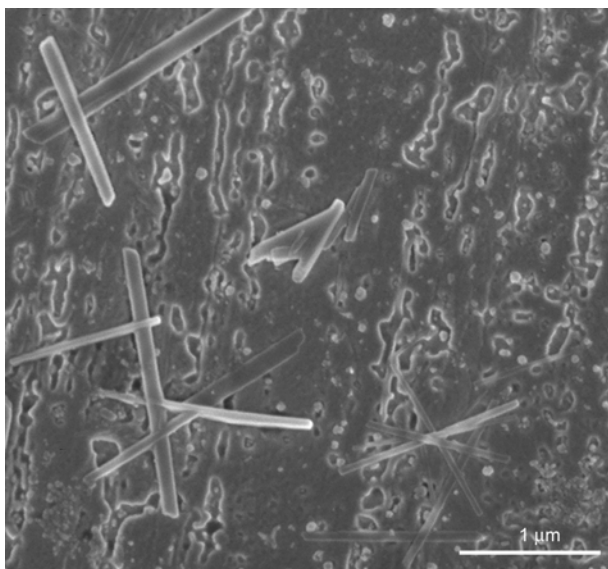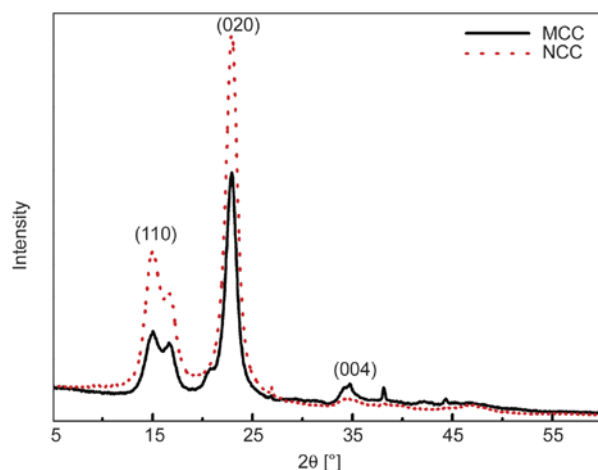

Figure 2. SEM image of NCC

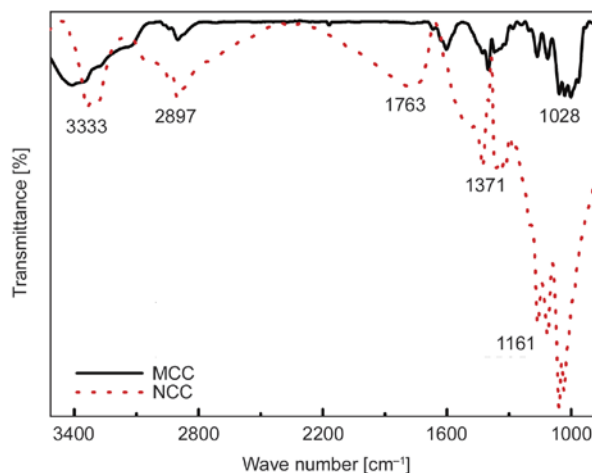**Figure 3.** XRD spectrum of MCC and NCC

Figure 4. FTIR spectrum of MCC and NCC

reduced crystallinity. A slightly difference maybe the shapes of peaks at 38.1 and 44.3°: all the peaks of NCC above 25° tended to extensively broaden and were not easy to figure out. The explanation was that the acid hydrolysis mainly took place at amorphous regions and imperfect crystalline regions. Hence, the peaks of NCC at large-angle tended to fade away and those at small-angle, however, were sharpened. The retention of crystalline area could retain the mechanical property of cellulose, which led to a good reinforcing effect.

Fourier transform infrared (FTIR) spectrum of MCC powder and NCC suspension was exhibited in Figure 4. The broad peak from 3400 to 3300 cm^{-1} indicated OH groups in cellulose. Transmittance at 2897 cm^{-1} belonged to alkyl CH stretches. Absorption peak at 1317, 1338, 1371 cm^{-1} corresponded to CH_2 rocking vibrations, OH bending vibrations and CH bending vibrations, respectively. The peak at 1429 cm^{-1} belonged to CH_2 bending. And 1161, 1112, 1057, 1031 cm^{-1} were characteristics of cellulose I′ C–O–C–O–C bond [23]. According to the mentioned peaks, the acid hydrolysis process did not cause chemical changes in cellulose. However, there was a new peak at 1760 cm^{-1} of NCC, which probably denoted the carbonyl group of lactones at the chain end. Explanation maybe that the degradation of cellulose increased chain ends, thus resulting in the appearance of C=O peak.

3.2. Morphology analysis of NR/BR/SBR composites

The tensile fracture surfaces of rubber composites filled with various NCC/CB/RH ratios were displayed in Figure 5. The fillers, both NCC and CB,
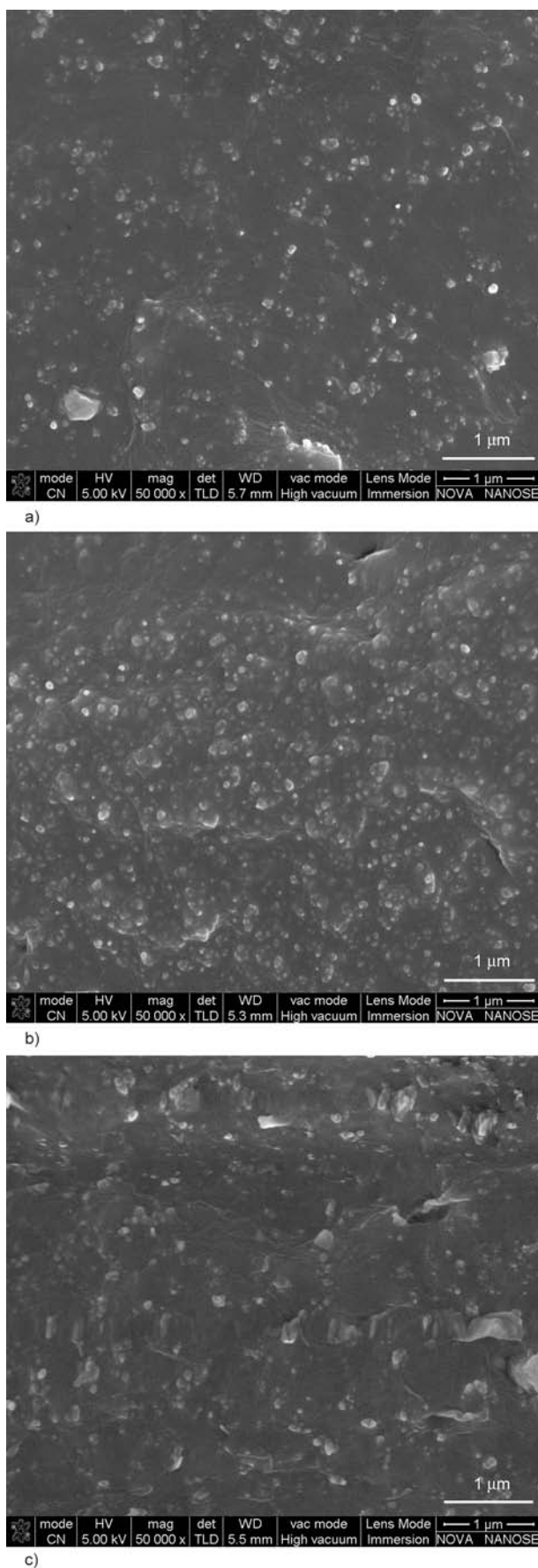
Figure 5. SEM images of NR/BR/SBR composites reinforced by NCC and CB: (a) NCC/CB/RH 0/45/0; (b) NCC/CB/RH 10/35/0; (c) NCC/CB/RH 10/35/4

in the rubber matrix could easily be identified as white dots. The micrographs of various vulcanizates revealed a relatively uniform morphology of the surface and displayed a slightly rolling section, which indicated good distribution of fillers and ductile fracture of composites, respectively. Besides, it's hard to find rod-like filler in NCC-loaded composites (Figure 5b and 5c), suggesting NCC oriented in the stretching direction. Because the orientation effect might be caused while the tensile fracture surfaces were prepared. It showed that the white dots in Figure 5b were relatively more and bigger than those in Figure 5a. Because the adhesion between NCC and matrix was poor, the fracture tended to happen along the interface of NCC/rubber, hence more exposure of NCC. Incorporation of RH helped to improve compatibility and adhesion, so boundary of NCC and matrix in Figure 5c tended to be obscure. That microstructure of composites would affect the mechanical properties, discussed in last parts.

In order to study the distribution of NCC in rubber, composites with only NCC filler were prepared and showed in Figure 6. The images illustrated the fracture surfaces of RH modified composite (Figure 6b) and without RH modification (Figure 6a). Several holes were observed in unmodified composite (Figure 6a), since some of the NCC was pulled out from the matrix. However, the surfaces of modified ones were smoother: most of the NCC was totally embedded in matrix, only showing up as dots. This indicated a strong interaction between NCC and rubber matrix, due to the modification of RH.

3.3. RPA 2000 analysis of NR/BR/SBR compounds

RPA was carried out to identify the network condition of uncured compounds, displayed in Figure 7. The total modulus reflecting both stable and unstable (major part) network could described by storage modulus (G') in small strain [24]. The unstable network commonly indicated the filler network and showed as the Payne effect [25]. Figure 7 illustrated that G' decreased as NCC partly displaced CB. This was because CB could form bound rubber [26], thus performing high modulus. Nevertheless, NCC networks were relatively weaker than those of CB. The substitution of CB by NCC diluted the CB network [27] and facilitated good dispersion of fillers. However, an unusual phenomenon was that the very low amount (4 phr) of RH involved in the compound led
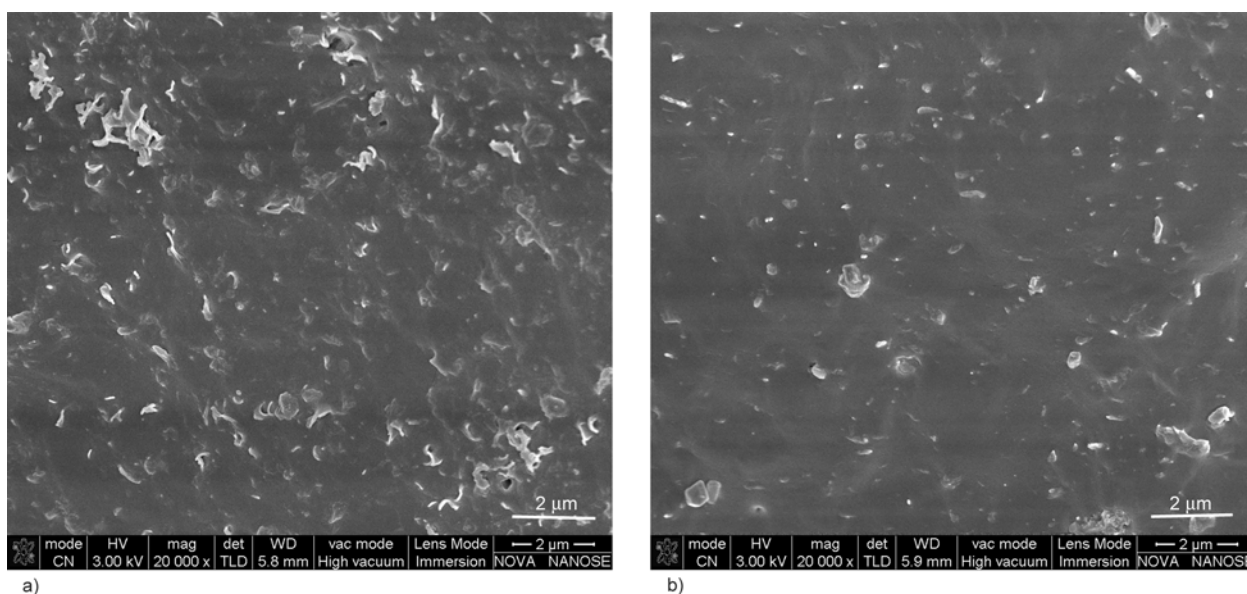
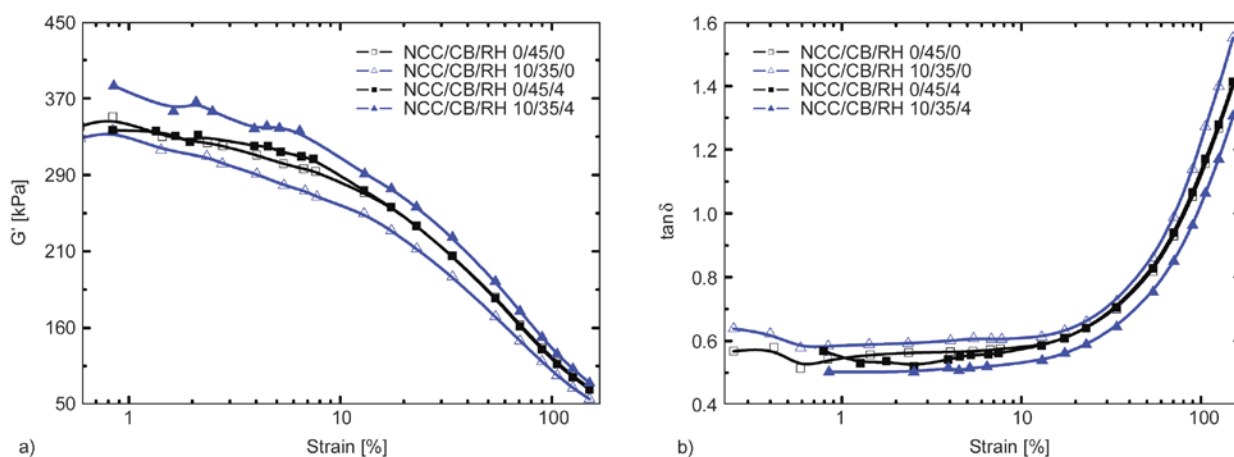**Figure 6.** SEM images of NR/BR/SBR composites filled with NCC: (a) NCC/CB/RH 10/0/0; (b) NCC/CB/RH 10/0/4

Figure 7. G'–strain (a) and $\tan\delta$–strain (b) curves of uncured NR/BR/SBR compounds

to an obvious rise in the modulus. It's worth noting that RH has not developed chemical link with rubber in the uncured compounds. So this rise was mainly attributed to the physical interaction of RH with filler. The hydrogen bond of RH/NCC has been verified in our previous publications [28]. It could be deduced that, with the existence of RH, NCC network seemed to be enhanced by hydrogen bond via RH. The fact that the addition of RH hardly affected the modulus of control samples (compounds without NCC) further proved it: this part of increase only resulted from the interaction of NCC/RH.

The loss tangent ($\tan\delta$) is the ratio of dissipated energies and storage energies in every cyclic strain. According to Wang [29], the breakdown and reformation of the network would result in an additional energy dissipation during cyclic strain, which was

evaluated by hysteresis ($\tan\delta$). Figure 7 showed a rise in $\tan\delta$ as NCC partly replace CB, for polar and rod-like NCC caused more friction than CB among macromolecules. However, the $\tan\delta$ was lower than in the control sample for RH modified compounds, since hydrogen bond enhanced the NCC network.

3.4. Apparent crosslink densities of NR/BR/SBR composites

Apparent crosslink densities of rubber/NCC/CB composites were displayed in Figure 8. It showed that, without the modification of RH, the substitution of NCC for CB led to a gradual decline in V_r, especially when fillers ratios reached 20/25. The abundant hydroxyl group in NCC could interact with curing agents, resulting in the decline of V_r [30]. After modified by RH, composites showed markedly improved but irregularly varying V_r as a function of
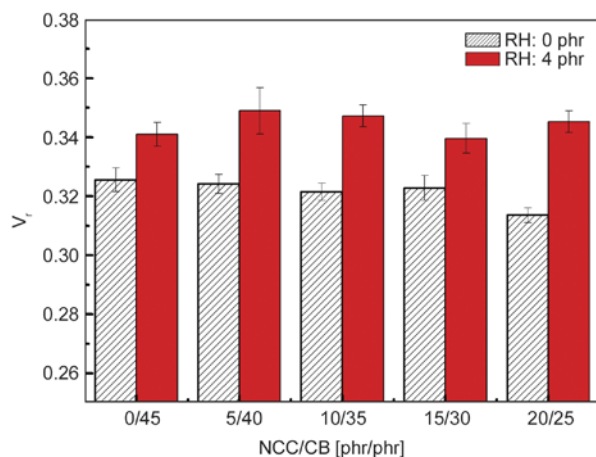
Figure 8. Apparent crosslink densities of NR/BR/SBR composites reinforced by NCC and CB
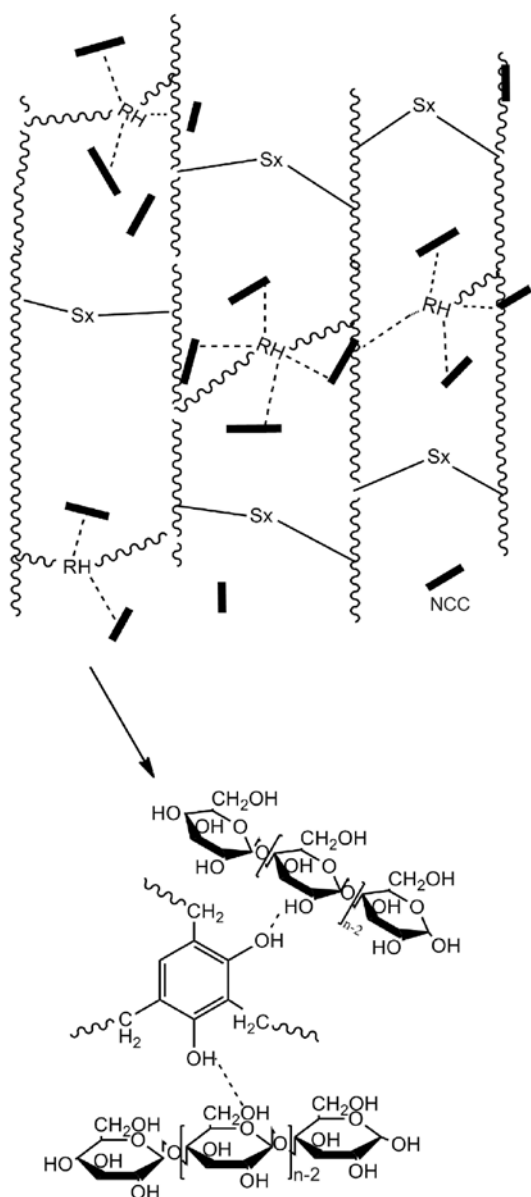

Figure 9. Interaction between NCC and macromolecules in modified composites [32]

fillers ratios. It was because at the cure temperature, RH would decompose into phenols, methyl and amine, which reacted *in situ* with the macromolecules to form resorcinol-formaldehyde resin [31]. Through it, active sites to polar fillers were introduced in the low-polarity rubber molecules as shown in Figure 9 [32]. Besides, amine generally facilitated the curing process [33, 34]. Therefore, the apparent crosslink densities were improved by RH. On the other hand, the existence of RH also influenced the NCC network as reflected in the RPA data, hence elevating V_r and preserving V_r as fillers ratio changed.

3.5. Dynamic mechanical performance of NR/BR/SBR composites

DMA was conducted to explore the dynamic response of CB and NCC loaded composites. The curves of storage modulus (E') and $\tan\delta$ and corresponding characteristics were shown in Figure 10 and Table 2, respectively. There were obvious reductions of E' at the temperature ranging from –80 to –45°C, followed by a rubbery plateau. And the $\tan\delta$ reached the top peak at about –55°C, illustrating the glass transition (T_g) of composites. Comparison of different samples showed that the replacement of CB by NCC did not impair the reinforcing effect, which was reflected by the slightly increased
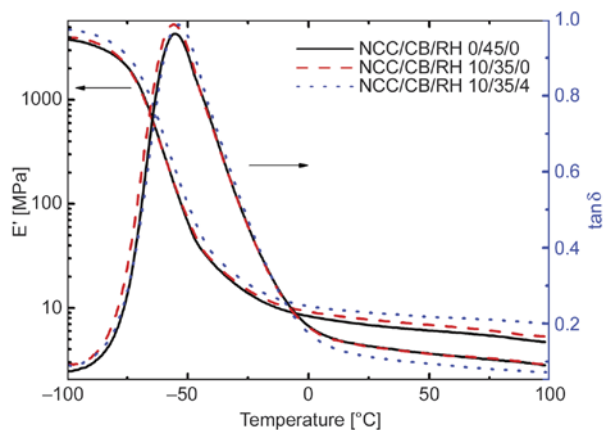

Figure 10. E'–T and $\tan\delta$–T curves of NR/BR/SBR composites reinforced by NCC and CB

Table 2. Data of the E' and $\tan\delta$–T curves of NCC-loaded NR/BR/SBR composites

NCC/CB/RH	T_g [°C]	$E'_{(25°C)}$ [MPa]	$\tan\delta_{(0°C)}$	$\tan\delta_{(60°C)}$
0/45/0	–55.2	6.867	0.1942	0.1151
10/35/0	–55.8	7.751	0.1906	0.1144
10/35/4	–53.9	9.023	0.1761	0.0887

value of *E′*. And modification of RH further facilitated this tendency. The reinforcement of NCC was due to the high aspect ratio and modulus [35]. So, a certain amount of NCC could perform comparable reinforcing effect with CB. Additionally, RH enhanced the NCC network by hydrogen bonding and linked this network to rubber molecules, as shown in the previous part. Besides, the contribution of RH to rubber crosslink also played a role.

The loss tangent (tan δ) is the ratio of dissipated energies and storage energies. It is the value to characterize internal friction. The higher the tan δ, the more friction the internal system suffers and the more heat is produced in the system. According to the characteristics of tan δ, tan δ at the temperature above 0°C decreased slightly upon the replacement of CB by NCC. The existence of RH also decreased the tan δ, because RH facilitated the crosslinking of

rubber. This trend suggested a low rolling resistance and probably reduced heat built-up.

3.6. Mechanical properties of NR/BR/SBR composites

The mechanical properties of NCC and CB loaded composites were exhibited in Figure 11. It showed that the substitution of CB by NCC did not cause obvious deterioration of the mechanical properties. And the elongation at break was even improved from 400 to 500%, after 20 phr NCC replacing CB. These comparable performances of NCC loaded composites with CB-filled ones were possibly due to the nano-effect [13] of cellulose and good dispersion of fillers, supported by SEM images. If need to mention some defects, it were permanent set and modulus at 300% that were undermined. This tendency was a result of weak adhesion of polar NCC
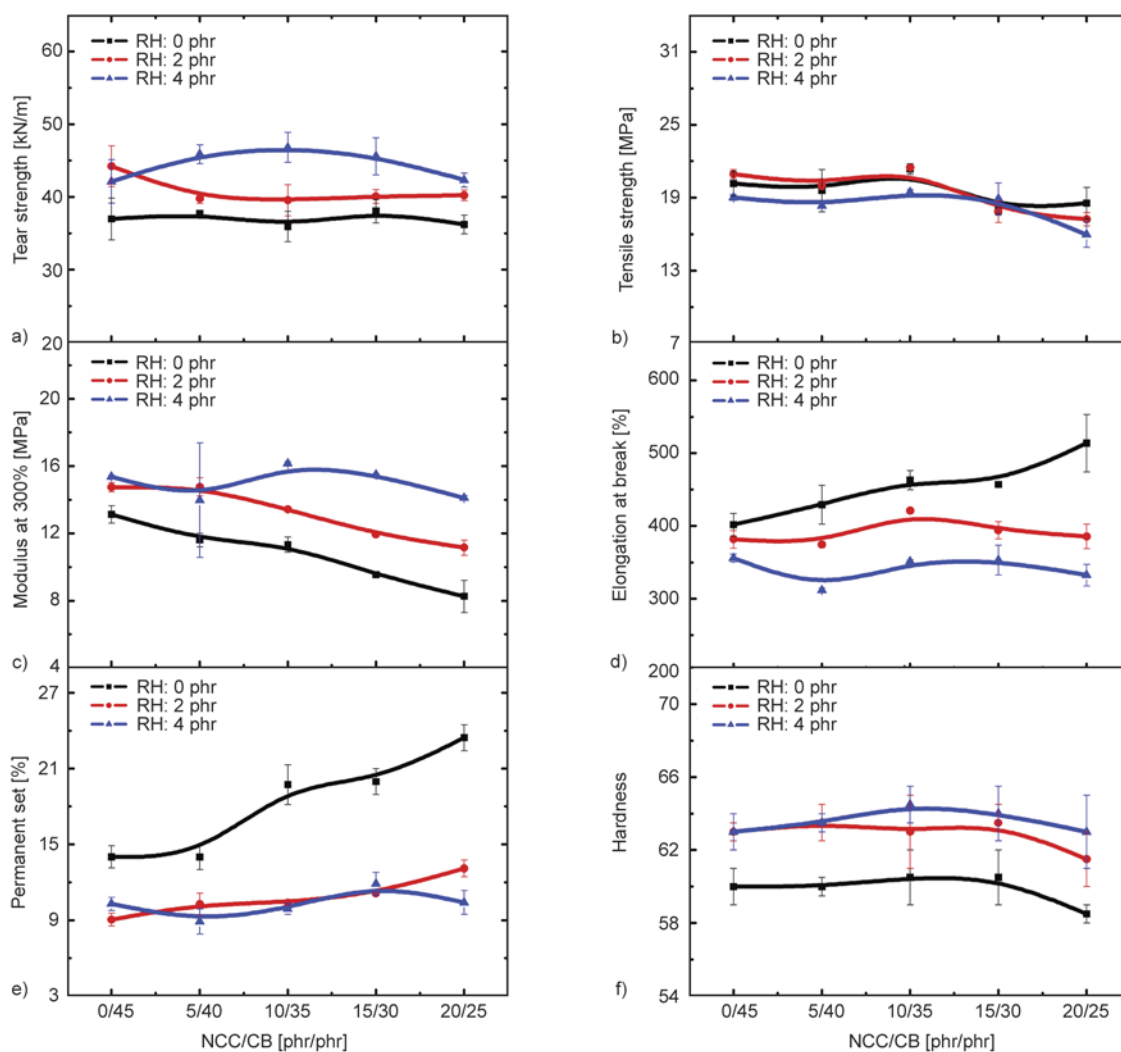

Figure 11. Mechanical properties of NR/BR/SBR composites reinforced by NCC and CB, (a) tear strength; (b) tensile strength; (c) modulus at 300%; (d) elongation at break; (e) permanent set; (f) hardness

and nonpolar rubber matrix. The incorporation of RH eliminated those defects: permanent set was obviously decreased, so did the increasing rate as a function of NCC content; modulus at 300% was enhanced and the tendency did not always decline as NCC increased. Tear strength and hardness were also markedly improved by RH. Among various fillers ratios, 10/35 was the optimal one to obtain the best mechanical properties, which may be a result of the good synergistic reinforcement of the two kinds of filler network.

4. Conclusions

Acid hydrolysis was adopted to obtain NCC, which was a kind of nanomaterial and possessed perfect crystal structure. Then, resulting NCC had been used to reinforce NR/BR/SBR blends as the substitute of CB. SEM images revealed good dispersion of NCC in blends. The RH strengthened the interaction of NCC and matrix. DMA revealed comparable reinforcement of NCC with CB. Mechanical properties showed samples with a high NCC loading of 10 phr performed best behaviors, indicating good reinforcing effect of NCC. The incorporation of RH would further improve the mechanical properties. In summary, NCC partially replacing CB, through stated method, led to well performance of NR/BR/SBR blends according to investigated aspects, along with environmental benefits and economic interests.

Acknowledgements

References
[1] Azizi Samir M. A. S., Alloin F., Dufresne A.: Review of recent research into cellulosic whiskers, their properties and their application in nanocomposite field. Biomacromolecules, **6**, 612–626 (2005).
DOI: 10.1021/bm0493685

[2] Siró I., Plackett D.: Microfibrillated cellulose and new nanocomposite materials: A review. Cellulose, **17**, 459–494 (2010).
DOI: 10.1007/s10570-010-9405-y

[3] Favier V., Chanzy H., Cavaille J. Y.: Polymer nanocomposites reinforced by cellulose whiskers. Macromolecules, **28**, 6365–6367 (1995).
DOI: 10.1021/ma00122a053

[4] Muniandy K., Ismail H., Othman N.: Effects of partial replacement of rattan powder by commercial fillers on the properties of natural rubber composites. Bioresources, **7**, 4640–4657 (2012).

[5] Kanking S., Niltui P., Wimolmala E., Sombatsompop N.: Use of bagasse fiber ash as secondary filler in silica or carbon black filled natural rubber compound. Materials and Design, **41**, 74–82 (2012).
DOI: 10.1016/j.matdes.2012.04.042

[6] Pasquini D., Teixeira E. M., Curvelo A. A. S., Belgacem M. N., Dufresne A.: Extraction of cellulose whiskers from cassava bagasse and their applications as reinforcing agent in natural rubber. Industrial Crops and Products, **32**, 486–490 (2010).
DOI: 10.1016/j.indcrop.2010.06.022

[7] Wang D., Shang S-B., Song Z-Q., Lee M-K.: Evaluation of microcrystalline cellulose prepared from kenaf fibers. Journal of Industrial and Engineering Chemistry, **16**, 152–156 (2010).
DOI: 10.1016/j.jiec.2010.01.003

[8] Martins M. A., Forato L. A., Mattoso L. H. C., Colnago L. A.: A solid state ^{13}C high resolution NMR study of raw and chemically treated sisal fibers. Carbohydrate Polymers, **64**, 127–133 (2006).
DOI: 10.1016/j.carbpol.2005.10.034

[9] Jacob M., Thomas S., Varughese K. T.: Mechanical properties of sisal/oil palm hybrid fiber reinforced natural rubber composites. Composites Science and Technology, **64**, 955–965 (2004).
DOI: 10.1016/S0266-3538(03)00261-6

[10] Bras J., Hassan M. L., Bruzesse C., Hassan E. A., El-Wakil N. A., Dufresne A.: Mechanical, barrier, and biodegradability properties of bagasse cellulose whiskers reinforced natural rubber nanocomposites. Industrial Crops and Products, **32**, 627–633 (2010).
DOI: 10.1016/j.indcrop.2010.07.018

[11] Xu S. H., Gu J., Luo Y. F., Jia D. M.: Effects of partial replacement of silica with surface modified nanocrystalline cellulose on properties of natural rubber nanocomposites. Express Polymer Letters, **6**, 14–25 (2012).
DOI: 10.3144/expresspolymlett.2012.3

[12] Karaağaç B.: Use of ground pistachio shell as alternative filler in natural rubber/styrene–butadiene rubber-based rubber compounds. Polymer Composites, **35**, 245–252 (2014).
DOI: 10.1002/pc.22656

[13] Hamed G. R.: Reinforcement of rubber. Rubber Chemistry and Technology, **73**, 524–533 (2000).
DOI: 10.5254/1.3547603

[14] Cao X., Xu C., Liu Y., Chen Y.: Preparation and properties of carboxylated styrene-butadiene rubber/cellulose nanocrystals composites. Carbohydrate Polymers, **92**, 69–76 (2013).
DOI: 10.1016/j.carbpol.2012.09.054

[15] Cao X., Xu C., Wang Y., Liu Y., Liu Y., Chen Y.: New nanocomposite materials reinforced with cellulose nanocrystals in nitrile rubber. Polymer Testing, **32**, 819–826 (2013).
DOI: 10.1016/j.polymertesting.2013.04.005

[16] Ljungberg N. J., Bonini C., Bortolussi F., Boisson C., Heux L., Cavaillé J. Y.: New nanocomposite materials reinforced with cellulose whiskers in atactic polypropylene: Effect of surface and dispersion characteristics. Biomacromolecules, **6**, 2732–2739 (2005).
DOI: 10.1021/bm050222v

[17] Bhattacharyya S. K., Parmar B. S., Chakraborty A., Dasgupta S., Mukhopadhyay R., Bandyopadhyay A.: Exploring microcrystalline cellulose (MCC) as a green multifunctional additive (MFA) in a typical solution-grade styrene butadiene rubber (S-SBR)-based tread compound. Industrial and Engineering Chemistry Research, **51**, 10649–10658 (2012).
DOI: 10.1021/ie301268e

[18] Geethamma V. G., Thomas Mathew K., Lakshminarayanan R., Thomas S.: Composite of short coir fibres and natural rubber: Effect of chemical modification, loading and orientation of fibre. Polymer, **39**, 1483–1491 (1998).
DOI: 10.1016/S0032-3861(97)00422-9

[19] Sui G., Zhong W. H., Yang X. P., Yu Y. H.: Curing kinetics and mechanical behavior of natural rubber reinforced with pretreated carbon nanotubes. Materials Science and Engineering: A, **485**, 524–531 (2008).
DOI: 10.1016/j.msea.2007.09.007

[20] Segal L., Creely J. J., Martin A. E., Conrad C. M.: An empirical method for estimating the degree of crystallinity of native cellulose using the X-ray diffractometer. Textile Research Journal, **29**, 786–794 (1959).
DOI: 10.1177/004051755902901003

[21] Flory P. J., Rehner Jr J.: Statistical mechanics of cross-linked polymer networks II. Swelling. The Journal of Chemical Physics, **11**, 521–626 (1943).
DOI: 10.1063/1.1723792

[22] Sassi J-F., Chanzy H.: Ultrastructural aspects of the acetylation of cellulose. Cellulose, **2**, 111–127 (1995).
DOI: 10.1007/BF00816384

[23] Zhang J., Pan S.: Study on the FTIR of microcrystalline celluloses. Journal of Cellulose Science and Technology, **3**, 22–27 (1995).

[24] Payne A. R.: Strainwork dependence of filler-loaded vulcanizates. Journal of Applied Polymer Science, **8**, 2661–2686 (1964).
DOI: 10.1002/app.1964.070080614

[25] Payne A. R., Whittaker R. E.: Low strain dynamic properties of filled rubbers. Rubber Chemistry and Technology, **44**, 440–478 (1971).
DOI: 10.5254/1.3547375

[26] Dannenberg E. M.: Bound rubber and carbon black reinforcement. Rubber Chemistry and Technology, **59**, 512–524 (1986).
DOI: 10.5254/1.3538213

[27] Wang M. J.: Effect of filler-elastomer interaction on tire tread performance Part I: Hysteresis of filled vulcanizates. Kautschuk und Gummi, Kunststoffe, **60**, 438–443 (2007).

[28] Xu S., Gu J., Luo Y., Jia D., Yan L.: Influence of nanocrystalline cellulose on structure and properties of natural rubber/silica composites. Polymer Composites, in press (2014).
DOI: 10.1002/pc.23005

[29] Wang M-J.: Effect of polymer-filler and filler-filler interactions on dynamic properties of filled vulcanizates. Rubber Chemistry and Technology, **71**, 520–589 (1998).
DOI: 10.5254/1.3538492

[30] Bahl K., Jana S. C.: Surface modification of lignosulfonates for reinforcement of styrene–butadiene rubber compounds. Journal of Applied Polymer Science, **131**, 40123/–40123/9 (2014).
DOI: 10.1002/app.40123

[31] Darwish N. A.: Effect of bonding systems on the adhesion of nitrile rubber to nylon cord. Polymer-Plastics Technology and Engineering, **39**, 793–806 (2000).

[32] Gu J., Chen W-J., Lin L., Luo Y-F., Jia D-M.: Effect of nanocrystalline cellulose on the curing characteristics and aging resistance properties of carbon black reinforced natural rubber. Chinese Journal of Polymer Science, **31**, 1382–1393 (2013).
DOI: 10.1007/s10118-013-1340-6

[33] Liu Y. B., Li L., Wang Q.: Reinforcement of natural rubber with carbon black/nanoclay hybrid filler. Plastics, Rubber and Composites, **39**, 370–376 (2010).
DOI: 10.1179/174328910X12691245469871

[34] Avalos F., Ortiz J. C., Zitzumbo R., López-Manchado M. A., Verdejo R., Arroyo M.: Effect of montmorillonite intercalant structure on the cure parameters of natural rubber. European Polymer Journal, **44**, 3108–3115 (2008).
DOI: 10.1016/j.eurpolymj.2008.07.020

[35] Favier V., Canova G. R., Cavaillé J. Y., Chanzy H., Dufresne A., Gauthier C.: Nanocomposite materials from latex and cellulose whiskers. Polymers for Advanced Technologies, **6**, 351–355 (1995).
DOI: 10.1002/pat.1995.220060514

Effect of surface modification of BiFeO₃ on the dielectric, ferroelectric, magneto-dielectric properties of polyvinylacetate/BiFeO₃ nanocomposites

O. P. Bajpai[1], J. B. Kamdi[1], M. Selvakumar[1], S. Ram[2], D. Khastgir[1], S. Chattopadhyay[1*]

[1]Rubber Technology Centre, Indian Institute of Technology, Kharagpur 721302, India
[2]Materials Science Centre, Indian Institute of Technology, Kharagpur 721302, India

Abstract. Bismuth ferrite (BiFeO₃) is considered as one of the most promising materials in the field of multiferroics. In this work, a simple green route as well as synthetic routes has been used for the preparation of pure phase BiFeO₃. An extract of *Calotropis Gigantea* flower was used as a reaction medium in green route. In each case so formed BiFeO₃ particles are of comparable quality. These particles are in the range of 50–60 nm and exhibit mixed morphology (viz., spherical and cubic) as confirmed by TEM analysis. These pure phase BiFeO₃ nanoparticles were first time surface modified effectively by mean of two silylating agent's viz., tetraethyl orthosilicate (TEOS) and (3-Aminopropyl)triethoxysilane (APTES). Modified and unmodified BiFeO₃ nanoparticles were efficiently introduced into polyvinylacetate (PVAc) matrix. It has been shown that nanocomposite prepared by modified BiFeO₃ comprise superior dispersion characteristics, improved ferroelectric properties and favorable magneto-dielectric properties along with excellent wettability in compare to nanocomposite prepared by unmodified BiFeO₃. These preliminary results demonstrate possible applications of this type of nanocomposites particularly in the field of multiferroic coating and adhesives.

Keywords: polymer composites, multiferroics, magnetic properties, polyvinylacetate, Calotropis Gigantea

1. Introduction

Bismuth ferrite (BiFeO₃) is one of the most promising materials owing to its favorable room temperature multiferroic characteristics [1–8]. In recent time, structure and properties of bismuth ferrite have been intensively studied because it comprises both ferromagnetic as well as ferroelectric characteristics simultaneously. As a result, an electric field can induce change in magnetization and an external magnetic field can induce electric polarization. This phenomenon is known as the magneto-electric effect [9]. However, current leakage problem of BiFeO₃ constricts its practical applications [10–12]. To resolve current leakage problem as reported in literature, one must come up with a potential route

for the preparation of impurity free BiFeO₃. To date, synthesis of pure phase BiFeO₃ is still a challenging task. So far, bismuth ferrite particles were prepared mostly by the solid state and solution chemistry methods (i.e., precipitation/co-precipitation, sol-gel, hydrothermal and sonochemical) [13–19]. However, it resulted in the formation of coarser particles. Therefore, we tried to synthesize pure phase bismuth ferrite via controlled sol-gel process through a green route by using flower extract of *Calotropis Gigantea* in dilute concentration of acid at low temperature. We choosed plant extract process because synthesis mediated by plant extracts is eco-friendly, economical and can provide nanoparticles with minimum toxicity. *Calotropis Gigantea* is a shrub com-

---

mon in the eastern and southern parts of India, Ceylon and Eastern Asia. The milky juice obtained from *Calotropis Gigantea* is used for medicinal and insecticidal purposes [20]. The roots and leaves of *Calotropis Gigantea* are also used traditionally for treatment of abdominal tumors, boils, syphilis, leprosy, insect-bites and elephantiasis [21]. Extract of *Calotropis Gigantea*n leaves also has significant antioxidant property. As reported in literature, there are numerous bio-organic compounds present in the plant systems such as flavonoids, terpenoids, proteins, reducing sugars and alkaloids [22, 23]. These bio-organic compounds are supposed to be involved either as reducing agents or as stabilizing agent in the formation of nanoparticles. It is assumed that formation of nanoparticles occurs through the ionic or electrostatic interactions between the metal complexes and the functional groups on the biomass surfaces. But due to the bio-diversity of the plant biomasses, the exact mechanism by which bio-constituents of plants have contributed to the synthesis process is so far not completely understood.

Moreover, though $BiFeO_3$ have many favorable properties, but still it is difficult to used directly. Being ceramic, as such $BiFeO_3$ is brittle in nature, very less shock resistive and has poor moldability [24]. To make it even more advantageous these disabilities ought to be rectified. The best way to do so is by making the composite of $BiFeO_3$ with a suitable polymer, since most of the polymers have better shock resistance, easy processability and being cheaper too. Also by judicious selection of polymer with some specific attributes, potential applications including in the field of adhesives and coatings of new composite material can be envisaged [25–27]. Large array piezoelectric devices and miscellaneous electromagnetic devices need joints or coatings. For these, coating materials are supposed to have electromagnetic properties as well as the ability to spread and wet the surface. Though, today we have a large gamut of polymers of diverse applications but considering above mentioned facts, we have chosen polyvinyl acetate (PVAc) for this work. PVAc is a type of thermoplastic with hydrophobic nature and comprises the characteristics of coating and adhesive [28–30]. As a result, ultimate product of $BiFeO_3$/ PVAc composite can be used in the field of magneto-electric coating or adhesives. Magneto-electric adhesives can be used to adjoin piezoelectric, magnetic or multiferroic components [31]. This compound may also be used for under water applications with adjustable buoyancy. Major concern about the polyvinyl acetate is the sensitivity of ester groups to base hydrolysis. With time PVAc also slowly converts into polyvinyl alcohol and acetic acid. Hence, necessary precaution should be taken accordingly. Thus owing to broad efficacy of $BiFeO_3$, properties of bismuth ferrite polymer nanocomposites must be explored, but interestingly very limited number of literature on the related area is available so far [32–35]. Therefore, motivated from above mentioned issues we prepared $BiFeO_3$ nanoparticles via sol-gel process through a green route by using flower extract of *Calotropis Gigantea* as well as by using other complexing agent (citric acid) and dispersant (polyethylene glycol) at lower temperature. Till now synthesis of gold and silver nanoparticles have been reported by using this type of extract, but there is no paper available on $BiFeO_3$ synthesis [36–38]. To achieve required properties of composites proper dispersion of $BiFeO_3$ into polymer matrix is desirable. Hence, prepared $BiFeO_3$ nanoparticles were first time surface modified by means of two different silanes viz., tetraethyl orthosilicate and (3-Aminopropyl)triethoxysilane [39]. Subsequently, modified and unmodified $BiFeO_3$ nanoparticles were introduced into polyvinyl acetate matrix to make this novel class of nanocomposite.

2. Experimental
2.1. Materials
For preparation of $BiFeO_3$ raw materials such as bismuth nitrate pentahydrate $[Bi(NO_3)_3 \cdot 5H_2O]$, iron nitrate nonahydrate $[Fe(NO_3)_3 \cdot 9H_2O]$, anhydrous citric acid, polyethylene glycol (MW- 600 Da) and nitric acid (69% GR) were obtained from Merck Specialties Chemicals Ltd, Mumbai, India (Analytical grade, 99% purity). Silane based surface modifier e.g., tetraethyl orthosilicate (TEOS) and (3-Aminopropyl)triethoxysilane (APTES) were purchased from Sigma Aldrich, USA. Complexing agent from bio-resources e.g., leaves and flowers of *Calotropis Gigantea* were collected from Agriculture & Food Department, IIT Kharagpur, India. Polyvinyl acetate (PVAc) of molecular weight (4.2·10^5 Da) was purchased from Pidilite Industries Ltd, Mumbai, India. It has (92±2)% polyvinyl acetate content and (5±1)% polyvinyl alcohol. All these materials were used as such without any further purification.

2.2. Preparation of extract of *Calotropis Gigantea* flower

The leaves and flowers were initially separated from the main plant's body and rinsed with distilled water. After proper washing with distilled water, they were cut into small pieces. Then 5 g petals were weighed and mixed with 20 mL distilled water. Subsequently, this mixture is subjected to 1.5 h of heating at 85°C and cooled up to room temperature. Afterward, petals were separated through filtration process and extract obtained is concentrated and used later as a complexing agent for the preparation of bismuth ferrite nanoparticles.

2.3. Preparation of BiFeO₃ nanoparticles

To prepare BiFeO₃ nanoparticles by extract route, 0.04 M [Bi(NO$_3$)$_3$·5H$_2$O] and 50 mL concentrated flower extract were mixed together, and solution was ultrasonicated about 30 minute followed by microwave treatment about three minute (at 900 Watt) to make it dry. Subsequently, solution of 50 mL concentrated flower extract and 0.04 M [Fe(NO$_3$)$_3$.9H$_2$O] were added into it followed by six minutes of microwave treatment (at 900 Watt). This resulted in blackish fluffy powder which is further annealed at 600°C.

To prepare BiFeO₃ nanoparticles by synthetic route, bismuth nitrate pentahydrate [Bi(NO$_3$)$_3$·5H$_2$O] and iron nitrate nonahydrate [Fe(NO$_3$)$_3$·9H$_2$O] were taken in equimolar proportion, and dissolved in distill water to make a solution of 0.2 M followed by five minutes of stirring. While stirring, 20 mL dilute HNO$_3$ (20%) solution was added to the mixture. Thereafter 12 g of citric acid was added to the solution followed by the addition of 2 g of PEG as dispersant (addition of PEG can be optional). Resultant yellowish solution was heated with continuous stirring of about 1 h. Subsequently, concentrated solution mixture was kept into oven at 150°C for 5 h to get powdered material. In addition to this, powdered material was annealed at 600°C.

Following above processes, four different types of samples of BiFeO₃ were prepared [e.g., prepared by using a complexing agent (a) citric acid, (b) citric acid with PEG, (c) none (without complexing agent), and (d) an extract of a *Calotropis Gigantea* flower]. Subsequently, crystal structure as well as surface functionality was analyzed by X-ray diffraction and FTIR techniques.

2.4. Surface modification of BiFeO₃ nanoparticles

Prepared BiFeO₃ nanoparticles were surface modified by means of two different silylating agent's viz., tetraethyl orthosilicate (TEOS) and (3-Aminopropyl)triethoxysilane (APTES). In the process of surface modification a mixture of 100 mg BiFeO₃, 80 mL ethanol and 50 mL water was taken in a round bottom flask and ultrasonication for 1 h. Thereafter, 20 mL 30% ammonia solution was added followed by 6 h of mechanical stirring. While stirring silylating agent's (e.g., TEOS or APTES) were added dropwise (0.1 mL in 10 mL of water) at room temperature. After 6 h of stirring silica coated nanoparticles were separated and washed 4–5 times by using ethanol and distilled water. Subsequently, prepared nanoparticles were dried in vacuum oven and used for the preparation of nanocomposite with PVAc.

2.5. Preparation of PVAc/BiFeO₃ nanocomposite

PVAc/BiFeO₃ nanocomposite films were prepared via simple solution casting technique. In the process 4 g of PVAc was dissolved in the 20 mL of distilled water followed by 30 minutes of ultrasonication. Subsequently, 80 mg of BiFeO₃ nanoparticles were separately mixed, and resultant solution was ultrasonicated for 30 minutes. Then both solutions were mixed together under mechanical stirring and further ultrasonicated for 4 h. Thereafter blend solution were cast in teflon petri dish and dried at room temperature (about 10 days) to get smooth films. Following above process four different samples [viz., PVAc reinforced with 2.0 wt% of (a) pristine BiFeO₃, (b) TEOS modified BiFeO₃, (c) APTES modified BiFeO₃ and (d) neat PVAc] were prepared and characterized.

2.6. Characterization techniques

Structural phase analysis was carried out by X-ray powder diffraction using Philips PW-1710 X-ray diffractometer with CuK$_\alpha$ radiation ($\lambda = 1.54$ Å) at accelerating voltage of 40 kV and at a beam current of 20 mA. Fourier transform infrared spectroscopy (FTIR) studies were performed on a Perkin Elmer FTIR spectrophotometer by using KBr pellets. Morphology analysis was performed on an Analytical TEM (FEI-TECHNAI G2 20S-TWIN, USA) at operating voltage 200 kV. Field Emission Scanning

Electron Microscopy (FESEM) and dot mapping was carried out with an (Model SUPRA 40 Field Emission Scanning Electron Microscope) acceleration voltage 10.0 kV. Thermo gravimetric analysis (TGA) was carried out in a TGA Q50 (TA instrument, USA) from ambient temperature to 600°C at a programmed heating rate of 20°C/min in nitrogen atmosphere. The contact angle measurement was performed by using dynamic contact angle analyzer (Model: FTA 200-First Ten Angstroms, Virginia, USA). The dielectric properties were measured using precision LCR meter (Model. Quad Tech 7600) coupled with a home-made cell that has parallel plate circular electrodes (up to MHz). M-H loop measurements were carried out up to the field strength 2.5 T using SQUID VSM DC magnetometer, Quantum Design, USA. Ferroelectric behavior was examined at room temperature using an automatic P-E loop tracer manufactured by Marine India Elect. Pvt. Ltd. Magneto-dielectric measurement were carried out up to the field strength 1.93 T with applied current ranging from 0.05 to 3 A.

3. Results and discussion
3.1. Characterization of $BiFeO_3$
3.1.1. X-ray diffraction analysis
Figure 1 illustrates XRD patterns of the annealed $BiFeO_3$ synthesized by using different complexing agents. It is apparent that well crystalline $BiFeO_3$ formed in both cases (e.g., citric acid and green route). In both cases so formed $BiFeO_3$ pa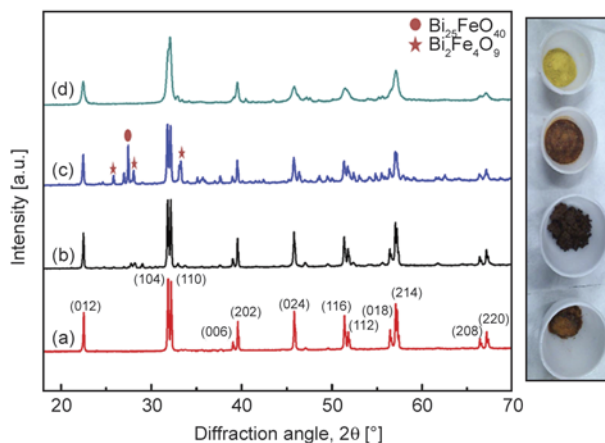rticles are of comparable quality. All peaks specify the formation of rhombohedral structure of $BiFeO_3$ with lattice parameters $a = b = 5.57$ Å, $c = 13.86$ Å and space group *R3c* (161). These are well consistent with reported data (JCPDS No.86-1518). Sample prepared without complexing agent and with PEG also confirms the formation of $BiFeO_3$ but with slight indication of phase impurity (viz., $Bi_2Fe_4O_9$ and $Bi_{25}FeO_{40}$) [40]. Interestingly, it is also observed that all four samples display different colors before annealing (side view, Figure 1).

3.1.2. FTIR analysis
Figure 2 illustrates FTIR spectra showing the effect of complexing agents on precursors used to synthesize $BiFeO_3$. Absorptive band at around 400–600 cm^{-1} in all samples indicate formation of FeO_6 octahedra of the perovskite structure. These peaks are due to the Fe–O stretching and bending vibration which confirms formation of metal-oxygen bond. In Figure 2 curve d absorption bands at around 1040–1150, 1350–1480 and 1350–1480 cm^{-1} are the characteristics of C–O stretching, C–H bending and C=O stretching respectively. Existence of carbonyl group indicates that some amounts of bio-organic compounds are still present in the sample prepared by extract process. Therefore extract process needs some additional steps to remove excess amount of bio-organic compounds. Bands at around 810–820 cm^{-1} are due to the presence of traces of trapped NO_3^- ion in the sample. Thus, FTIR study confirms

Figure 1. XRD patterns of $BiFeO_3$ prepared by using a complexing agent (curve a) citric acid, (curve b) citric acid with PEG (dispersant), (curve c) none (without complexing agent), and (curve d) an extract of a *Calotropis Gigantea* flower, with photographs of the samples before annealing in the right
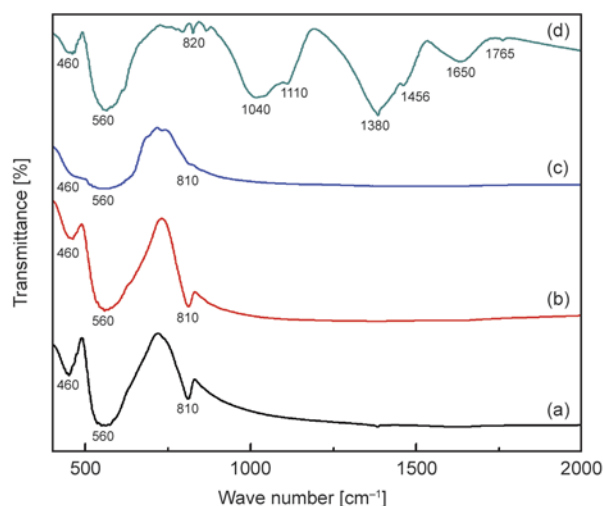

Figure 2. FTIR spectra showing the effect of a complexing agent on a precursor used to obtain $BiFeO_3$ (curve a) citric acid, (curve b) citric acid with PEG (dispersant), (curve c) none (without complexing agent), and (curve d) an extract of a *Calotropis Gigantea* flower

the formation of perovskite structure of prepared $BiFeO_3$.

3.2. Characterization of surface modified $BiFeO_3$

3.2.1. FTIR analysis

Figure 3 illustrates FTIR spectra showing effect of surface modification on $BiFeO_3$. Absorption bands at 1075 and 1070 cm^{-1} are present in the modified samples, which are assigned to the asymmetric stretching vibrations of the Si–O–Si bond. These bands confirm surface modification of prepared $BiFeO_3$. However, absorption bands at 400–600, 2920, 2860 and 3310 cm^{-1} are the characteristics of Fe–O stretching, symmetric and asymmetric stretching of (–CH_2–) and –NH_2 stretching respectively. Bands at around 810–820 and 2340 cm^{-1} are
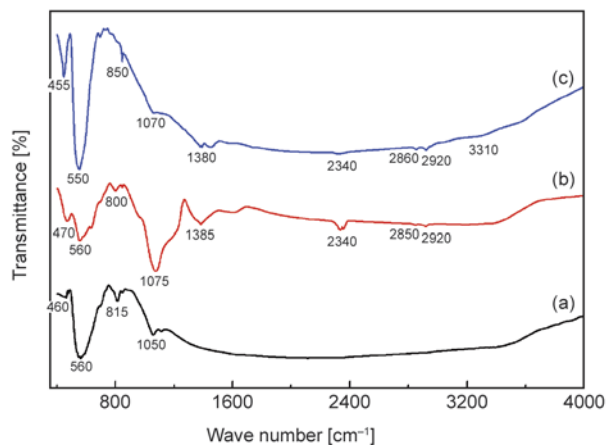
Figure 3. FTIR spectra of (curve a) pristine $BiFeO_3$, (curve b) TEOS modified $BiFeO_3$, and (curve c) APTES modified $BiFeO_3$
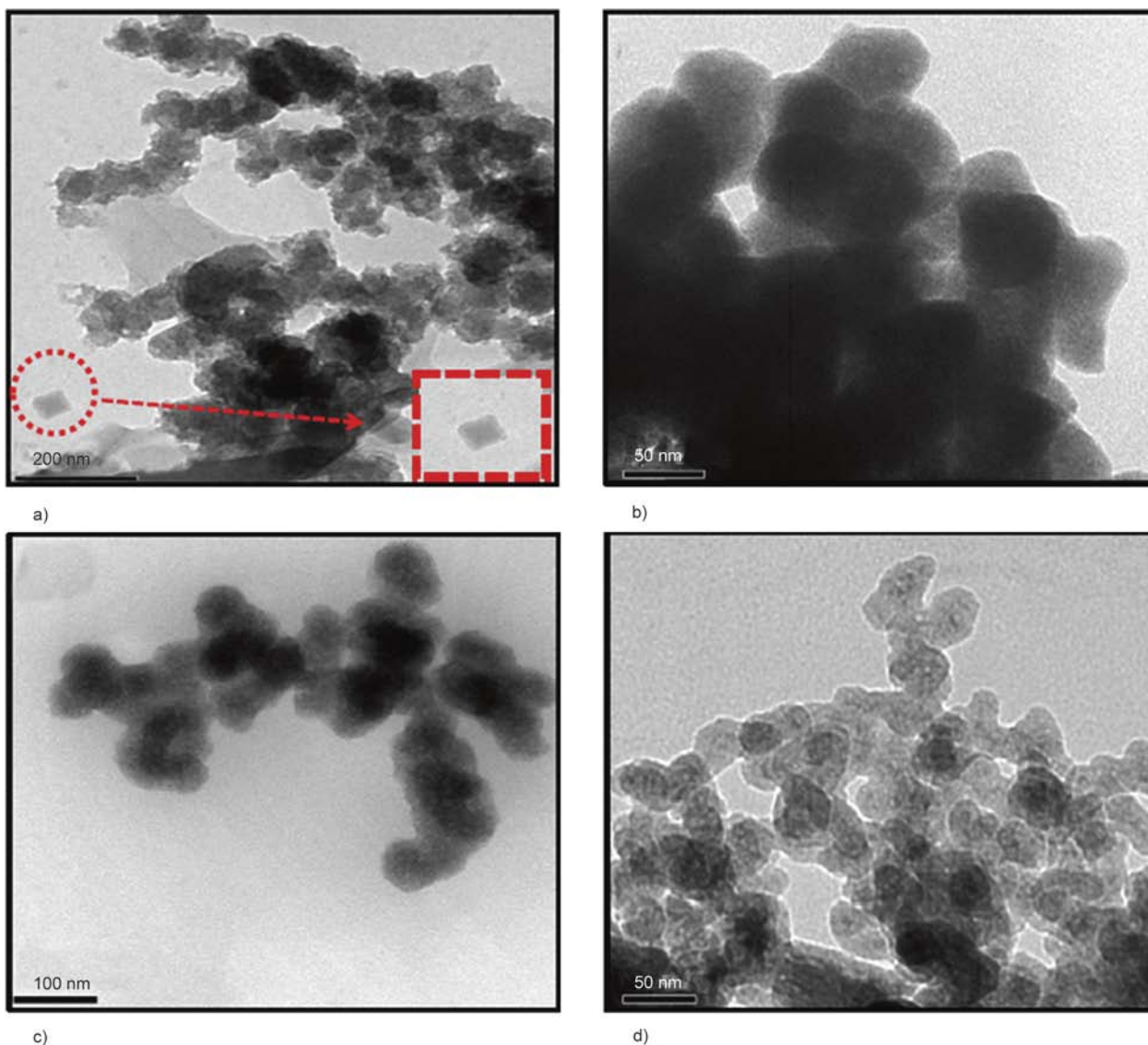
Figure 4. TEM images of (a, b) pristine $BiFeO_3$, (c) TEOS modified $BiFeO_3$, and (d) APTES modified $BiFeO_3$

due to the traces of trapped NO_3^- ion and CO_2 present in the sample.

3.2.2. Morphology by analytical TEM

Figure 4 displays TEM photomicrographs of $BiFeO_3$ before and after surface modification. It is clearly evident that before modification particles are very much agglomerated (Figure 4a, 4b), and these particles have mixed morphology (viz., spherical and cubic). However, nanoparticles modified by TEOS and APTES are comparatively well separated (Figure 4c, 4d). Approximate size range (50–60 nm) of the prepared $BiFeO_3$ has been obtained by image analysis of TEM photomicrographs.

3.3. Characterization of PVAc/BiFeO₃ nanocomposite

3.3.1. FESEM analysis

Figure 5 illustrates FESEM images of $BiFeO_3$/PVAc nanocomposites with 'Bi' dot mappings. It is distinctly observed that nanocomposite made by using unmodified $BiFeO_3$ exhibits very rough surface with lot of cracks and pores (Figure 5a). On the other hand, surface roughness is reasonably reduced in the case of nanocomposites made by modified $BiFeO_3$ with a lesser amount of cracks and pores (Figure 5b and 5c). Observed improvements in the

surface roughness of nanocomposites are due to the superior dispersion of modified $BiFeO_3$ in the PVAc matrix. This is further supported by the corresponding dot mapping images (Figure 5d–5f). Dot mapping micrographs clearly demonstrate enhanced dispersion of the nanoparticles in the case of nanocomposites made by modified $BiFeO_3$. Among all, nanocomposite prepared using TEOS modified $BiFeO_3$ exhibits best quality of dispersion.

3.3.2. Thermal analysis

Figure 6 illustrates TGA and DTA thermograms of neat PVAc and its $BiFeO_3$ based nanocomposites. It is apparent from TGA and DTA thermograms that decomposition of nanocomposites took place in two major steps (Figure 6). In first step majority of mass loss took place around 340°C. It could be due to the elimination of side groups (viz., acetate group), solvent and decomposition of chelated complex formed by citric acid. In second step, further smaller mass loss took place between 410 to 490°C. This might be due to the breakdown of the polymer backbone at higher temperatures. Perhaps due to the filler and impurities, a non volatile residue of approximately of 10 weight% is formed at the end. From the thermogram, it is clearly evident that thermal stability of the nanocomposites prepared by using modified
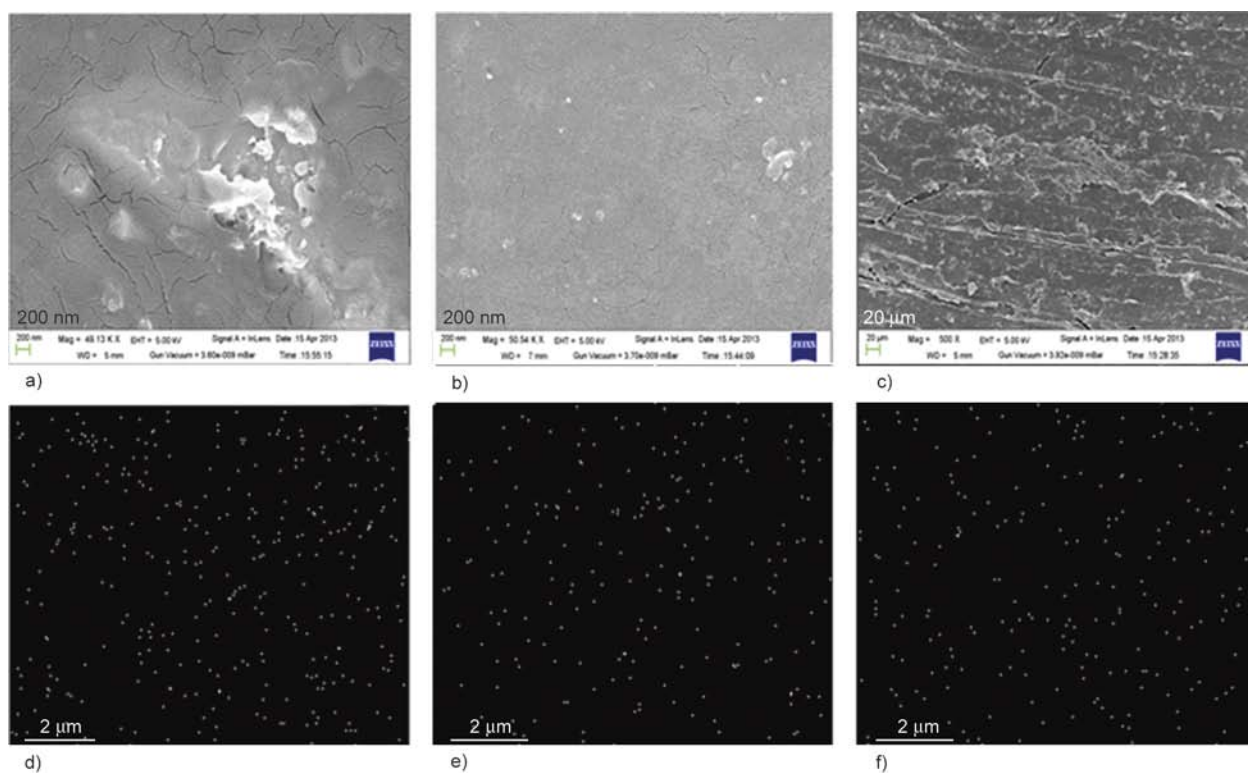

Figure 5. FESEM images of reinforced PVAc with 2.0 wt% of (a) pristine $BiFeO_3$, (b) TEOS modified $BiFeO_3$, and (c) APTES modified $BiFeO_3$, with (d–f) Bi dot mappings
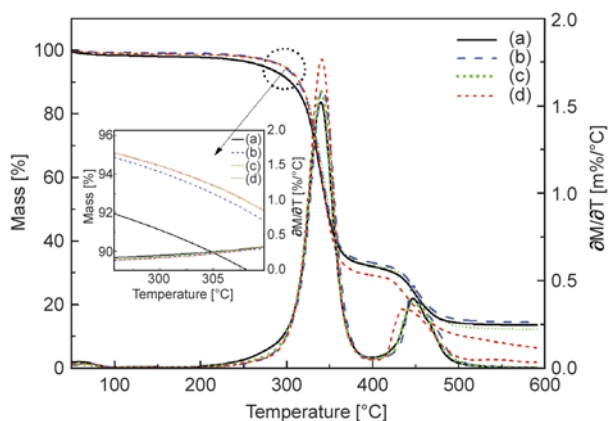
Figure 6. TGA and DTA thermograms of reinforced PVAc with 2.0 wt% of (curve a) pristine BiFeO$_3$, (curve b) TEOS modified BiFeO$_3$, (curve c) APTES modified BiFeO$_3$ and (curve d) neat PVAc, with magnified graph in the inset

BiFeO$_3$ is fairly enhanced as compared to nanocomposite prepared by using unmodified BiFeO$_3$ (Figure 6 inset). It is due the surface modification of the BiFeO$_3$ particles with silanes that improves its thermal stability. However, as compared to neat PVAc, the thermal stability of all nanocomposites moderately decreased. This decrease in thermal stability of the nanocomposites is attributed to the loss of crystallinity of the polymer chains due to BiFeO$_3$ loading, which accelerates thermal degradation of polymers by allowing easier diffusion of degradation products.

3.3.3. Dielectric analysis

Figure 7 illustrates the variation of permittivity and tan δ of neat PVAc and its BiFeO$_3$ based nanocomposites with frequency at room temperature. Lowest permittivity is found for the neat PVAc and measured permittivity at lower frequency is always greater than those at higher frequency. In the lower frequency range (e.g., 10–10^3 Hz) permittivity of the nanocomposites made by using TEOS modified BiFeO$_3$ is found similar to unmodified one, but somewhat lower permittivity is observed for nanocomposites made by using APTES modified BiFeO$_3$. However, in the higher frequency range (e.g., 10^4–10^6 Hz) permittivity is found higher for the nanocomposites made by using modified BiFeO$_3$ than those of unmodified one (Figure 7 inset).

In each case, as the frequency increases dielectric permittivity decrease significantly up to 10^4 Hz and beyond which the changes in the values are marginal. Actually at low frequency the dielectric permittivity depends upon various types of polarizations i.e., interfacial, ionic/dipolar, electronic, atomic polarization. However, at high frequency only electronic and atomic polarizations are responsible for constituting the permittivity. Consequently, there is a sharp decline in permittivity at low frequency, as at higher frequency interfacial and dipolar relaxation could not contribute significantly. But increase in the permittivity at higher frequency for the modified BiFeO$_3$ filled nanocomposites clearly indicates that silane coating enhances electronic or atomic polarizations. It may be due to the possible electronic interaction between silane coating agents and BiFeO$_3$ which ultimately lead to increase in the permittivity. This is what we also got in the magneto-dielectric measurement. Moreover, drastic
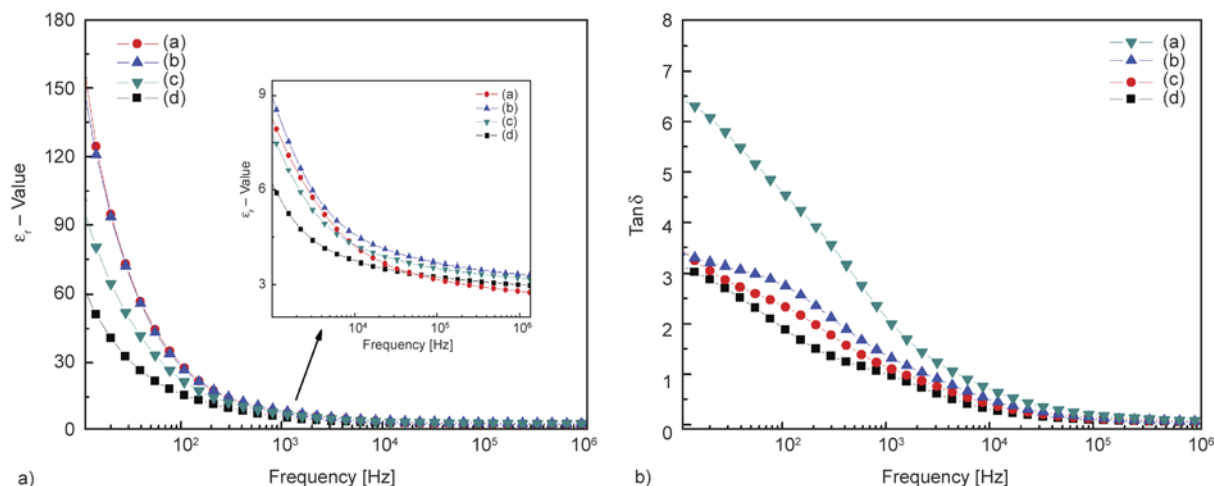

Figure 7. Variation of dielectric permittivity (a) and tan δ (b) of reinforced PVAc with 2.0 wt% of (curve a) pristine BiFeO$_3$, (curve b) TEOS modified BiFeO$_3$, (curve c) APTES modified BiFeO$_3$ and (curve d) neat PVAc, with magnified permittivity graph in the inset

increase in the permittivity for the $BiFeO_3$ filled nanocomposites are mainly due to the effect of high permittivity of filler ($BiFeO_3$) compared to the polymer matrix. The permittivity value of phase pure $BiFeO_3$ is more than 100 at kHz (e.g., even higher for less than kHz frequency) [41]. More or less similar behavior is observed in the $\tan\delta$ versus frequency plot of nanocomposites i.e., incessant decline of $\tan\delta$ in all cases. It is found highest for nanocomposites made by using unmodified $BiFeO_3$ and lowest for neat PVAc. This shows that nanocomposites prepared by using modified $BiFeO_3$ exhibits decrease of $\tan\delta$ significantly as compared to that of unmodified one.

3.3.4. Ferroelectric measurement

Ferroelectric hysteresis loops of $BiFeO_3$/PVAc nanocomposites at room temperature are shown in (Figure 8). It is evident that nanocomposites prepared by using modified $BiFeO_3$ show more remnant polarization and coercivity than those of unmodified one. Nanocomposite made by using TEOS modified $BiFeO_3$ exhibit superior ferroelectric properties with remnant polarization ($2Pr \approx 6.08$ μC/cm^2) and the coercive field ($2Ec \approx 21.89$ kV/cm). Whereas unmodified one shows remnant polarization ($2Pr$) $\approx$ 4.98 μC/cm^2. This is because coating of modifying agent on the surface of $BiFeO_3$ nanoparticles contributes additional polarizability, consequently improves ferroelectric properties. Observed values are good agreement for ferroelectric applications of $BiFeO_3$/PVAc nanocomposites material with low current leakage contribution.
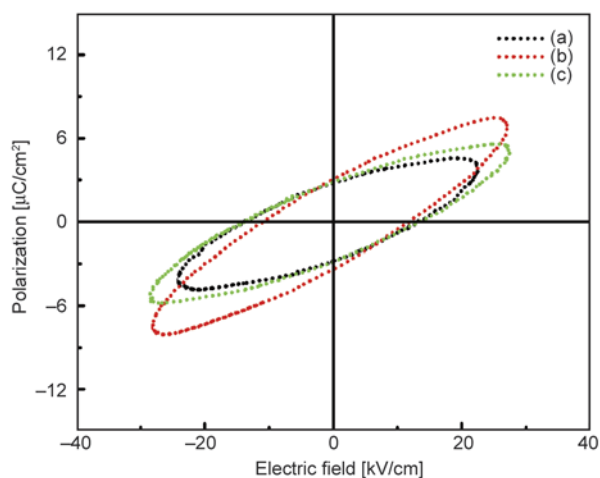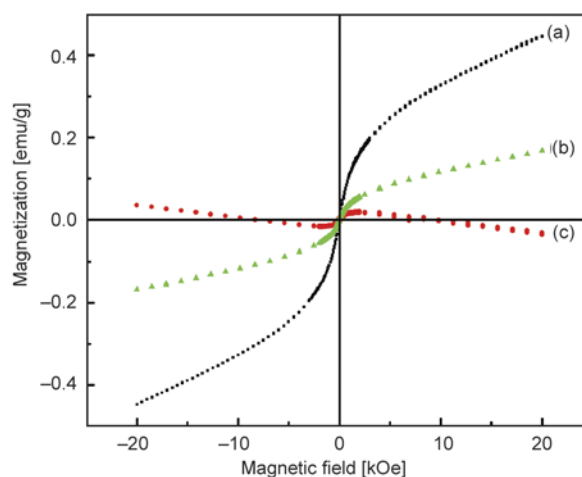

Figure 9. Magnetic hysteresis loops of reinforced PVAc with 2.0 wt% of (curve a) pristine $BiFeO_3$, (curve b) TEOS modified $BiFeO_3$, and (curve c) APTES modified $BiFeO_3$

3.3.5. Magnetic property measurement

Magnetic properties of the $BiFeO_3$/PVAc nanocomposites have been studied using SQUID VSM at room temperature (Figure 9). Measured *M–H* curves are indicative of super paramagnetic nature. However, nanocomposites made by using modified $BiFeO_3$ displays less magnetization than those of unmodified one and it is found lowest in case of nanocomposite prepared by using APTES modified $BiFeO_3$. This could be due to the drop of amount of $BiFeO_3$ per gram owing to coated outer surface and as a result magnetization (emu/g) decreased.

3.3.6. Magneto-dielectric analysis

Magneto-dielectric measurement characterizes degree of the coupling between magnetic and electric polarizations. Here change in dielectric constant with applied magnetic field is characterized by magneto-dielectric coupling or magneto-capacitive factor [$\approx (\varepsilon_H - \varepsilon_0)/\varepsilon_0 \cdot 100\%$].

The magnetocapacitive effect is relative to the term P^2M^2 (*P* – polarization, *M* – magnetization) in the Ginzburg–Landau free energy [9, 33]. In the multiferroic polymer nanocomposites, coupling of electric and magnetic phenomena happens through elastic interaction. Hence, magneto-electric effect in the composites is extrinsic in nature and depends on the composite microstructure and coupling interaction across the magnetic and ferroelectric interfaces.

Figure 10 illustrates magneto-dielectric response of reinforced PVAc with 2.0 wt% of modified and unmodified $BiFeO_3$ at different frequencies. It is dis-
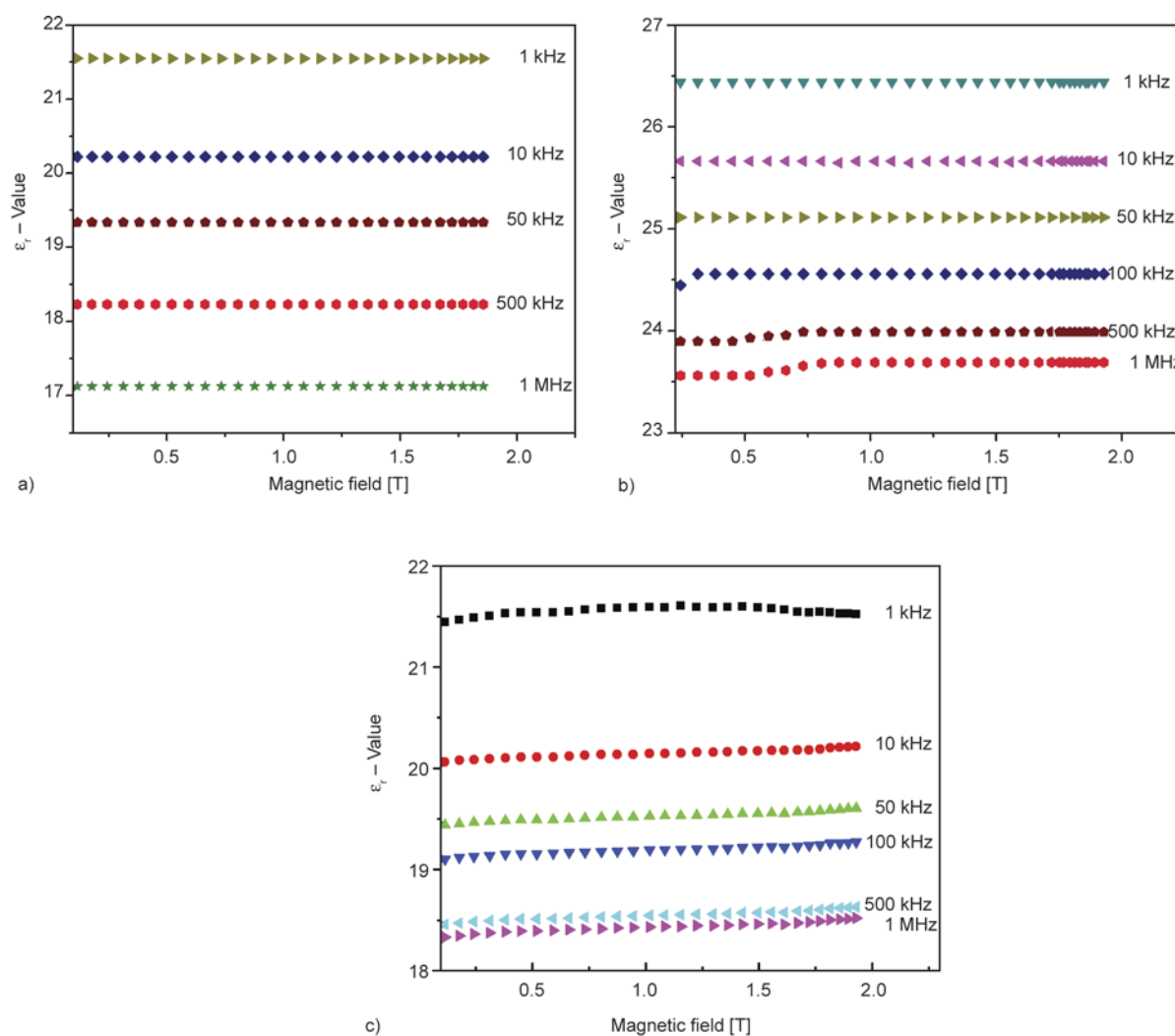

Figure 8. Comparison of *P–E* loops of reinforced PVAc with 2.0 wt% of (curve a) pristine $BiFeO_3$, (curve b) TEOS modified $BiFeO_3$, and (curve c) APTES modified $BiFeO_3$

Figure 10. Magneto-dielectric response of a reinforced PVAc with 2.0 wt% (a) pristine $BiFeO_3$, (b) TEOS modified $BiFeO_3$, and (c) APTES modified $BiFeO_3$ at different frequencies

tinctly observed that dielectric permittivity increases as magnetic field increases in case of nanocomposite made by using modified $BiFeO_3$ (Figure 10b, 10c). Generally, surface modification leads to decrease in the piezoelectricity of the nanocomposites due to the reduction of piezoelectric response of the resultant nanoparticles. But in our case modified $BiFeO_3$ based nanocomposites displays improved magneto-dielectric response. It means surface elastic interaction produced by the modifying agents may lead to change in the spin structure/magnetic moment of the $BiFeO_3$ near the interface, and ultimately produces better interfacial contacts. The change in the spin structure of the $BiFeO_3$ indicates alteration in the bond angle of Fe–O–Fe bonds of FeO_6 octahedra. As a result redistribution of charges and orientation of dipoles within the polymer matrix eventually produces higher coupling. Highest coupling

about 1.08% is observed in case of nanocomposite made by using APTES modified $BiFeO_3$. However, in case of nanocomposite made by using unmodified $BiFeO_3$ not much change in the dielectric permittivity is observed with change in magnetic field, and shows insignificant coupling (less than 0.10%) (Figure 10a). It may be due to the weak interfacial contacts between the dispersed nanoparticles in the matrix which leads to failure of transferring elastic strain/stress from one component (piezoelectric) to other component (magnetostrictive). Notable point about this material is that it contains only 2 wt% $BiFeO_3$ but still shows favorable magneto-dielectric properties especially modified one. Hence, it can be used for magneto-electric applications after the comprehensive assessment of magneto-electrical properties.

3.3.7. Contact angle measurement

Wetting ability of the nanocomposites was determined by the contact angle measurement (Figure 11). Even though polyvinyl acetate is hydrophobic in nature, contact angle of neat polymer sample is found 59° (less than 90°). As per specification of purchased polyvinyl acetate (mentioned in material section) it contains 5% polyvinyl alcohol (PVA) which is hydrophilic material. Therefore, as water comes in contact with mixture of hydrophobic (–COOCH$_3$ group) and hydrophilic (–OH group) material, hydrophilic material will move toward surface and hydrophobic material will move away. This makes shape like a ball in which –OH repeat units are on the outer surface while –COOCH$_3$ are on the inner side of the ball (i.e., away from water) (Figure 11a). Consequently, while measuring contact angle as the water drops fall on surface of the polymer, PVA will move towards the surface and being hydrophilic it gives less contact angle. This is the reason why neat polymer have contact angle less than 90°. On the other hand, in the case of nanocomposite made by unmodified BiFeO$_3$ contact angle is found more (~82°) than that of neat polymer (Figure 11b). This is because of the hydrophobic nature of bismuth ferrite. It is interesting to note that the water contact angle for the nanocomposites prepared from modified BiFeO$_3$ is found significantly low (~57°) compared (Figure 11c, 11d) to those of unmodified one (82°) that reflects its enhanced wettability in hydrophobic environment. These positive outcomes indicate possible applicability of BiFeO$_3$/ PVAc nanocomposites in the area of magnetic field controllable devices or in magneto-electric coatings and adhesives.
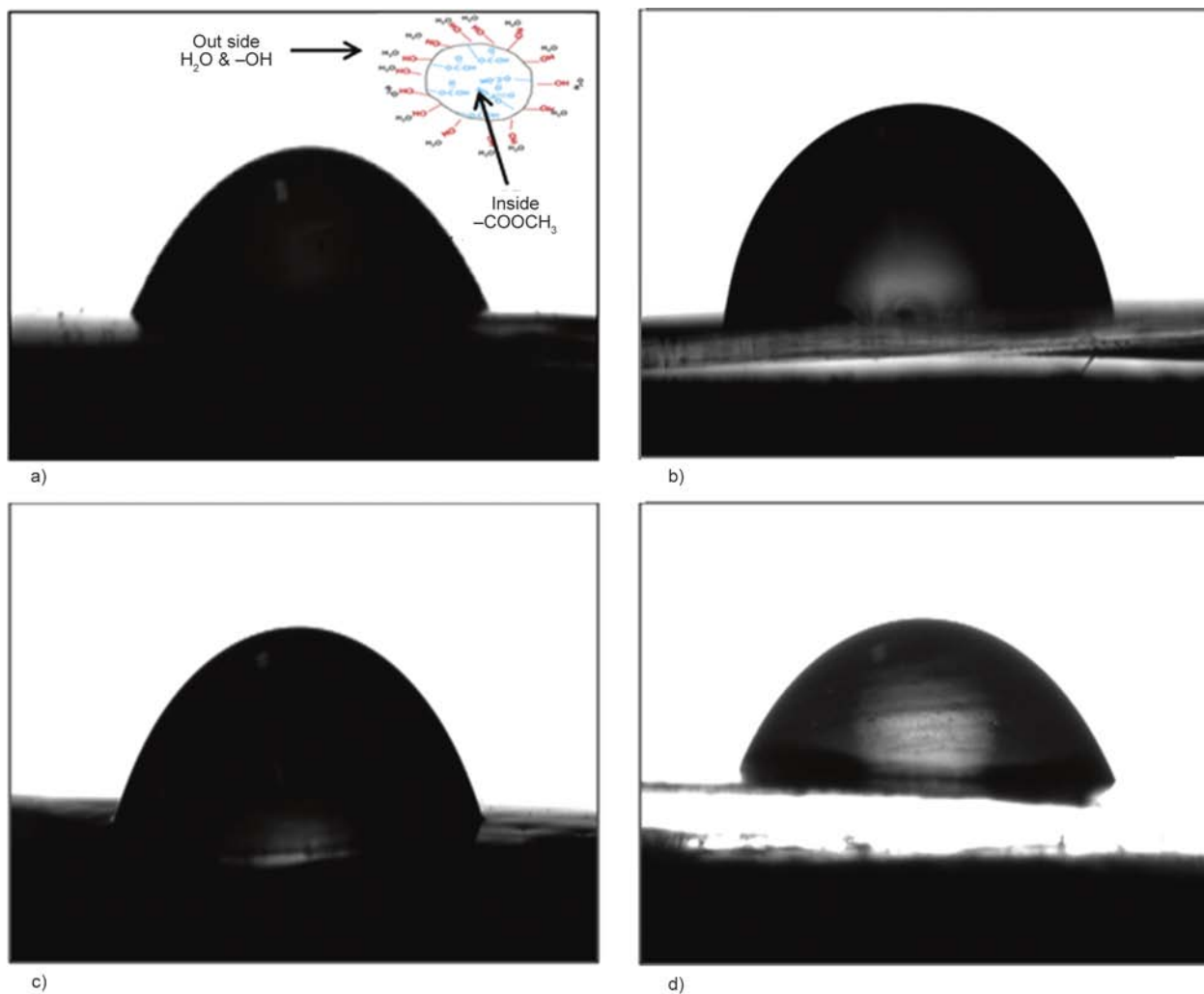

Figure 11. Contact angle images of (a) Neat PVAc, and reinforced PVAc with 2.0 wt% of (b) pristine BiFeO$_3$, (c) TEOS modified BiFeO$_3$, and (d) APTES modified BiFeO$_3$

4. Conclusions

First step toward synthesis of $BiFeO_3$ following a facile green route be accomplished effectively together with the synthetic route. In each case so formed $BiFeO_3$ particles are of comparable quality. Prepared $BiFeO_3$ nanoparticles were surface modified successfully by means of two different silanes (viz., TEOS and APTES). FESEM, TGA and contact angle analysis indicates nanocomposites made by using modified $BiFeO_3$ exhibit superior dispersion, enhanced thermal stability and suitable wetting ability in compare to unmodified one. Progressive growth in permittivity (especially in higher frequency range) and ferroelectric polarization is also observed in case of modified $BiFeO_3$ based nanocomposites. Magnetic property measurement confirms modification of nanoparticles reduces magnetization without any influence in its super paramagnetic nature. Magneto-dielectric measurements shows favorable coupling especially in case of nanocomposite made by using APTES modified $BiFeO_3$. Summing up all these valuable features, the possible applications of $BiFeO_3$/PVAc nanocomposite in the field of multiferroic coatings and adhesives can be envisaged. Still, comprehensive studies of magneto-electrical properties need to be investigated to stabilize practical device using such versatile nanocomposites.

Acknowledgements

References

[1] Catalan G., Scott J. F.: Physics and applications of bismuth ferrite. Advanced Materials, **21**, 2463–2485 (2009).
DOI: 10.1002/adma.200802849

[2] Eerenstein W., Mathur N. D., Scott J. F.: Multiferroic and magnetoelectric materials. Nature, **442**, 759–765 (2006).
DOI: 10.1038/nature05023

[3] Liu Y., Lv H., Lan X., Leng J., Du S.: Review of electro-active shape-memory polymer composite. Composites Science and Technology, **69**, 2064–2068 (2009).
DOI: 10.1016/j.compscitech.2008.08.016

[4] Tuboltsev V., Savin A., Sakamoto W., Hieno A., Yogo T., Räisänen J.: Spin-glass behavior of nanocrystalline multiferroic bismuth ferrite lead titanate. Journal of Materials Chemistry, **21**, 781–788 (2011).
DOI: 10.1039/c0jm02273j

[5] Zhang X., Lv J., Bourgeois L., Cui J., Wu Y., Wang H., Webley P. A.: Formation and photocatalytic properties of bismuth ferrite submicrocrystals with tunable morphologies. New Journal of Chemistry, **35**, 937–941 (2011).
DOI: 10.1039/c1nj00008j

[6] Dutta D. P., Jayakumar O. D., Tyagi A. K., Girija K. G., Pillai C. G. S., Sharma G.: Effect of doping on the morphology and multiferroic properties of $BiFeO_3$ nanorods. Nanoscale, **2**, 1149–1154 (2010).
DOI: 10.1039/C0NR00100G

[7] Wu J., Wang J., Xiao D., Zhu J.: Ferroelectric behavior in bismuth ferrite thin films of different thickness. ACS Applied Materials and Interfaces, **3**, 3261–3263 (2011).
DOI: 10.1021/am200801u

[8] Mohanty S., Choudhary R. N. P.: Dielectric and impedance characteristics of $KTaO_3$ modified $BiFeO_3$ multiferroics. Journal of Materials Science: Materials in Electronics, **25**, 1180–1187 (2014).
DOI: 10.1007/s10854-014-1706-8

[9] Martins P., Lanceros-Méndez S.: Polymer-based magnetoelectric materials. Advanced Functional Materials, **23**, 3371–3385 (2013).
DOI: 10.1002/adfm.201202780

[10] Casper M. D., Losego M. D., Maria J-P.: Optimizing phase and microstructure of chemical solution-deposited bismuth ferrite ($BiFeO_3$) thin films to reduce DC leakage. Journal of Materials Science, **48**, 1578–1584 (2012).
DOI: 10.1007/s10853-012-6914-0

[11] Lotey G. S., Verma N. K.: Magnetodielectric properties of rare earth metal-doped $BiFeO_3$ nanoparticles. Journal of Materials Science: Materials in Electronics, **24**, 3723–3729 (2013).
DOI: 10.1007/s10854-013-1309-9

[12] Wang H-C., Lin Y-H., Feng Y-N., Shen Y.: Photocatalytic behaviors observed in Ba and Mn doped $BiFeO_3$ nanofibers. Journal of Electroceramics, **31**, 271–274 (2013).
DOI: 10.1007/s10832-013-9818-8

[13] Liu Y., Zuo R.: Tunable morphology and optical absorption of bismuth ferrite synthesized by sol–gel–hydrothermal method. Journal of Materials Science: Materials in Electronics, **23**, 2276–2281 (2012).
DOI: 10.1007/s10854-012-0816-4

[14] Han J-T., Huang Y-H., Wu X-J., Wu C-L., Wei W., Peng B., Huang W., Goodenough J. B.: Tunable synthesis of bismuth ferrites with various morphologies. Advanced Materials, **18**, 2145–2148 (2006).
DOI: 10.1002/adma.200600072

[15] Ghosh S., Dasgupta S., Sen A., Sekhar Maiti H.: Low-temperature synthesis of nanosized bismuth ferrite by soft chemical route. Journal of the American Ceramic Society, **88**, 1349–1352 (2005).
DOI: 10.1111/j.1551-2916.2005.00306.x

[16] Sakar M., Balakumar S., Saravanan P., Jaisankar S. N.: Annealing temperature mediated physical properties of bismuth ferrite ($BiFeO_3$) nanostructures synthesized by a novel wet chemical method. Materials Research Bulletin, **48**, 2878–2885 (2013).
DOI: 10.1016/j.materresbull.2013.04.008

[17] Abramova V. V., Slesarev A., Sinitskii A.: Synthesis of high-quality inverse opals based on magnetic complex oxides: Yttrium iron garnet ($Y_3Fe_5O_{12}$) and bismuth ferrite ($BiFeO_3$). Journal of Materials Chemistry C, **1**, 2975–2982 (2013).
DOI: 10.1039/c3tc30335g

[18] Wu J., Mao S., Ye Z-G., Xie Z., Zheng L.: Room-temperature ferromagnetic/ferroelectric $BiFeO_3$ synthesized by a self-catalyzed fast reaction process. Journal of Materials Chemistry, **20**, 6512–6516 (2010).
DOI: 10.1039/c0jm00729c

[19] Chybczyńska K., Ławniczak P., Hilczer B., Łęska B., Pankiewicz R., Pietraszko A., Kępiński L., Kałuski T., Cieluch P., Matelski F., Andrzejewski B.: Synthesis and properties of bismuth ferrite multiferroic flowers. Journal of Materials Science, **49**, 2596–2604 (2013).
DOI: 10.1007/s10853-013-7957-6

[20] David M., Bharath K. R., Bhavani M.: Study of *Calotropis gigantea* R. Br. extracts on growth and survival dynamics of selected pathogenic microorganisms. International Journal of Biological Engineering, **1**, 1–5 (2012).
DOI: 10.5923/j.ijbe.20110101.01

[21] Kshirsager A., Purnima A., Ingawale D., Vyawahare N., Ingale K., Hadambar A.: Antioxidant and hepatoprotective activity of ethanolic extract of *Calotropis gigantea* against paracetamol induced liver damage in mice. Journal of Cell and Tissue Research, **9**, 1859–1864 (2009).

[22] Mittal A. K., Chisti Y., Banerjee U. C.: Synthesis of metallic nanoparticles using plant extracts. Biotechnology Advances, **31**, 346–356 (2013).
DOI: 10.1016/j.biotechadv.2013.01.003

[23] Gan P. P., Li S. F. Y.: Potential of plant as a biological factory to synthesize gold and silver nanoparticles and their applications. Reviews in Environmental Science and Bio/Technology, **11**, 169–206 (2012).
DOI: 10.1007/s11157-012-9278-7

[24] Wu J., Wang J., Xiao D., Zhu J.: Multiferroic and fatigue behavior of silicon-based bismuth ferrite sandwiched structure. Journal of Materials Chemistry, **21**, 7308–7313 (2011).
DOI: 10.1039/c0jm04026f

[25] Levkin P. A., Svec F., Fréchet J. M.: Porous polymer coatings: A versatile approach to superhydrophobic surfaces. Advanced Functional Materials, **19**, 1993–1998 (2009).
DOI: 10.1002/adfm.200801916

[26] Cao L., Jones A. K., Sikka V. K., Wu J., Gao D.: Anti-icing superhydrophobic coatings. Langmuir, **25**, 12444–12448 (2009).
DOI: 10.1021/la902882b

[27] Lim A. S., Melrose Z. R., Thostenson E. T., Chou T-W.: Damage sensing of adhesively-bonded hybrid composite/steel joints using carbon nanotubes. Composites Science and Technology, **71**, 1183–1189 (2011).
DOI: 10.1016/j.compscitech.2010.10.009

[28] Svoboda R., Pustková P., Málek J.: Structural relaxation of polyvinyl acetate (PVAc). Polymer, **49**, 3176–3185 (2008).
DOI: 10.1016/j.polymer.2008.05.002

[29] Kaboorani A., Riedl B.: Effects of adding nano-clay on performance of polyvinyl acetate (PVA) as a wood adhesive. Composites Part A: Applied Science and Manufacturing, **42**, 1031–1039 (2011).
DOI: 10.1016/j.compositesa.2011.04.007

[30] Rahaman M., Chaki T. K., Khastgir D.: Modeling of DC conductivity for ethylene vinyl acetate (EVA)/polyaniline conductive composites prepared through insitu polymerization of aniline in EVA matrix. Composites Science and Technology, **72**, 1575–1580 (2012).
DOI: 10.1016/j.compscitech.2012.06.005

[31] Gabower J. F.: Electromagnetic interference shield for electronic devices. U.S. Patent 5811050, USA (1998).

[32] Bhadra D., Masud M. G., Sarkar S., Sannigrahi J., De S. K., Chaudhuri B. K.: Synthesis of PVDF/$BiFeO_3$ nanocomposite and observation of enhanced electrical conductivity and low-loss dielectric permittivity at percolation threshold. Journal of Polymer Science Part B: Polymer Physics, **50**, 572–579 (2012).
DOI: 10.1002/polb.23041

[33] Jayakumar O. D., Mandal B. P., Majeed J., Lawes G., Naik R., Tyagi A. K.: Inorganic–organic multiferroic hybrid films of Fe_3O_4 and PVDF with significant magneto-dielectric coupling. Journal of Materials Chemistry C, **1**, 3710–3715 (2013).
DOI: 10.1039/c3tc30216d

[34] You S. J., Ai L., Li D., Huang H. M., Chen W. P., Liu W., Guo S. S., Zhao X. Z.: Enhanced electrical properties of composite nanostructures using $BiFeO_3$ nanotubes and ferroelectric copolymers. Materials Letters, **94**, 183–185 (2013).
DOI: 10.1016/j.matlet.2012.12.056

[35] Li Z., Shen Y., Yang C., Lei Y., Guan Y., Lin Y., Liu D., Nan C-W.: Significant enhancement in the visible light photocatalytic properties of $BiFeO_3$–graphene nanohybrids. Journal of Materials Chemistry A, **1**, 823–829 (2013).
DOI: 10.1039/c2ta00141a

[36] Rajasekharreddy P., Rani P. U., Sreedhar B.: Qualitative assessment of silver and gold nanoparticle synthesis in various plants: A photobiological approach. Journal of Nanoparticle Research, **12**, 1711–1721 (2010).
DOI: 10.1007/s11051-010-9894-5

[37] Babu S. A., Prabu H. G.: Synthesis of AgNPs using the extract of *Calotropis procera* flower at room temperature. Materials Letters, **65**, 1675–1677 (2011).
DOI: 10.1016/j.matlet.2011.02.071

[38] Martin L. W.: Engineering functionality in the multiferroic $BiFeO_3$ – Controlling chemistry to enable advanced applications. Dalton Transactions, **39**, 10813–10826 (2010).
DOI: 10.1039/c0dt00576b

[39] Lu A-H., Salabas E. L., Schüth F.: Magnetic nanoparticles: Synthesis, protection, functionalization, and application. Angewandte Chemie International Edition, **46**, 1222–1244 (2007).
DOI: 10.1002/anie.200602866

[40] Wang X., Zhang Y., Wu Z.: Magnetic and optical properties of multiferroic bismuth ferrite nanoparticles by tartaric acid-assisted sol–gel strategy. Materials Letters, **64**, 486–488 (2010).
DOI: 10.1016/j.matlet.2009.11.059

[41] Perejón A., Murafa N., Sánchez-Jiménez P. E., Criado J. M., Subrt J., Diánez M. J., Pérez-Maqueda L. A.: Direct mechanosynthesis of pure $BiFeO_3$ perovskite nanoparticles: Reaction mechanism. Journal of Materials Chemistry C, **1**, 3551–3562 (2013).
DOI: 10.1039/c3tc30446a

Dielectric properties of nanosilica/low-density polyethylene composites: The surface chemistry of nanoparticles and deep traps induced by nanoparticles

S. Ju[1,2], *M. Chen*[1], *H. Zhang*[1], *Z. Zhang*[1*]

[1]National Center for Nanoscience and Technology, China, 100190 Beijing, China
[2]University of Chinese Academy of Sciences, 100049 Beijing, China

Abstract. Four kinds of nanosilica particles with different surface modification were employed to fabricate low-density polyethylene (LDPE) composites using melt mixing and hot molding methods. The surface chemistry of modified nanosilica was analyzed by X-ray photoelectron spectroscopy. All silica nanoparticles were found to suppress the space charge injection and accumulation, increase the volume resistivity, decrease the permittivity and dielectric loss factor at low frequencies, and decrease the dielectric breakdown strength of the LDPE polymers. The modified nanoparticles, in general, showed better dielectric properties than the unmodified ones. It was found that the carrier mobility, calculated from *J–V* curves using the Mott-Gurney equation, was much lower for the nanocomposites than for the neat LDPE.

Keywords: nanocomposites, insulation, silica, polyethylene (PE), carrier mobility

1. Introduction

Polymer nanocomposites have recently drawn great attention of scientists [1–3]. Research has shown that nanofillers can improve the dielectric breakdown strength [4], enhance the voltage endurance [5], depress the space charge formation [6] and weaken the partial discharge degradation [7] of the pristine polymers more significantly than the micro-sized fillers. These improvements are of importance to electrical insulation applications and shed light on further advancement in dielectric materials [8].

The dispersion of nanoparticles in the polymer matrix [11, 12] and the property of the interface between nanoparticle and polymer are regarded as key factors affecting the electric insulating properties of nanocomposites [13, 14]. The interaction zone around nanoparticles can be considered as a 'quasi-conductive' region that partially overlaps in the nanocom-

posites, as proposed by Lewis [15]; they describe the interface as the pathway, charge would be transferred between a metal electrode and a dielectric phase, which can even control the conductive properties of the latter. Furthermore, another working hypothesis, so-called 'multi-core' model has also been proposed, which divides the 'interaction zone' of polymeric nanocomposites into three layers from particle surface to matrix [16, 17]; this model is used to illustrate several electrical performance of the polymer nanocomposites. Both the hypotheses believe that the charge dissipation in the interfacial regions could be the main reason to improve the dielectric breakdown strength and space charge suppression.

To improve the properties of the nanocomposites, the fine interface characteristics of nanoparticles as well as the homogeneous dispersion are needed. The common solution is to modify the nanoparti-

---

*Corresponding author, e-mail: zhong.zhang@nanoctr.cn

cles using coupling agents [18, 19]. Roy *et al.* [20] show that the vinylsilane modified nanosilicas offer XLPE a larger increase in the dielectric breakdown strength and double time to failure in voltage endurance strength, as compared to unmodified nano-silica filled materials. Using cold atmospheric-pressure plasma to modify nanosilica particles, Yan *et al.* [21] find that modified nanosilica/polymer nanocomposites show higher dielectric breakdown strength and extended endurance under a constant electrical stress, compared with the unmodified nanocomposites and neat polymer.

Besides the above, some other views have been proposed to explain why and how the nanoparticles affect the dielectric properties of polymer materials. Huang *et al.* [9] consider that inorganic particles may reduce the carrier mobility in the composite materials, thereby increasing their insulating properties. Takada *et al.* [10] propose a trapping model of 'induced dipole polarization'; it is proposed that the deep potential well induced by nanoparticles becomes trapping sites for carriers, which hinder the movement of carriers and avoid the space charge accumulation in the defect positions.

So far, a few researches have systematically studied the effects of different nanoparticle surface chemistry on the performances of composite materials. And this is the main goal of the present work. The dielectric breakdown strength, space charge, volume resistivity and permittivity of the SiO_2/LDPE nanocomposites were measured and compared with those of the neat LDPE. The carrier mobility was evaluated from the quadratic *J–V* curves of the samples using the Mott-Gurney equation. It is demonstrated that the space charge suppression and volume resistivity of the nanocomposites with surface-modified fillers were significantly improved, which is probably due to the lower carrier mobility in the nanocomposites.
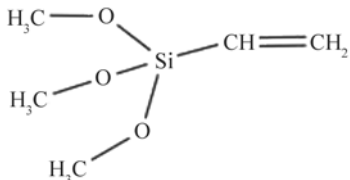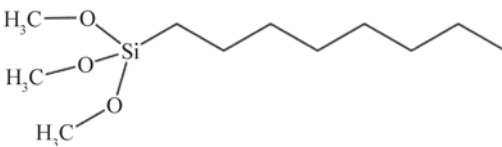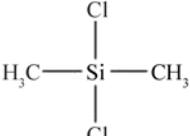
2. Experimental
2.1. Materials
LDPE (2220H) with density of 0.923 g/cm^3 and melt flow rate of 2.0 g/10 min was purchased from BASF-YPC Company (China). High purity fumed nanosilica (purity >99%) with the trademarks of A200, R312, R805 and R974 were obtained from Evonik Degussa AG (Germany). The nanosilicas A200 were un-surface-modified, while others were modified by vinyltrimethoxysilane, octyltrimethoxysilane and dimethyldichlorosilane, respectively, as stated by the supplier. The detailed information of the nanoparticles is listed in Table 1.

The different nanosilicas were mechanically mixed with LDPE granules at the processing temperature of 130°C using the HAAKE PolyLab mixer (HAAKE Rheomix600, Germany). Films of the neat LDPE and nanocomposites were prepared by a hot-press method at the temperature of 150°C and the pressure of

Table 1. Properties of the silica nanoparticles

Trademark	Average primary particle size [nm]	BET specific surface area [m^2/g]	Surface modifier	Chemical structure of surface modifier
A200	12	200±25	–	–
R312	12	210±30	vinyltrimethoxysilane	
R805	12	150±25	octyltrimethoxysilane	
R974	12	170±20	dimethyldichlorosilane	

20 MPa. The prepared films were placed in a vacuum oven at 95°C for 30 min, and then cooled down to room temperature to eliminate thermal history. To banish the remainder charge, the films were put between two polished copper plates in a vacuum oven at 80°C for 48 h short-circuiting.

2.2. Characterization

The surface chemical characteristics of the nano-silica were measured using X-ray photoelectron spectroscopy (XPS, Thermo Scientific ESCALAB 250Xi, USA) performed with Mg Kα radiation. C, O and Si were recorded.

The dispersion level of nanosilica in LDPE was observed using a field emission SEM (Hitachi S-4800, Japan) at 6 kV accelerating voltage. The composite samples for SEM were fractured in liquid nitrogen and sputtered with thin gold layer.

DC (direct-current) dielectric breakdown strength of samples was measured using a dielectric strength tester (HT-50, Guilin Electrical Equipment Scientific Research Institute, China). The sample (70±10 μm thick) was placed between 6 mm diameter copper cylindrical electrodes and tested at a voltage ramping rate of 500 and 2 kV/s until the sample failed. The whole setup was immersed in silicone oil. Weibull distribution was employed to fit the experimental data and determine the characteristic DC dielectric breakdown strength of the samples according to the IEEE Standard 930-2004 [22].

The space charge distribution was tested by pulsed electroacoustic measurement (PEA, Harbin university of science and technology, assembled by themselves) carried out under an electrical field of 40 kV/mm for 0.5 and 10 min at 25°C. The sensitivity of space charge was 0.6 μC/cm^3 with spatial resolution of 18~19 μm. During the measurement, the sample (300 μm thick×10 cm long×10 cm wide) was sandwiched between an aluminum electrode and a semi-conductive polymer electrode (both 7.5 cm in diameter).

Dielectric properties of the composite samples were measured by a high-resolution ALPHA analyzer (Novocontrol, Germany). The film samples (1 mm thick, 20 mm in diameter) were placed between two gold-coated stainless steel electrodes. The permittivity and loss tangent were measured in the frequency range from 10^{-2} to 10^6 Hz at 25°C.

Volume resistivity, polarization current and short-circuited current of the samples were measured
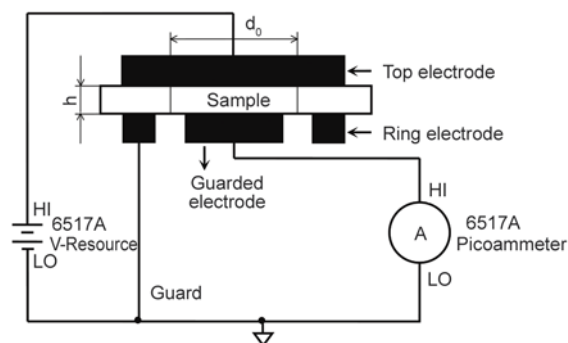

Figure 1. Experimental set-up for measuring volume resistivity and polarization current of samples

with a Keithley electrometer model 6517A. A standard three-electrode system was used, as illustrated in Figure 1, where the conductive rubber pad diameter (d_0) is 54 mm and the thick of sample (h) is 0.1 mm. The volume resistivity was tested at a DC voltage of 50 V and the polarization current at 1000 V. The short-circuit current was obtained by letting the upper and lower surfaces of the sample short circuit after applying 1000 V for five minutes [7].

3. Results and discussion
3.1. Characterization of the particle surface and dispersion level

Figure 2 shows the surface chemistry of four types of nanosilica, i.e. A200, R312, R805, R974, using XPS. The signal ratio of C (1s) to O (1s) is 0.76 for unmodified nanoparticles (A200). The ratios are relatively higher for the modified ones, which are 1.86, 1.69 and 3.60 for R312, R805 and R974, respectively. The high intensity ratio of carbon signal indicates the presence of organic species for surface modified silica [23]. Note that the signal of C(1s) for A200 is probably due to the presence of carbon impurity in these fillers, such as carbon dioxide, according to the literature [25]. The shift of O (1s) signals (Figure 2b) and Si (2p) signals (Figure 2c) of modified silica (R312, R805 and R974, respectively) toward lower binding energy indicates the silane coupling reaction has done on the surface of silica [24]. It can be seen from Figure 2a that as the intensity of carbon signals increases, the intensity of silicon and oxygen signals reduce accordingly, indicating the coating of silane on the silica surface, which may offer nice interfacial properties.

The SEM micrographs in Figure 3 show the dispersion levels of nanosilicas in LDPE on the fracture surface of nanocomposites. All the nanosilicas (A200, R312, R805, R974) are dispersed well with no big
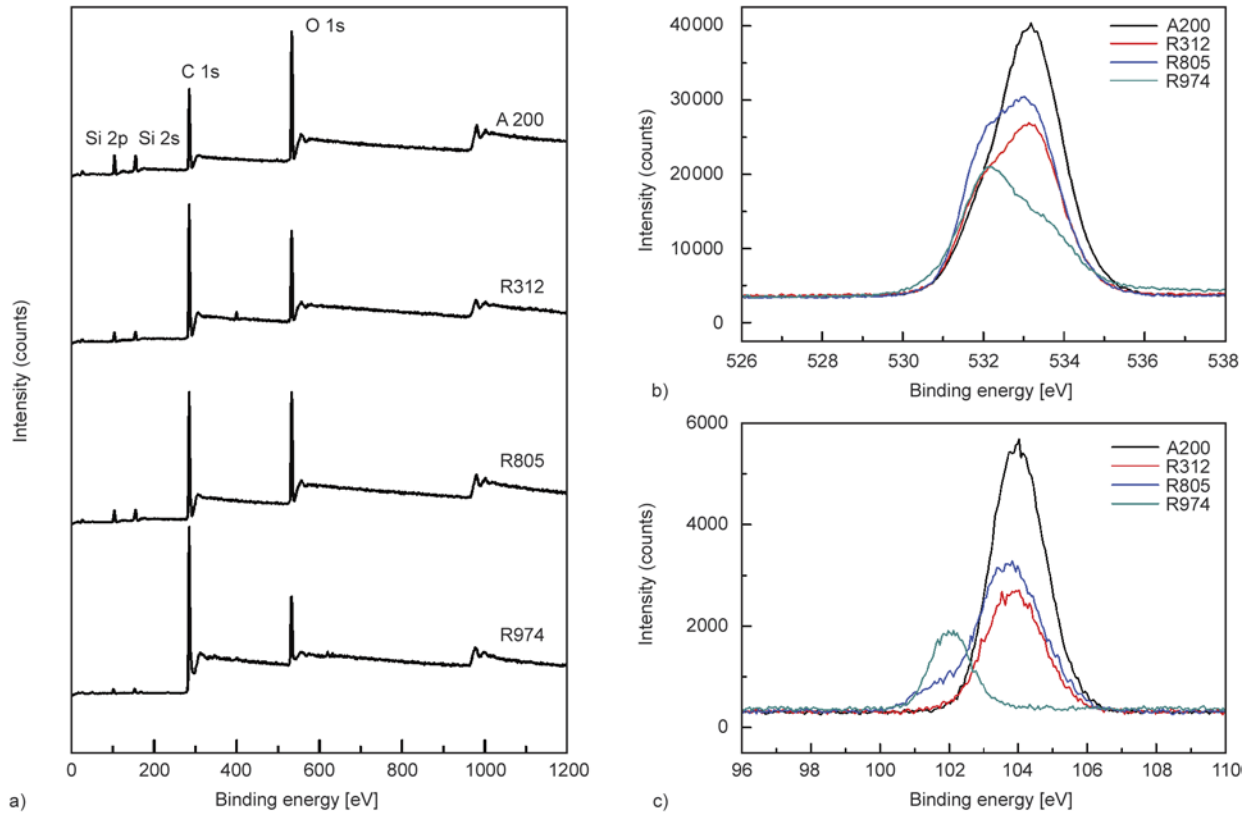
Figure 2. XPS spectra of (a) the silica nanoparticles used and comparison of four types of silica on (b) oxygen signals and (c) silicon signals

agglomerates in the nanocomposites. The arrows in Figure 3 indicate some cavitations between nanoparticles and polymer matrix, suggesting the relatively weak interfacial adhesion. This situation seems more obvious for the unmodified nanoparticles (A200) than the other modified nanoparticles (R312, R805, R974). This means the chemical surface modification does improve the interfacial adhesion.

3.2. Dielectric breakdown strength

The dielectric breakdown strength of the nanocomposites is analyzed within the framework of Weibull statistics. The Weibull parameters, α and β (representing the characteristic dielectric breakdown strength and shape parameter), are shown in the insert table in Figure 4. α is found to be strongly affected by the filler modification in the nanocomposite samples and the voltage ramping rate [5]. Addition of nanosilica particles reduce α values of the LDPE polymers, which is likely due to the more defects in the composite samples that result in charge accumulation and partial discharge. The defects are formed due to the relatively weak interface, voids as well as the larger aggregates. Comparatively, the modified nanoparticles show the relatively higher α values than the

unmodified ones, owing to the improved interface, good dispersion level and smaller aggregates [26]. In addition, α values of the samples increase as the voltage ramping rate increases from 500 V/s to 2 kV/s due to the viscoelastic behavior of LDPE polymer.

3.3. Space charge

Figure 5 shows the PEA curves of the neat LDPE and nanocomposite samples (silica content = 5 wt%) tested at an applied electric field of 40 kV/mm. The curves show the evaluation of space charges in the samples. After applying the electric field for 0.5 min, the space charges are found to accumulate near the electrodes. After applying the electric field for 10 min, the space charges obviously diffuse to the middle of the sample, as indicated by black arrows in Figure 5 [27]. Nevertheless, the space charge injection has been significantly inhibited for the modified silica nanocomposites. The space charge accumulation in the middle of the sample is reduced, while only a small amount of charge is found near the electrodes. Interestingly, the heterocharges are found near the anode of R974/LDPE, as shown by the red arrow in Figure 5, which may originate from the chemistry nature of the silica surface. The outer elec-
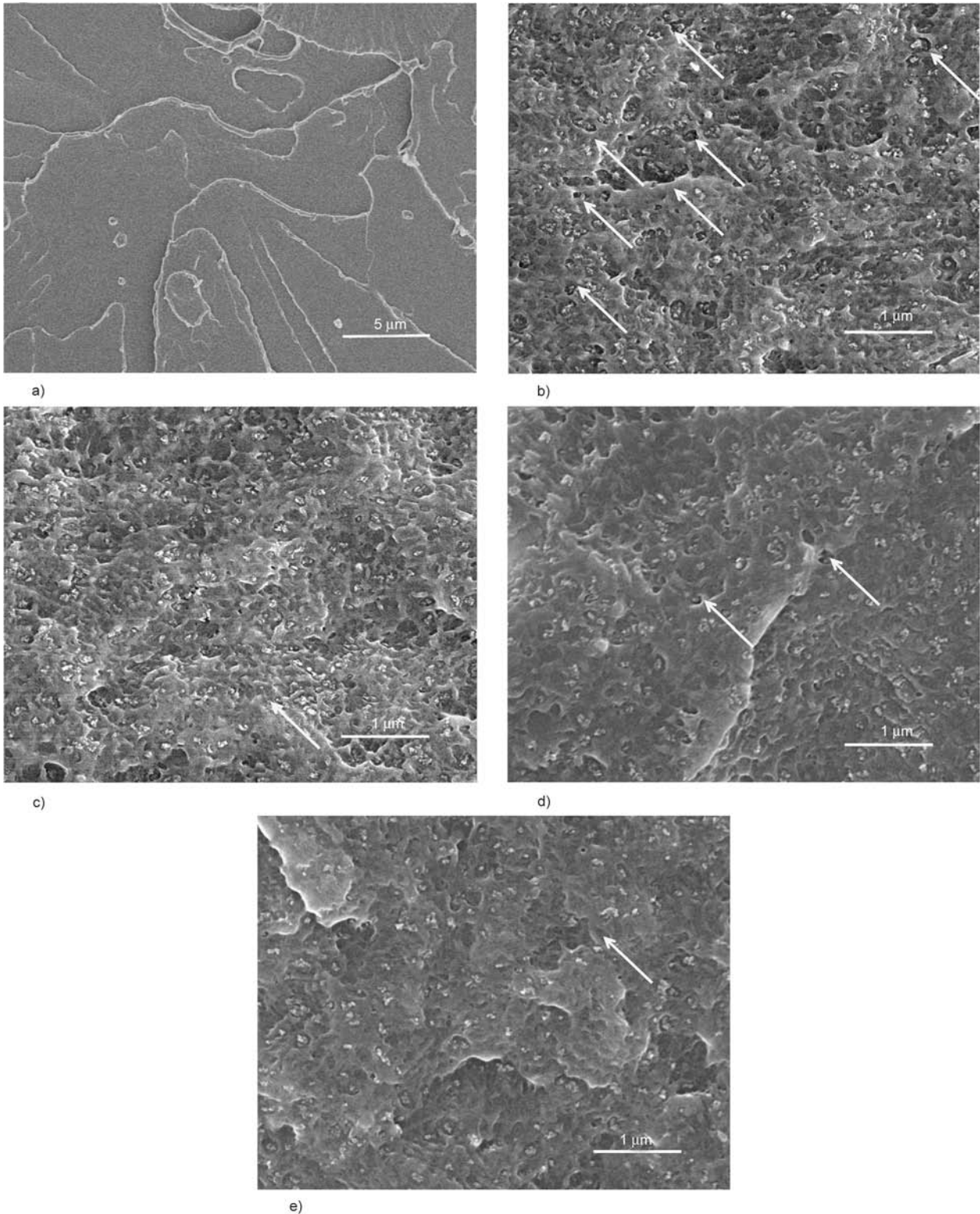
Figure 3. SEM micrographs of the fracture surfaces of composites filled with 5 wt% silica nanoparticles: (a) LDPE, (b) A200/LDPE, (c) R312/LDPE, (d) R805/LDPE, and (e) R974/LDPE

trons of chlorine originating from dimethyldichloro-silane coated on R974 are far from the nucleus. It is susceptible to deform and polarize due to the applied electric field. The polarized reactions are particularly likely to occur at the anode. Changes in the distribution of space charge caused by surface modification are also reported by Huang *et al.* [9] and Ma *et al.* [28]. As the space charge is the initiator of aging, it is very meaningful to do the filler surface modification to improve its interfacial adhesion and dispersion in the matrix, in order to suppress space charge injection.
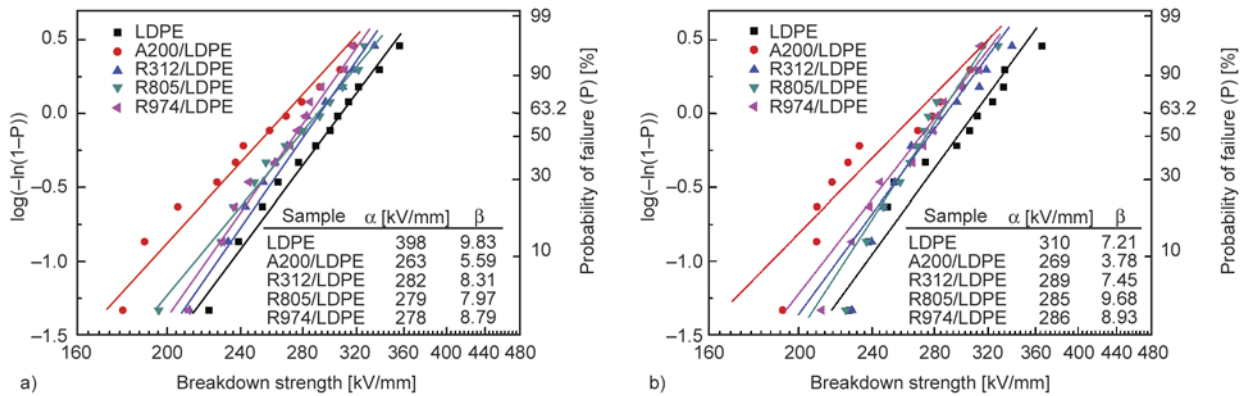
Figure 4. Weibull probability plots of DC breakdown strength of LDPE and its nanocomposite films at voltage ramping rate of (a) 500 V/s and (b) 2 kV/s
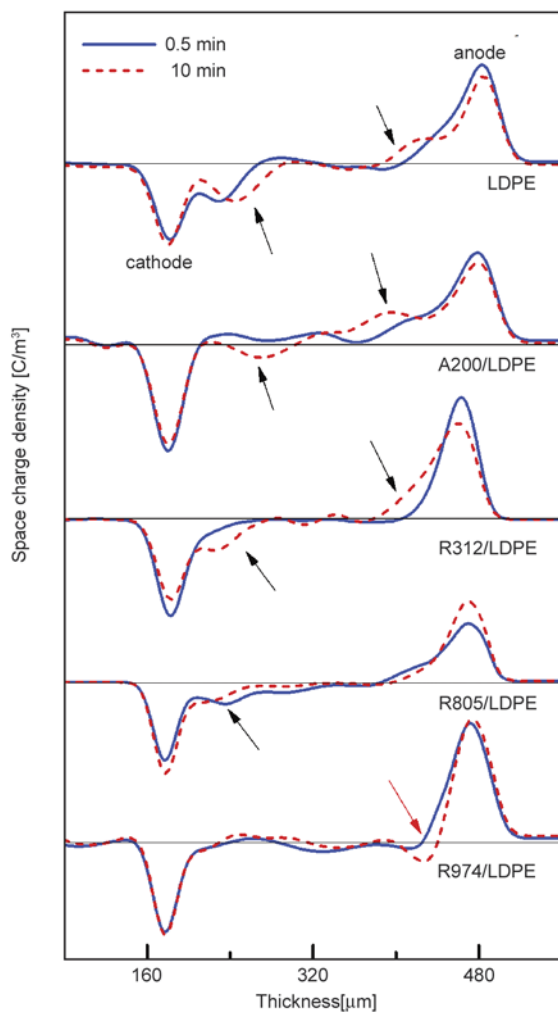

Figure 5. Space charge distribution of neat LDPE and its nanocomposites with the thickness of 300 μm

3.4. Dielectric properties

Figure 6 shows the dielectric constant and loss tangent (tan δ) as a function of frequency at 25°C for the neat LDPE and nanocomposites. At low frequencies the dielectric constant of LDPE increases strongly with decreasing frequencies up to very high values

(Figure 6a) which cannot be explained by molecular relaxation processes. Such a behavior is a clear sign of electrode polarization, which originates from the blocking of charge carriers at the sample/electrode interface [29]. Medjdoub *et al.* [30] show similar results of LDPE appears at a low frequency. However, they consider this reflects conductivity effects due to free charge motion within the material. Moreover, at low frequencies the dipoles have sufficient time to align with the field before it changes direction giving rise to high permittivity. At high frequencies the dipoles do not have time to align before the field changes direction and the permittivity is lower [31]. The addition of A200 make permittivity of LDPE increase in the 1–1000 Hz range, but decrease in the 10 000–100 000 Hz range, while the permittivities of R312/LDPE, R805/LDPE and R974/LDPE all reduce to different extents (the insert of Figure 6a), indicating that the charge carriers movement was inhibited in the functionalized nanocomposites [32]. Moreover, the slope of the dielectric loss of functionalized nanocomposites is lower than A200/LDPE (Figure 6b), suggesting that the conducting sheath present in the case of functionalized nanocomposites is less-conducting according to the O'Konski's model [33]. By this model, an induced polarization occurs at the polar ends of the particle by the applied electric field. Then charge carriers are efficiently transferred around the interface and become the conducting sheath [30]. This will lead to a permittivity higher than the particle itself. It is interesting to find that there is a relaxation peak in the range of 1000–100 000 Hz in A200/LDPE, indicating changes of the LDPE molecular structure. A200 disrupt the original crystallization process of LDPE, resulting in more free volume, while the poor inter-
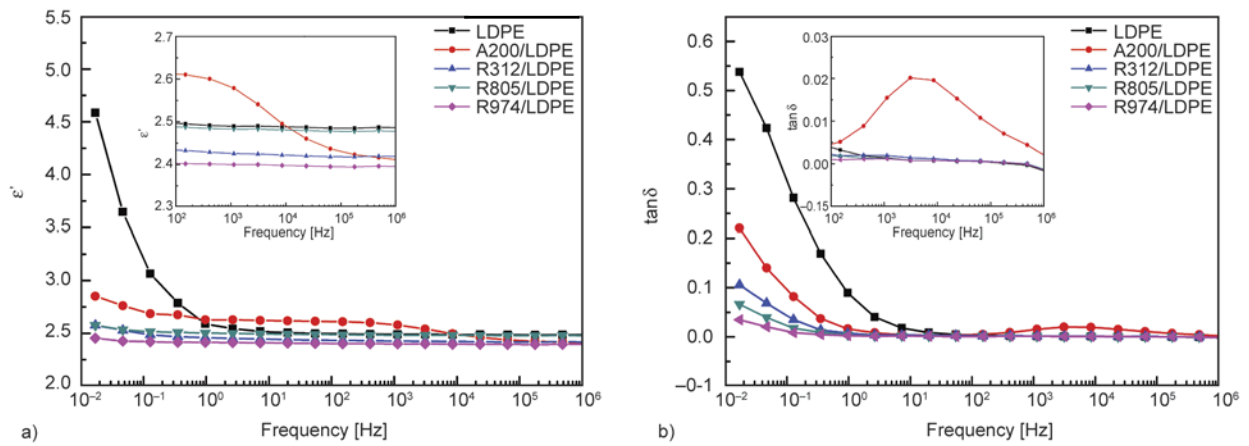
Figure 6. Dielectric constant (a) and loss tangent (b) for neat LDPE and the nanocomposites

face also introduces more defects, the relaxation of the polymer occurs [34].

3.5. Polarization current and volume resistivity

Figure 7 shows polarization currents and short-circuit currents measured for 5 min. Both and short-circuit currents decrease exponentially with time, and subsequently reach an equilibrium value. LDPE needs 150 s to reach the equilibrium value of polarization currents, while only 20 s for nanocomposite (Figure 7a), and the initial value, equilibrium value of polarization current and short-circuit current of LDPE are much larger than those of nanocomposite. It could be indicated that a large amount of charges inject into and go through the LDPE. However, the nanosilica can inhibit the charges to inject into the interior of nanocomposite, and make most of charges gather on the surface of the sample [35]. It seems that the addition of nanosilica decrease the carrier mobility of nanocomposite. Meanwhile, the volume resistivity are 3.74×10^{17}, 7.53×10^{17}, 6.88×10^{17}, $7.12\times10^{17}\,\Omega\cdot$cm for A200/LDPE, R312/LDPE,

Figure 8. Volume resistivity at 20°C of neat LDPE and its nanocomposites

R805/LDPE, R974/LDPE respectively, about one order of magnitude larger than that of LDPE ($5.65\times10^{16}\,\Omega\cdot$cm) as shown in Figure 8 [36].

3.6. Carrier mobility

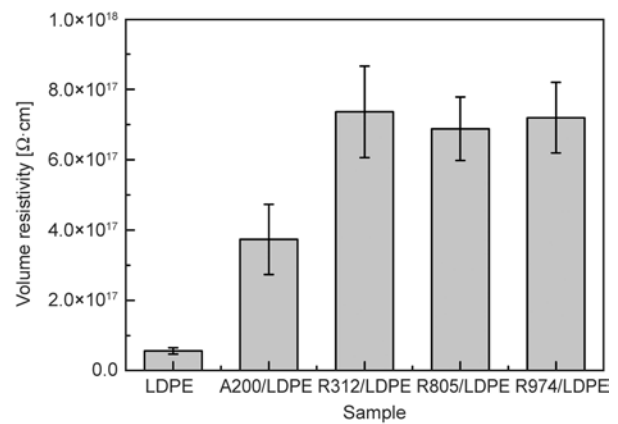The current density-voltage (*J–V*) curves are obtained from the equilibrium value of polarization current at different voltages (Figure 9). It is consistent with
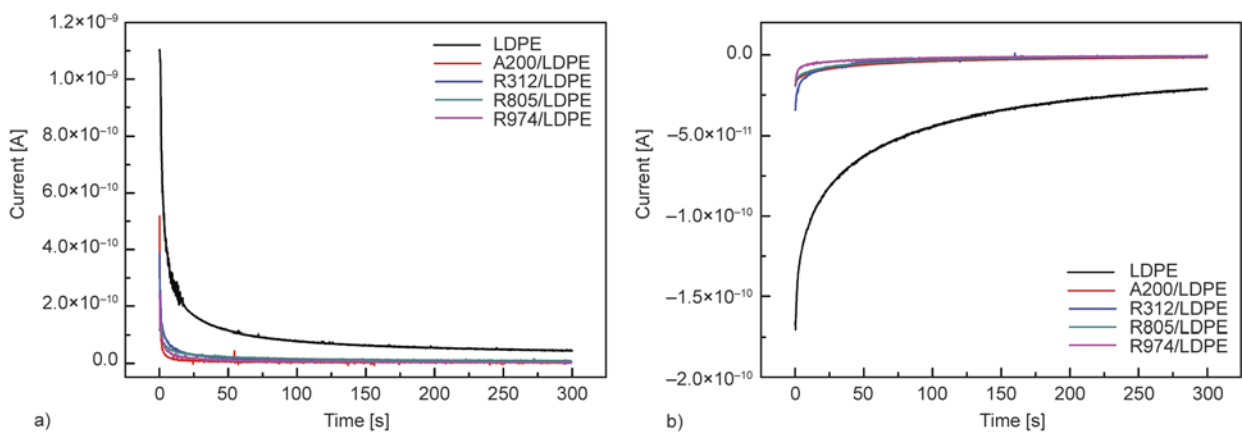

Figure 7. Polarization currents measured (a) at 1000 V and (b) in a short-circuit

the well-known Mott and Gurney equation [37]. At low applied voltages the *J–V* characteristics may follow Ohm's law (Equation (1)):

$$J = qp_0\mu_p\frac{V}{d} \qquad (1)$$

where p_0 is the density of thermally generated free carriers inside the sample, μ_p is the carrier mobility and d is the thickness of the sample. So we can use the slope of the linear fit, $k_l = qp_0\mu_p/d$, to calculate the volume resistivity of the materials. The results are shown in the Table 2, which are consistent with the experimental results.

Due to the increased space charge, quadratic relationship of *J–V* curves fitting are obtained (Figure 9) at high applied voltages as shown by Equation (2):

$$J = \frac{9}{8}\varepsilon_r\varepsilon_0\mu_p\frac{V^2}{d^3} \qquad (2)$$

where ε_r is the relative permittivity of the material, and $\varepsilon_0 = 8.854\times10^{-12}$ F/m, is the permittivity of vacuum. Then the carrier mobility μ_0 are calculated from the fitting constants *k*, where Equation (3):

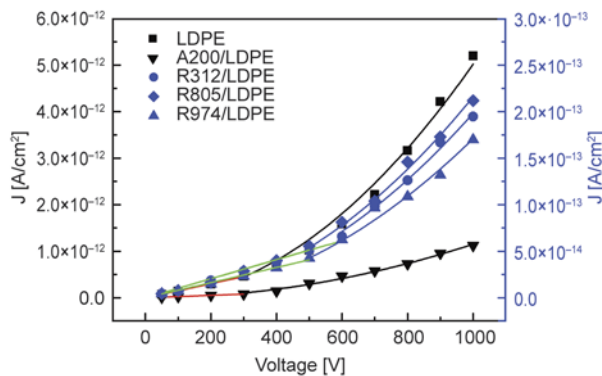$$k = \frac{9\varepsilon_r\varepsilon_0\mu_p}{8d^3} \qquad (3)$$

Figure 9. Current density-voltage (*J–V*) curves from the equilibrium value of polarization current at different voltages

Table 2. The carrier mobility calculated by the fitting constants

Sample	k	Carrier mobility μ_p [cm²/(V·s)]	k_l	Volume resistivity ρ [Ω·cm]
LDPE	5.02×10^{-18}	6.97×10^{-12}	1.52×10^{-15}	6.60×10^{16}
A200/LDPE	1.16×10^{-18}	1.61×10^{-12}	2.64×10^{-16}	3.81×10^{17}
R312/LDPE	1.98×10^{-19}	2.75×10^{-13}	1.02×10^{-16}	9.79×10^{17}
R805/LDPE	2.16×10^{-19}	3.00×10^{-13}	1.03×10^{-16}	9.74×10^{17}
R974/LDPE	1.71×10^{-19}	2.37×10^{-13}	8.15×10^{-17}	1.23×10^{18}

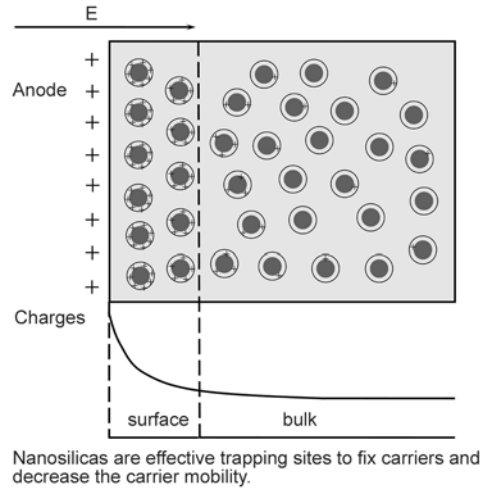Nanosilicas are effective trapping sites to fix carriers and decrease the carrier mobility.

Figure 10. Schematic of the deep-trap hypothesis at high voltage in the insulating nanocomposites

As seen in Table 2, the carrier mobility of LDPE calculated by the above equations is 6.97×10^{-12} cm²/(V·s), which is comparable to published values [38, 39]. The addition of silica decreases the carrier mobility of composites, especially the silica modified by silane coupling agent, about an order of magnitude.

As the trapping model of 'induced dipole polarization' proposed by Takada, the potential well induced by nanoparticles is much deeper than that induced by chemical defects [10]. It makes the nanosilica become effective trapping site to fix carriers and decrease the carrier mobility. As illustrated in Figure 10, charges injected from electrodes generate in the deep trap induced by the nanosilica after electric voltage applied. The charges are difficult to move and accumulate near the electrodes to produce an additional electric potential reversed to the applied voltage. Therefore the potential difference near the electrode becomes small. It inhibits the dissociation of small molecule and prevents further injection of the charges. Therefore, the space charge inside the sample is reduced.

4. Conclusions

Bare silica (A200) and silane modified nanosilica (R312, R805 and R974) were incorporated to LDPE using a melt-mixing approach, to improve the dielectric properties of silica/LDPE nanocomposites. SEM revealed that modified nanosilicas were dispersed more evenly in the matrix than the unmodified ones. All nanosilicas lowered the space charge injection and accumulation, increased the volume resistivity, but decreased the dielectric breakdown strength of the

LDPE. The surface modified silica/LDPE nanocomposites showed relatively higher dielectric breakdown strength, than the unmodified ones. It was found from polarization currents and short-circuit currents analysis that nanosilica prevented further injection of charges from electrodes into samples. The carrier mobility of modified silica/LDPE nanocomposites calculated from *J–V* curves was about 5 times lower than those of unmodified ones, more than one order of magnitude lower than neat LDPE. The results obtained confirmed that the surface modification of nanoparticles was very necessary for improving the insulating properties of LDPE polymer.

Acknowledgements

References

[1] Hussain F., Hojjati M., Okamoto M., Gorga R. E.: Review article: Polymer-matrix nanocomposites, processing, manufacturing, and application: An overview. Journal of Composite Materials, **40**, 1511–1575 (2006).
DOI: 10.1177/0021998306067321

[2] Pyun J., Matyjaszewski K.: Synthesis of nanocomposite organic/inorganic hybrid materials using controlled/ 'living' radical polymerization. Chemistry of Materials, **13**, 3436–3448 (2001).
DOI: 10.1021/cm011065j

[3] Sayari A., Hamoudi S.: Periodic mesoporous silica-based organic–inorganic nanocomposite materials. Chemistry of Materials, **13**, 3151–3168 (2001).
DOI: 10.1021/cm011039l

[4] Nelson J. K., Hu Y., Thiticharoenpong J.: Electrical properties of TiO$_2$ nanocomposites. in '2003 Annual Report Conference on Electrical Insulation and Dielectric Phenomena. Albuquerque, USA' 719–722 (2003).
DOI: 10.1109/ceidp.2003.1254955

[5] Roy M., Nelson J. K., MacCrone R. K., Schadler L. S., Reed C. W., Keefe R., Zenger W.: Polymer nanocomposite dielectrics-the role of the interface. IEEE Transactions on Dielectrics and Electrical Insulation, **12**, 629–643 (2005).
DOI: 10.1109/tdei.2005.1511089

[6] Smith R. C., Liang C., Landry M., Nelson J. K., Schadler L. S.: The mechanisms leading to the useful electrical properties of polymer nanodielectrics. IEEE Transactions on Dielectrics and Electrical Insulation, **15**, 187–196 (2008).
DOI: 10.1109/t-dei.2008.4446750

[7] Calebrese C., Le H., Schadler L. S., Nelson J. K.: A review on the importance of nanocomposite processing to enhance electrical insulation. IEEE Transactions on Dielectrics and Electrical Insulation, **18**, 938–945 (2011).
DOI: 10.1109/tdei.2011.5976079

[8] Tanaka T., Montanari G. C., Mulhaupt R.: Polymer nanocomposites as dielectrics and electrical insulation-perspectives for processing technologies, material characterization and future applications. IEEE Transactions on Dielectrics and Electrical Insulation, **11**, 763–784 (2004).
DOI: 10.1109/tdei.2004.1349782

[9] Huang X., Jiang P., Yin Y.: Nanoparticle surface modification induced space charge suppression in linear low density polyethylene. Applied Physics Letters, **95**, 242905 (2009).
DOI: 10.1063/1.3275732

[10] Takada T., Hayase Y., Tanaka Y., Okamoto T.: Space charge trapping in electrical potential well caused by permanent and induced dipoles for LDPE/MgO nanocomposite. IEEE Transactions on Dielectrics and Electrical Insulation, **15**, 152–160 (2008).
DOI: 10.1109/t-dei.2008.4446746

[11] Yin Y., Chen J., Yang J., Xiao D., Tu D., Yin R., Qian H.: Effect of space charge in nanocomposite of LDPE/ TiO$_2$. in 'Proceedings of the 7th International Conference on Properties and Applications of Dielectric Materials. Nagoya, Japan' Vol. 3, 913–916 (2003).
DOI: 10.1109/ICPADM.2003.1218570

[12] Yang J-M., Wang X., Zheng C-J., Zhao H., Lei Q-Q.: DC conduction properties of SiO$_2$/LDPE Nanocomposite. in '10th IEEE International Conference on the Properties and Applications of Dielectric Materials (ICPADM), Bangalore, India' 1–4 (2012).
DOI: 10.1109/ICPADM.2012.6318950

[13] Wang W., Li S., Tang F., Li J.: Characteristics on breakdown performance of polyethylene/silica dioxide nanocomposites. in '2012 Annual Report Conference on Electrical Insulation and Dielectric Phenomena. Montreal, Canada' 521–524 (2012).
DOI: 10.1109/CEIDP.2012.6378834

[14] Schmidt D., Shah D., Giannelis E. P.: New advances in polymer/layered silicate nanocomposites. Current Opinion in Solid State and Materials Science, **6**, 205–212 (2002).
DOI: 10.1016/s1359-0286(02)00049-9

[15] Lewis T. J.: Nanometric dielectrics. IEEE Transactions on Dielectrics and Electrical Insulation, **1**, 812–825 (1994).
DOI: 10.1109/94.326653

[16] Tanaka T.: Dielectric nanocomposites with insulating properties. IEEE Transactions on Dielectrics and Electrical Insulation, **12**, 914–928 (2005).
DOI: 10.1109/tdei.2005.1522186

[17] Tanaka T., Kozako M., Fuse N., Ohki Y.: Proposal of a multi-core model for polymer nanocomposite dielectrics. IEEE Transactions on Dielectrics and Electrical Insulation, **12**, 669–681 (2005).
DOI: 10.1109/tdei.2005.1511092

[18] Geng Y., Liu M. Y., Li J., Shi X. M., Kim J. K.: Effects of surfactant treatment on mechanical and electrical properties of CNT/epoxy nanocomposites. Composites Part A: Applied Science and Manufacturing, **39**, 1876–1883 (2008).
DOI: 10.1016/j.compositesa.2008.09.009

[19] Siqueira G., Bras J., Dufresne A.: Cellulose whiskers versus microfibrils: Influence of the nature of the nanoparticle and its surface functionalization on the thermal and mechanical properties of nanocomposites. Biomacromolecules, **10**, 425–432 (2009).
DOI: 10.1021/bm801193d

[20] Roy M., Nelson J. K., MacCrone R. K., Schadler L. S.: Candidate mechanisms controlling the electrical characteristics of silica/XLPE nanodielectrics. Journal of Materials Science, **42**, 3789–3799 (2007).
DOI: 10.1007/s10853-006-0413-0

[21] Yan W., Han Z. J., Phung B. T., Ostrikov K.: Nanosilicas treated by cold atmospheric-pressure plasmas improve the dielectric performance of organic-inorganic nanocomposites. Acs Applied Materials and Interfaces, **4**, 2637–2642 (2012).
DOI: 10.1021/am300300f

[22] Huang X., Zheng Y., Jiang P., Yin Y.: Influence of nanoparticle surface treatment on the electrical properties of cycloaliphatic epoxy nanocomposites. IEEE Transactions on Dielectrics and Electrical Insulation, **17**, 635–643 (2010).
DOI: 10.1109/tdei.2010.5448121

[23] Laruelle G., Parvole J., Francois J., Billon L.: Block copolymer grafted-silica particles: A core/double shell hybrid inorganic/organic material. Polymer, **45**, 5013–5020 (2004).
DOI: 10.1016/j.polymer.2004.05.030

[24] Brito L., Fiolhais M.: Energetics of charge distributions. European Journal of Physics, **23**, 427–432 (2002).
DOI: 10.1088/0143-0807/23/4/306

[25] Ray S., Bhowmick A. K.: Novel electron beam-modified surface-coated silica fillers: Physical and chemical characteristics. Journal of Applied Polymer Science, **83**, 2255–2268 (2002).
DOI: 10.1002/app.10240

[26] Wang Z., Iizuka T., Kozako M., Ohki Y., Tanaka T.: Development of epoxy/BN composites with high thermal conductivity and sufficient dielectric breakdown strength part II-breakdown strength. IEEE Transactions on Dielectrics and Electrical Insulation, **18**, 1973–1983 (2011).
DOI: 10.1109/tdei.2011.6118635

[27] Nelson J. K., Fothergill J. C.: Internal charge behaviour of nanocomposites. Nanotechnology, **15**, 586–595 (2004).
DOI: 10.1088/0957-4484/15/5/032

[28] Ma D., Hugener T. A., Siegel R. W., Christerson A., Mårtensson E., Önneby C., Schadler L. S.: Influence of nanoparticle surface modification on the electrical behaviour of polyethylene nanocomposites. Nanotechnology, **16**, 724–731 (2005).
DOI: 10.1088/0957-4484/16/6/016

[29] Kremer F., Schönhals A.: Broadband dielectric spectroscopy. Springer, Berlin (2003).

[30] Medjdoub A., Boubakeur A., Lebey T.: Dielectric spectroscopy analysis behavior of low density polyethylene. in '2008 IEEE Conference on Electrical Insulation and Dielectric Phenomena, Québec, Canada' 517–520 (2008).
DOI: 10.1109/CEIDP.2008.4772907

[31] Dang Z-M., Zhang Y-H., Tjong S-C.: Dependence of dielectric behavior on the physical property of fillers in the polymer-matrix composites. Synthetic Metals, **146**, 79–84 (2004).
DOI: 10.1016/j.synthmet.2004.06.011

[32] Takala M., Ranta H., Nevalainen P., Pakonen P., Pelto J., Karttunen M., Virtanen S., Koivu V., Pettersson M., Sonerud B., Kannus K.: Dielectric properties and partial discharge endurance of polypropylene-silica nanocomposite. Dielectrics and Electrical Insulation, IEEE Transactions on Dielectrics and Electrical Insulation, **17**, 1259–1267 (2010).
DOI: 10.1109/tdei.2010.5539698

[33] O'Konski C. T.: Electric properties of macromolecules. V. Theory of ionic polarization in polyelectrolytes. The Journal of Physical Chemistry, **64**, 605–619 (1960).
DOI: 10.1021/j100834a023

[34] Nanda M., Chaudhary R. N. P., Tripathy D. K.: Dielectric relaxation of conductive carbon black reinforced chlorosulfonated polyethylene vulcanizates. Polymer Composites, **31**, 152–162 (2010).
DOI: 10.1002/pc.20779

[35] Nelson J. K., Hu Y.: Nanocomposite dielectrics – Properties and implications. Journal of Physics D: Applied Physics, **38**, 213–222 (2005).
DOI: 10.1088/0022-3727/38/2/005

[36] Leroux C., Mur P., Rochat N., Rouchon D., Truche R., Reimbold G., Ghibaudo G.: Characterization and modeling of nanometric SiO_2 dielectrics. Microelectronic Engineering, **72**, 121–124 (2004).
DOI: 10.1016/j.mee.2003.12.049

[37] Kao K. C., Hwang W.: Electrical transport in solids with particular reference to organic semiconductors. Taylor and Francis, London (1981).

[38] Meunier M., Quirke N., Aslanides A.: Molecular modeling of electron traps in polymer insulators: Chemical defects and impurities. Journal of Chemical Physics, **115**, 2876–2881 (2001).
DOI: 10.1063/1.1385160

[39] Anta J. A., Marcelli G., Meunier M., Quirke N.: Models of electron trapping and transport in polyethylene: Current–voltage characteristics. Journal of Applied Physics, **92**, 1002–1008 (2002).
DOI: 10.1063/1.1489714

Barium titanate/polyester resin nanocomposites: Development, structure-properties relationship and energy storage capability

I. A. Asimakopoulos[1], G. C. Psarras[2], L. Zoumpoulakis[1]*

[1]National Technical University of Athens, School of Chemical Engineering, Section III 'Materials Science and Engineering', Laboratory Unit 'Advanced and Composite Materials', 9-Heroon Polytechniou str., Zografou Campus, Athens 157 73, Greece

[2]Department of Materials Science, School of Natural Sciences, University of Patras, Patras 26505, Greece

Abstract. Nanocomposite materials based on two different types of polyester matrix (a commercial type and a laboratory produced one) with embedded barium titanate nano-particles were developed and characterized. Structural and morphological characteristics of the produced composite specimens were studied via X-ray diffraction, Fourier transformation infra red spectroscopy, and scanning electron microscopy. Thermal, mechanical and electrical performance was examined via differential scanning calorimetry, bending and shear strength tests, and broadband dielectric spectroscopy, respectively. Mechanical strength appears to reduce with the increase of filler content. Commercial polyester's composites exhibit brittle behaviour, while laboratory polyester's composites exhibit an elastomeric performance. Dielectric data reveal the presence of four relaxation processes, which are attributed to motion of small parts of the polymer chain (γ-mode), re-arrangement of polar side groups (β-mode), glass to rubber transition of the polymer matrix (α-mode) and Interfacial Polarization between the systems' constituents. Finally, the energy storing efficiency of the systems was examined by calculating the density of energy.

Keywords: nanocomposites, polyester resin, barium titanate ferroelectric crystal, mechanical properties, structural characterization

1. Introduction

The presence of $BaTiO_3$ nano-particles in this type of polyester polymer composites adds to the materials' system performance piezoelectric, ferroelectric and pyroelectric properties. These properties can be exploited in developing 'intelligent' or 'smart' materials. Intelligence, at its most basic level in materials is characterized by three fundamental functions associated with sensing, actuation and control [1]. These fundamental functions are also related with energy conversion mechanisms and information-transfer mechanisms which involve essential concepts at the atomic and molecular levels [2]. The applications of smart materials and structures are expected to be widely diverse, ranging from bio-medical to energy storing devices. A common denominator for the deployment of the most sophisticated class of materials systems, featuring sensors, actuators and microprocessors, will probably be the unstructured environment in which a system should operate properly. Thus the uncertainty associated with the influence of the relevant external stimuli, which govern the system's response relative to the prescribed design, will largely dictate the deployment of smart materials and structures [2, 3].

An outstanding position in the group of electroceramics is given to composite materials based on barium titanate. Barium titanate is a wide band gap semiconductive ferroelectric material with perovskite structure which has been of practical importance for over 60 years due to its specific electrical properties. Barium titanate's great significance is expressed in its applications, which include ceramic capacitors, PTCR thermistors (positive temperature coefficient resistors/thermistors or posistors), piezoelectric sensors, optoelectronic devices, transducers, actuators etc. [4–10]. Furthermore, it is being applied as a capacitive material in dynamic random access memories (DRAM) in integrated circuits. DRAM applications require both high dielectric constant and good insulating properties [10]. Semiconductor memories such as dynamic random access memories (DRAM's) and static random access memories (SRAM's) currently dominate the market. However, the disadvantage of these memories is that they are volatile, i.e. the stored information is lost when the power fails. The non-volatile memories available at this time include complementary metal oxide semiconductors (CMOS) with battery backup and electrically erasable read only memories (EEPROM's). These non-volatile memories are very expensive. The main advantages offered by ferroelectric random access memories (FRAM's) include non-volatility and radiation hardened compatibility with CMOS and GaAs circuitry, high speed (30ns cycle time for read/erase/rewrite) and high density (4 $(\mu m)^2$/cell size) [11].

Up to now, the most important utility of $BaTiO_3$/polymer composites is based on their dielectric properties, because of barium titanate's high dielectric permittivity value (high-K material) [12]. Nevertheless serious drawback for this kind of composites is their poor mechanical properties [13]. The latter is related to the brittle nature of the ceramic filler, and to the possibility that distributed ceramic particles could act as stress raisers. Ideally, mechanically robust and processable at ambient temperature, tiny high-k materials could be incorporated within suitable polymers to form composites that combine desired properties of both components [14–16]. Ceramic/polymer nanocomposites should retain advantages emanating from the reinforcing phase, such as high dielectric permittivity, excellent thermal stability and high stiffness in compression, and the polymer matrix, such as low density, flexibility,

facile processability, and high dielectric breakdown strength [17]. However, dispersing nano-ceramic particles, such as bariun titanate, in a polymer matrix in order to form a high-k composite, creates an extensive interfacial area, which has a crucial effect on the overall dielectric performance of the system. Therefore, it is necessary to study the dielectric properties, the employed processing route, and the synergy of the composite's constituents before polymer matrix/high-k materials could be exploited in technological applications [18]. Current applications of this type of composites include multilayer ceramic capacitors (MLCC's), thermistors, electro-optic components, integrated capacitors, thin films electronic component materials, acoustic emission sensors, moreover they proved to be useful for the reduction of leakage currents [19]. Additionally, ceramic/polymer nanocomposite can be exploited in the development of dielectric-based capacitors for energy storage in novel electronics used in electric vehicles, cellular phones, medical devices, wireless personal digital assistants etc. [17, 20]. Embedded nano-inclusions can be considered as a distributed network of nano-capacitors, which can be charged and discharged defining thus an energy storing procedure at the nano-scale level [3, 21]. Furthermore, ceramic/polymer composites appear to be attractive to researchers, nowadays, because of their simple and convenient manufacturing processes, low cost, enhanced properties and outstanding compatibility with printed wiring board (PWB), such as lower dielectric loss, lower conductivity and leakage current [22].

In this study, novel composite materials have been produced, by combining two types of polyesters, with different chemical raw materials, as the polymer matrix and nano-particles of barium titanate as the reinforcing phase at various loadings. Prepared specimens were then tested by means of different experimental techniques aiming to identify their structural, mechanical, thermal and dielectric properties. Structural characterization took place via a number of experimental techniques (such as scanning electron microscopy-SEM, energy dispersive X-ray spectroscopy-EDAX and infra red spectroscopy via Fourier transformation-FTIR). Thermal, mechanical and dielectric properties were examined by means of differential scanning calorimetry (DSC), three point shear and bending tests and broadband dielectric spectroscopy (BDS), respectively.

2. Experimental
2.1. Laboratory unsaturated polyester polymerization process

The polymerization process was held via a polyesterification reaction. This is a polycondensation reaction, which is a typical step-growth polymerization, so water molecules were removed from the reactor by using distillation method with recirculation (vapour reflux reactor) with 2000 mL capacity. The raw materials that have been used in the polyesterification reaction were maleic and adipic acid in the molar proportion of 60–40% and ethylene glycol in the molar proportion of 110% (this ratio refers to the feed ratio of the reactor). These monomers were used with ethylene glycol with 10% molar excess over stoichiometry, because of the fact that ethylene glycol evaporates during the reaction. Toluene was used as a reflux fluid (3.5% v/w of total monomers) and hydroquinone was employed as inhibitor (0.013% w/w of total monomers) [23–25]. The product of the polymerization was the development of the laboratory unsaturated polyester with the code type MA6AA4. For controlling the progress of polymerization, a dynamic temperature profile was used at different final temperature values. Measurements of the generated water quantities versus time, lead to the determination of such stages of the polymerization. So as a consequence, Acid Number (AN) of the final product was determined by titration with 0.5N methanolic potassium hydroxide solution and calculated 44 mgKOH/g polyester, which is an accepted value according to literature [23, 24]. Not only Acid Number but also other kinetic parameters, regarding polymerization process, have been calculated and are exposed in Table 1 (theoretical background is not referred here, as it is thoroughly explained in other works) [23–25]. Except from Acid Number the progress of the polyesterification was studied via the amount of the eliminated water [25, 26]. Time duration of the whole polymerization process was between 6 and 10 h.

Table 1. Kinetic parameters regarding polyesterification polymerization process of laboratory unsaturated MA6AA4 polyester

U.P. code type	E_a		k_0	R^2
	[Kcal/mol]	[kJ/mol]	[kg·mol^{-2}·min^{-1}]	
MA6AA4	26.27	110.09	$2.92 \cdot 10^{10}$	0.986

2.2. Composite specimens preparation-curing process

In the unsaturated polyester MA6AA4, in order to be ready for the curing process, it was necessary to add styrene (30% w/w of the produced amount of polyester) and hydroquinone (0.03% of styrene's quantity) in its liquid form [24]. Afterwards liquid/solid mixtures (cured system) were prepared by mixing polyester (either commercial polyester type: thixotropic polyester with accelerator, Neotex, Athens, Greece or laboratory-MA6AA4 one), barium titanate nano-particles (Sigma Aldrich, Taufkirchen, Germany) (with mean diameter in the range: 30–50 nm), methyl ethyl ketone peroxide (MEKP) as initiator and cobalt (II) naphthenate (CoNp) as accelerator. The proportion of MEKP was 3% v/w and CoNp was 1% v/w (both proportions are referred on polyester's quantity) [23–25]. The specimen's content in barium titanate ranged from 0–20% w/w. Mixtures were magnetically stirred for 15 min approximately and then poured in the closed-type steel moldings. Afterwards moldings were sealed with specific caps and then placed in the thermo-compressor. The mixtures then were cured using compression molding technique. The curing program consisted of two stages. Firstly, nano-composites underlie no pressure at 60°C for 15 min, while in the second stage pressure of 8.5 MPa was applied at 60°C for 15 min.

2.3. Structural characterization

Concerning the study of specimen's surface and the nanoparticle's dispersion in the polymer matrix Scanning Electron Microscopy (SEM) has been used. The employed SEM device is a FEI Quanta 200 (FEI Company, Dawson Creek Drive, Hillsboro, USA), equipped with Element Dispersive X-Ray Analysis (EDAX).

Additionally, the structure of both types of composite systems was examined by means of X-ray diffraction (XRD) scans by means of Siemens D5000 Diffractometer (Siemens, Germany), using a Cu Kα source, scanning in the range 5 to 120°, with a step of 0.0020° and a step time of 1 sec. XRD measurements were carried out at specimens with 0, 5, 20% content in BaTiO$_3$ (for both kinds of composites, either with the commercial polyester as a polymer matrix or the laboratory MA6AA4 one) and pure BaTiO$_3$ nano-powder.

Chemical bonds of both polyesters and barium titanate, were studied via vibrational spectroscopy and particular by means of infra red spectroscopy via Fourier transformation (FT-IR) (Perkin Elmer FT-IR Spectrum GM-Waltham, Massachusetts, U.S.A.). The measurements are in the form of transmittance versus wavelength in the spectrum region of middle infra red irradiation between 4000–200 cm^{-1}.

2.4. Thermal analysis

A DSC Q200 (TA Instruments, Lukens Drive, New Castle, U.S.A.) Differential Scanning Calorimeter setup operating at a scan rate of 10°C/min was used to characterize thermal transitions of the employed polyester resins and composite systems. Samples were placed within an aluminum crucible, while an empty aluminum crucible was serving as reference material. Temperature was varied from ambient to 200°C, followed by an isothermal stage at 200°C for 1 minute. Afterwards, the cooling process consisted of cooling until 0°C (via nitrogen flow) again with a cooling rate of 10°C/min. The aim of this characterization was the determination of glass transition temperatures (T_g) of each specimen. The determination of T_g was carried out via the point of inflexion of the transition.

2.5. Mechanical characterization

Composite specimens both with commercial or laboratory polyester matrix were mechanically tested using the three-point method, employing bending (DIN-53452) and shear (ASTM-NORM D 2344-65T) strength tests [27]. Between these two tests the only difference is that in the shear strength test the distance between the two points was 10 mm, while in the bending strength test was 100 mm. In both of them, the evaluated parameter was the deflection in μm. Obtained data were used for the calculation of the shear and bending strength for each sample in MPa [27, 28]. All mechanical tests took place at room temperature (25°C). Specimens are classified in two types: in the first one the dimensions are 13,5 cm length, 17 mm width and 3 mm thickness (specimens for shear tests) and in the second one the dimensions are 13 cm length, 10 mm width and 3 mm thickness.

2.6. Dielectric characterization

Dielectric measurements were conducted by means of Broadband Dielectric Spectroscopy (BDS) in the frequency range of 0.1 Hz to 1 MHz, using an Alpha-N Frequency Response Analyser (Novocontrol Technologies, Hundsagen, Germany). The employed dielectric cell (BDS-1200, Novocontrol) is a parallel-plate capacitor with two gold-plated electrodes. Temperature was controlled via Quatro device, supplied also by Novocontrol, with accuracy ±0.1°C. Experimental data were obtained by performing isothermal frequency scans, for each examined specimens, from –100 to 160°C with a temperature step of 10°C. The amplitude of the applied test voltage was kept constant at 1000 mV. The specimens that underwent such measurements were: 0, 5, 10 and 20% w/w in BaTiO$_3$ content for both kinds of polyester polymer matrices.

3. Results and discussion
3.1. Scanning electron microscopy (SEM) and energy dispersive X-ray spectroscopy (EDAX) characterization

SEM images depicted in Figure 1, reveal that the dispersion of barium titanate's nano-particles is quite satisfactory for both types of polyesters, because of the absence of extensive barium titanate's agglomerates. However, clusters as well as nano-dispersions can be detected in all studied systems. In relation to specimen's topography, the surface is more smooth and flat without so many micro-cavities for the case of laboratory polyester. Commercial polyester has probably more micro-cavities and bigger agglomerates' diameter because of its' higher viscosity, in comparison to the low viscosity of the laboratory polyester. High viscosity leads to more difficult mixture of the raw materials during the curing process and also in obstruction in filling of the molds. Another parameter which assists the creation of rough surface is the employment of poly(vinyl alcohol) (PVA). Its effect is more evident in composites with commercial polyester resin (Figure 1a). PVA was used as a lubricant of the molding parts, in order to remove easily and without any damage the cured specimens from the mold. Compression molding technique rises temperature and pressure. This fact leads, PVA to create corrugations in the surface of
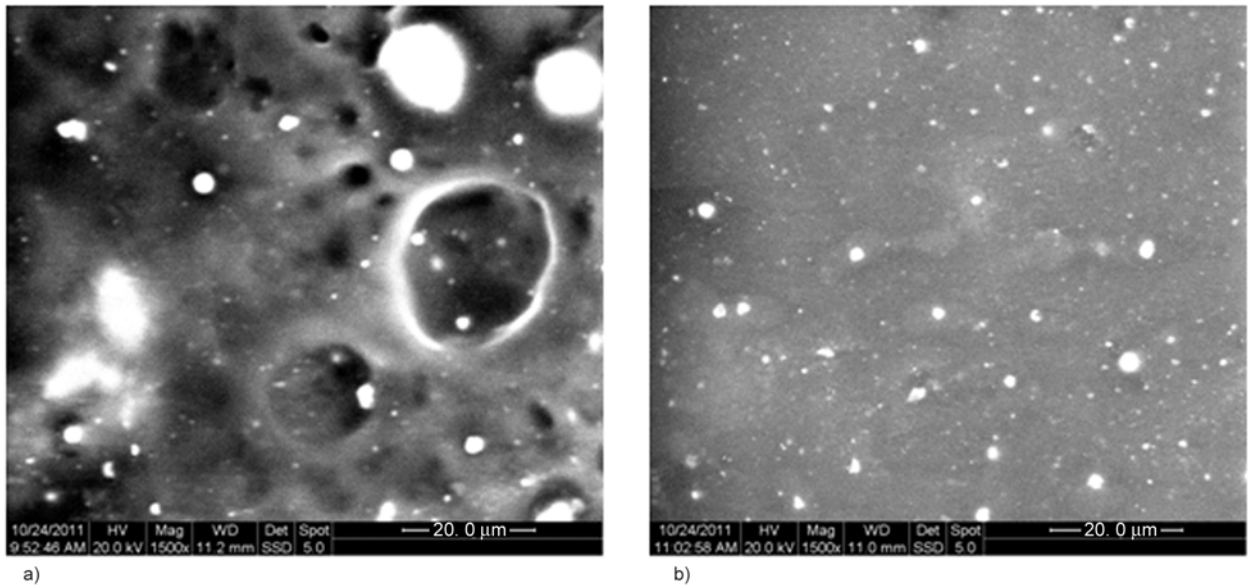
Figure 1. Scanning electron microscopy images from nano-composite specimen with 20% w/w content in BaTiO$_3$ for a magnification of about 1500 times (×1500) embedded in: commercial polyester polymer matrix (a), laboratory MA6AA4 polyester polymer matrix (b)

Table 2. Energy dispersive X-ray spectroscopy measurements from nano-composite specimen with 20% w/w content in BaTiO$_3$ embedded in: commercial polyester

Chemical element	C(K)	O(K)	Ba(L)	Ti(L)	Total
Proportion in % (c.p)	36.81	12.98	40.48	9.73	100.00
Proportion in % (l.p.)	43.58	15.60	31.87	8.95	100.00

the polymer matrix prior being evaporated. Commercial polyester, because of its higher viscosity, traps the initially liquid PVA and as a result the finally evaporated PVA, creates the micro-cavities. On the other hand laboratory polyester with low viscosity helps PVA to evaporate and escape from the specimen easier and quicker without creating cavities.

Energy dispersive X-ray spectroscopy (EDAX) measurements (Table 2) detect the presence carbon, barium, oxygen and titanium, as expected. The highest proportion of all detected chemical elements corresponds to carbon, due to the polymer matrix.

3.2. X-ray diffraction (XRD) characterization
The obtained XRD spectra of the above mentioned specimens are depicted in Figure 2. Spectra from unfilled specimens exhibit a wide peak at low values of 2θ angle characteristic for amorphous materials such as the employed polymers. On the other hand BaTiO$_3$ spectrum reveals its crystalline nature via the formed sharp peaks. Plots from the nano-composites with 5 and 20% w/w content in BaTiO$_3$ include contributions from both constituent materi-
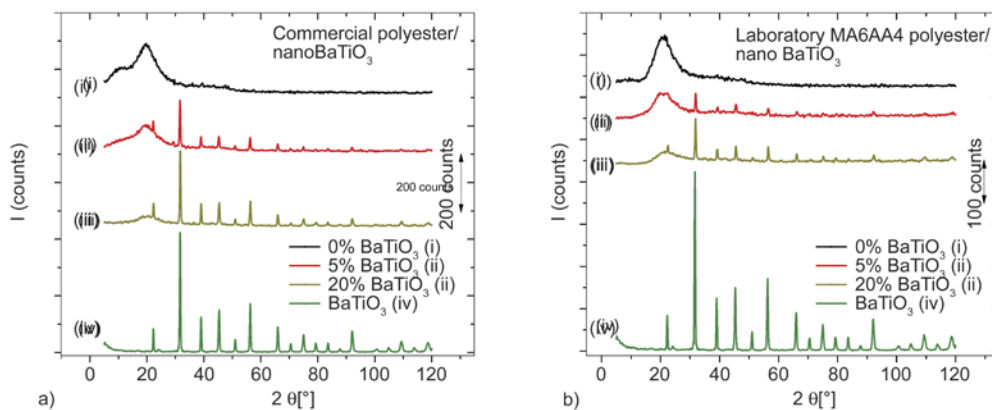

Figure 2. X-ray diffraction spectra from pure BaTiO$_3$ nano-particles and specimens with 0, 5, 20% w/w in BaTiO$_3$ within: commercial polyester (a), laboratory polyester (b)

als. Polymer matrix provides the wide peak, while the presence of ceramic particles becomes evident via a number of sharp peaks. The relative intensity of the recorded peaks is representative for the amount of each constituent material in the nanocomposite's composition [29]. It is interesting to note that all recorded reflections, including the one from the amorphous polymers, are shifted to higher values, in the case of the specimens with the laboratory produced polyester compared to the specimens based on the commercial polyester. In particular, the wide peak of the amorphous phase appears, for the commercial polyester at 19.7°, while for the laboratory one at 21.4°. In the literature, values of 2θ for the amorphous peak of unsaturated polyesters range between 21.2 to 21.4°. The laboratory polyester (MA6AA4) exhibits its peak within this region. The slight deviation of the commercial type should be attributed to the presence of catalysts residues, resulting from the stage of its production. However, the producing company does not provide details upon the synthesis procedure, the type and the amounts of the used chemicals in the relative product sheet, and thus only qualitative comments can be made. Reflections related to $BaTiO_3$ in composites with commercial resin appear at the same values of 2θ angles with the corresponding of pure barium titanate. On the contrary, all relative XRD peaks in the laboratory polyester based composites are shifted to higher 2θ values systematically. Specimen with 5% w/w in $BaTiO_3$, displays a peak shift of 0.32°, while specimen with 20% w/w in $BaTiO_3$ displays a 0.16° peak shift. This behaviour could be related to a distortion of the unit cell because of enhanced hardening (via curing process) in the case of MA6AA4 resin. The unit cell distortion results in lowering the distance of the adjacent planes, and thus in accordance with Bragg law peaks are shifted to higher values.

3.3. Infra red spectroscopy via Fourier transformation (FT-IR) characterization

Figure 3, depicts the FT-IR imprint of barium titanate nano-powder. This spectrum can be divided into five characteristic regions. Region i, is the most important peak for barium titanate and corresponds to wavelength range between 530–700 cm^{-1} (usually between 560–680 cm^{-1}). This peak is due to the vibration of the bond between titanium and oxygen (Ti–O bond) [30–33]. Region ii, corresponds to a
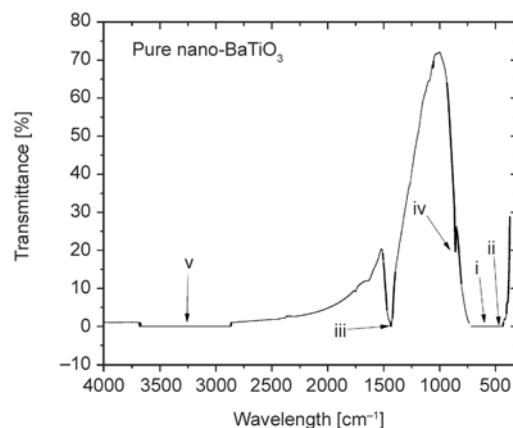

Figure 3. Infra red spectroscopy via Fourier transformation (FT-IR) spectrum from pure $BaTiO_3$ nano-powder at a wavelength range between 4000–200 cm^{-1}

peak at 450 cm^{-1} approximately, which is caused by vibrations between metal atoms and oxygen (Ti–O and Ba–O bonds) [30, 32, 34]. Both previous referred regions are not clearly visible in Figure 3 as from their nature these peaks are difficult to be detected [34]. The formed plateau in the range 993–370 cm^{-1}, indicates their presence instead of a clear separation between the two peaks. The most easily detected region iii, corresponds to a wavelength at 1453 cm^{-1} and has to do with carbonate ion impurities (C–O bond) [30], which ordinarily came from barium titanate's synthesis. Region iv at 859 cm^{-1} corresponds to bonds between Ba, Ti and O. The last region v, corresponds to a large range of bands between 3670–2870 cm^{-1}, which has to do with absorbed moisture from the pellets due to hygroscopic potassium bromide.

The aim of the FT-IR measurements, besides that they are performed for the first time in the specific composite systems, is to examine if the vibration of characteristic bonds of the polymeric matrices is affected by the presence of barium titanate and to what extent. Figures 4 and 5 show the spectra from all the examined composites, while the main peaks of each kind of pure polyester are listed in Table 3. All the basic characteristic peaks related to polyesters according to the literature [23–25, 35–41] are present and detectable in the spectra of both kinds of polyesters. The symbols used for the identification of each peak, can be explained as follows: i) regarding the shape of the peak: (sh) means sharp and (br) means broad, ii) regarding the magnitude of the peak: (s) means strong, (m) means medium, (w) means weak and (pl) means plateau. Table 4

Table 3. FT-IR spectra characteristic peaks from the two kinds of polyester polymer matrixes

Characteristic chemical group	Wavelength from literature [cm⁻¹]	Peak appearance wavelength [cm⁻¹]	
		Composite's polyester polymer matrix	
		Commercial polyester	Laboratory MA6AA4 polyester
–OH vibration stretch	3600–3200	3534 w/br 3443 w/br	3540 w/br 3459 w/br
C–H vibration stretch, styrene's aromatic ring	3024	3029 w/sh	3029 w/sh
>CH₂, –CH₃ vibration stretch, aliphatic parts	2980–2950	2980 w/sh 2934 m/sh	2958 m/sh
>CH₂ vibration stretch, circular and linear parts	2890–2850	2980 w/sh	2878 w/sh
>C=O vibration stretch	1736–1726	1731 s/sh	1736 s/sh
C=C vibration stretch within the aromatic ring	1600 1580 1500	1600 m/sh 1581 m/sh 1494 m/sh	1603 w/sh – 1495 w/sh
C–C vibration stretch within the aromatic ring	1480–1400	1453 s/sh	1456 m/sh
CH₃ symmetric bending vibration	1390–1370	1381 w/sh	1393 m/sh
C$_{sp3}$–O (ester bond)	1330–1200	1283 s/br	1250 w/br
C$_{sp3}$–O (alcohol bond)	1200–1100	1122 m/br	1162 m/sh
C–H «in plane» vibrations	1080–1036	1068 m/sh	1077 m/br
C=C unsaturated polyester's double bond	982	990 w/br	978 w/sh
C=C styrene's double bond	912	913 w/br	–
C–H deformation vibration «out of plane» 1 or 2 neighbour H of benzene ring	876–815	847 m/br	877 w/sh 814 w/br
C–H deformation vibration «out of plane» 3 or 4 neighbour H of benzene ring	750	745 s/sh	764 m/sh
C–H deformation vibration «out of plane» 5 neighbour H of benzene ring	700 666	700 s/sh 649 w/br	703 s/sh

lists peaks and vibrational modes of pure BaTiO₃ and of BaTiO₃/nanocomposites. It is easily noticeable, a difference in the characteristics of each peak. This difference is attributed to the increase of the proportion of BaTiO₃ in the specimens, thus a variation in the intensity of each peak occurs.

Finally, there are two important remarks that must be noted. The first one is that there is a specific region in the FTIR spectra that is characteristic for each specimen relative to its' content in barium titanate compared to the intensity of a certain peak. For the specimens with commercial polyester, this specific region is located between 458–431 cm⁻¹, while in specimens with laboratory polyester this region is located between 432–428 cm⁻¹. The second one is that independently from barium titanate's content in each specimen, all the recorded peaks remain in the same values of wavelength, in contrast to similar composite systems [42].
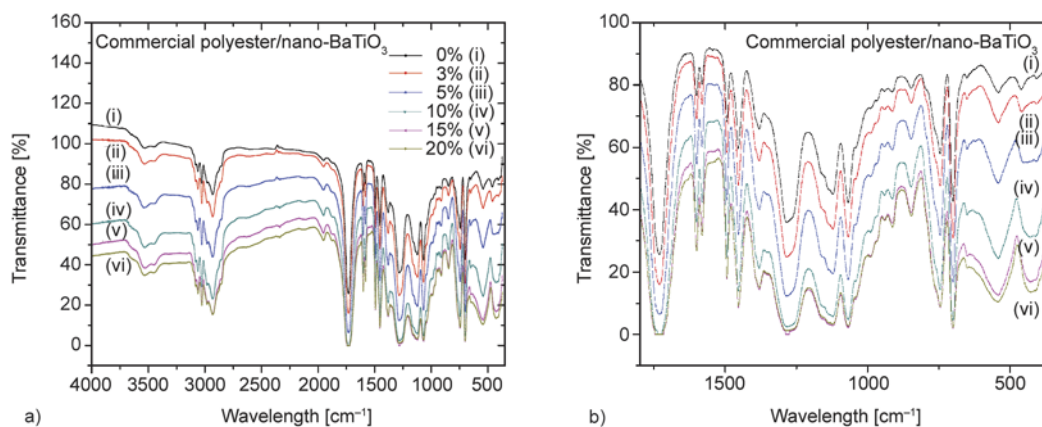
Figure 4. Infra red spectroscopy via Fourier transformation (FT-IR) spectra from specimens with 0–20% w/w content in BaTiO$_3$ nano-particles within commercial polyester at a wavelength range between: 4000–200 cm^{-1} (a) and 1800–350 cm^{-1} (b)
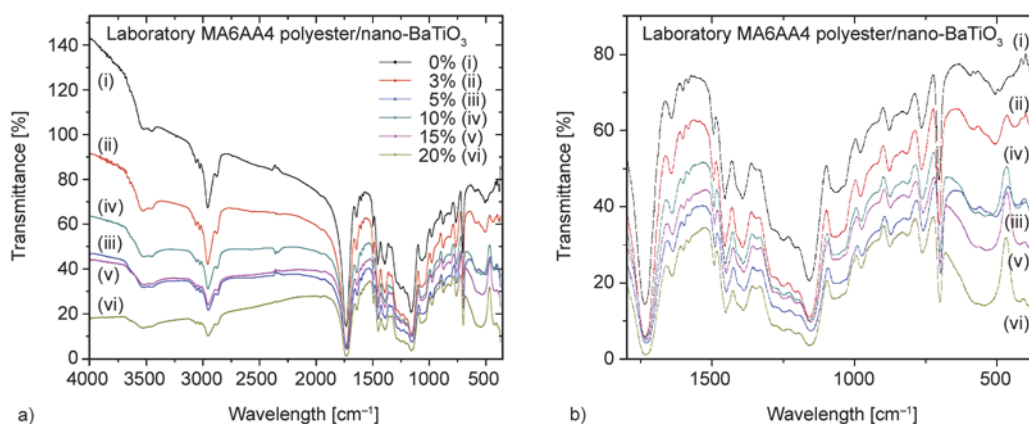

Figure 5. Infra red spectroscopy via Fourier transformation (FT-IR)) spectra from specimens with 0–20% w/w content in BaTiO$_3$ nano-particles within laboratory MA6AA4 polyester at a wavelength range between: 4000–200 cm^{-1} (a) and 1800–350 cm^{-1} (b)

Table 4. FT-IR spectra characteristic peaks from pure BaTiO$_3$ nano-powder and all kind of developed composites with either commercial or laboratory polyester polymer matrix

Characteristic chemical group	Wavelength from literature [cm^{-1}]	Peak appearance wavelength [cm^{-1}]		
		pure BaTiO$_3$	Composite's polyester polymer matrix	
			Commercial polyester	Laboratory MA6AA4 polyester
Ba–O, Ti–O vibration stretch	405–450 m/sh	432–727 pl	458 w/br (3, 5% w/w BaTiO$_3$) 431 m/br (10–20% w/w BaTiO$_3$)	432 w/br (3, 5% w/w BaTiO$_3$) 428 m/br (10–20% w/w BaTiO$_3$)
Ti–O vibration stretch	530–700 s/sh	432–727 pl	541 w/br (3, 5% w/w BaTiO$_3$) 541 m/br (10-20% w/w BaTiO3)	504 w/br (3, 5% w/w BaTiO$_3$) 504 m/br (10–20% w/w BaTiO$_3$)
Ba–O, Ti–O vibration stretch	852–860 w/sh	857 w/sh	847 w/sh (3% w/w BaTiO$_3$) 847 m/sh (5–20% w/w BaTiO$_3$)	–
C–O vibration stretch	1440–1444 m/sh	1433 m/sh	1453 s/sh (3–20% w/w BaTiO3)	1455 m/sh (3% w/w BaTiO$_3$) 1450 w/sh (5% w/w BaTiO$_3$) 1453 w/sh (10% w/w BaTiO$_3$) 1451 w/sh (15% w/w BaTiO$_3$) 1452 w/sh (20% w/w BaTiO$_3$)
–OH vibration stretch	3389–3433 m/br	2866–3674 pl	–	–

3.4. Thermal characterization

Glass transition temperature (T_g) of pure commercial polyester resin was found to be 57°C, while T_g of pure laboratory MA6AA4 polyester resin was found to be 45°C. The T_g of all the other examined systems are shown in Figure 6. The main tendency for the nanocomposites of both polyester polymer matrices is the reduction of T_g with the increase of

BaTiO$_3$ content. Variation of T_g with filler content in polymer matrix micro- or nanocomposites has been observed and reported previously [43]. Variation has been attributed to the type of the occurring interactions (strong or weak) between the reinforcing particles surface and the macromolecular chains, as well as to the level of adhesion of the filler by the matrix. Lowering of T_g implies weak interactions and poor adhesion between filler and polymer matrix. If the macromolecules are not anchored on the particles surface, their co-operative movement is facilitated and thus less thermal energy should be provided to the system in order to relax simultaneously. The latter becomes evident with a systematic reduction of T_g with ceramic filler content. The impact of glass transition temperature leveling of on the composites' performance, results in narrowing the temperature range where the materials can serve appropriately. Figure 6 depicts this behaviour, points represent the mean value between the upper and lower limit of the glass transition range [44]. It is interesting to note that the diminishing rate of T_g with the BaTiO$_3$ content, as expressed by the slope of the average values from Figure 6, varies with the type of the polymer matrix. Slope for composites with commercial polyester is equal to –3.63°C/% w/w BaTiO$_3$ content, while slope for laboratory polyester is equal to –0.54°C/% w/w BaTiO$_3$ content. This difference, by an order of magnitude, can be considered as a clear indication for the quality of the produced nanocomposites and the achieved dispersion of ceramic particles within the employed polyesters. Laboratory produced polyester appears to be more suitable for the preparation of nanocomposites and the adhesion between matrix and filler is enhanced in this case. It should be noted that

morphological investigation via SEM previously mentioned, lead to the same conclusion.

3.5. Mechanical characterization

The results of shear and bending tests, for all the examined specimens, are shown in Tables 5 and 6. It is clear that shear strength values decreases as BaTiO$_3$ content increases. This behaviour is consistent with the DSC results (diminishing of T_g point), so the fact that the adhesion between polyester polymer matrix and nano-particles hinders with the increase in BaTiO$_3$ content is further confirmed. The same behaviour occurs in the specimens with laboratory polyester as polymer matrix, but in this case in a smoother way. As it can be seen maximum shear strength values, for all the nanocomposite systems, are quite close. Another important remark is that shear strength values, for specimens with commercial polyester are approximately two times higher than the corresponding values for specimens with laboratory polyester. Maximum bending strength values are approximately ten times higher than the corresponding shear strength values for composites with commercial polyester. These differences between both types of polyesters are in accordance with the brittle performance of the commercial one. Concerning the bending tests for specimens with laboratory polyester, should be noted that all samples demonstrated an elastomeric behaviour being thus unable to reach fracture. This qualitative modification, in the mechanical performance, between the two types of the employed polyesters can be considered responsible for the observed differences via SEM and DSC tests in the two sets of nanocomposites. The elastomeric performance of laboratory polyester based nanoscomposites is shown in Figure 7. The occur-
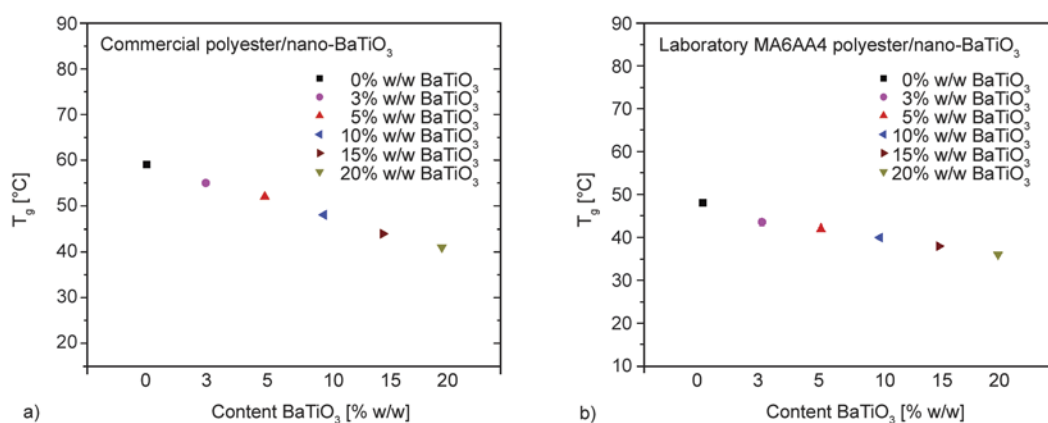

Figure 6. T_g values for each specimen versus % content in BaTiO$_3$ nano-particles with: commercial polyester (a) and laboratory MA6AA4 polyester polymer matrix (b)

Table 5. Deflection, maximum applied force, shear strength and error range of shear strength values for shear tests

Kind of polyester polymer matrix	Specimen's content in BaTiO₃ [% w/w]	Diflection, x [μm]	Maximum applied force, P_max [N]	Shear strength, τ_b [MPa]	Shear's strength error range ± [MPa]
Specimens with commercial polyester/BaTiO₃	0	15.2	244.4	3.90	0.3
	3	14.2	228.3	3.65	0.3
	5	10.8	173.6	2.80	0.2
	10	8.8	141.5	2.25	0.2
	15	8.2	131.8	2.10	0.2
	20	7.8	125.4	2.00	0.1
Specimens with laboratory MA6AA4 polyester/BaTiO₃	0	7.8	125.4	2.00	0.1
	3	7.0	112.5	1.80	0.1
	5	7.2	115.8	1.85	0.1
	10	6.8	109.3	1.75	0.1
	15	6.7	107.7	1.70	0.1
	20	6.2	99.7	1.60	0.1

Table 6. Deflection, maximum applied force, bending strength and error range of bending strength values for bending tests

Kind of polyester polymer matrix	Specimen's content in BaTiO₃ [% w/w]	Diflection, x [μm]	Maximum applied force, P_max [N]	Bending strength, σ_b [MPa]	Bending's strength error range ± [MPa]
Specimens with commercial poly-ester/ BaTiO₃	0	1.2	19.3	33.75	2.4
	3	1.1	17.7	30.95	2.2
	5	0.9	14.5	25.30	1.8
	10	0.9	14.5	25.30	1.8
	15	0.8	12.9	22.50	1.6
	20	0.7	11.3	19.70	1.4

Figure 7. Snapshot showing the elastomer nature of composites with laboratory polymer matrix during bending tests

ring elastomeric performance is ascribed to the structure of the MA6AA4 laboratory polyester. During its synthesis the concentrations of acid raw materials are the following: 60% maleic acid and 40% adipic acid. Thus the elastomeric behaviour of the nanocomposites – with the laboratory polymer matrix – is attributed to the high percentage of adipic acid in the final thermosetting unsaturated polyester structure. Adipic acid has a linear structure without any ramifications; therefore the polymer chain acquires mobility. Macroscopically, enhanced polymers' chain mobility is translated to elastomeric mechanical behaviour.

3.6. Broadband dielectric spectroscopy (BDS) characterization

Dielectric data were firstly expressed in terms of dielectric permittivity and then transformed via Equation (1) in terms of electric modulus. Electric modulus is considered as an effective formalism for the investigation of dielectric data, since it eliminates the parasitic and undesirable effect of electrode polarization [45–47]. Electric modulus is defined as the inverse quantity of complex permittivity, as shown in Equation (1):

$$M^* = \frac{1}{\varepsilon^*} = \frac{1}{\varepsilon' - j\varepsilon''} = \frac{\varepsilon'}{\varepsilon'^2 + \varepsilon''^2} + j\frac{\varepsilon''}{\varepsilon'^2 + \varepsilon''^2} = M' + jM'' \tag{1}$$
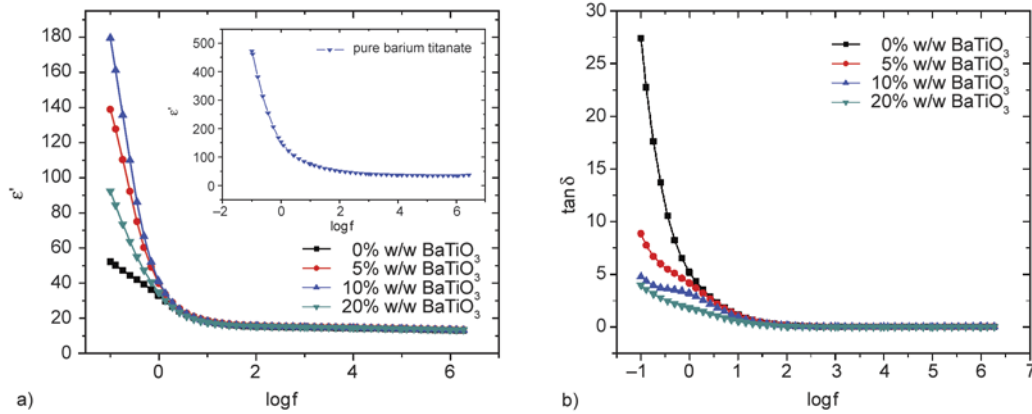
Figure 8. Real part of dielectric permttivity (a), and tan δ (b) as a function of frequency for the laboratory based systems, at 50°C. Inset depicts the variation of (ε′) versus logf, at 50°C, for pure barium titanate

where ε', M' and ε'', M'' are the real and the imaginary parts of dielectric permittivity and electric modulus respectively.

The variation of the real part of dielectric permittivity as a function of frequency, at 50°C, for all the laboratory polyester (MA6AA4) based systems is shown in Figure 8a, while inset presents (ε') as a function of frequency, at the same temperature, for pure barium titanate. In all cases (ε') diminishes with frequency reflecting the decrease of polarization due to the inertia of the dipoles to follow the alternation of the applied field. Permittivity alters with filler content, but this increase appears not be systematic indicating that the optimum performance does not correspond to the maximum barium titanate content. This point is further discussed later. The variation of loss tangent for the same systems is given in Figure 8b. Loss tangent acquires high values in the low frequency range, and curves are shifted to lower frequencies as the ceramic filler content increases. Recorded behaviour is ascribed to interfacial polarization [45–47], although the

high values of losses could be, possibly, influenced by electrode polarization. Analogous behaviour has been found for the commercial polyester based systems.

Figure 9 depicts the loss modulus index versus temperature spectra of all the examined systems, at 10^2 Hz, where all the recorded relaxation phenomena are present. Three relaxation processes are evident in the spectra of commercial polyester based systems in Figure 9a, while four relaxations are detected in the spectra of the MA6AA4 polyester based nanocomposites in Figure 9b. In the second case, the two faster mechanisms, namely γ- and β-mode, are recorded in the range from 2 to 7°C and 9 to 13°C, respectively. These modes are characterized by short relaxation times and are assigned to local motions or re-arrangements of small polymer parts. In particular, γ-mode is attributed to the motion of small parts of the main polymer chain, such as hydrogen and phenyl's aromatic ring, which are connected with carbon atoms of the main polymer chain with single bonds. Further, β-mode is related
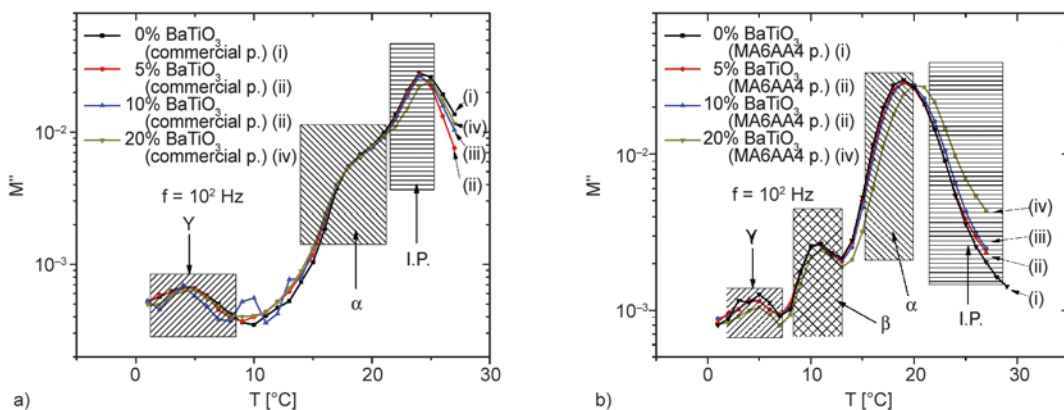

Figure 9. Imaginary part of electric modulus versus temperature at 10^2 Hz, for specimens with commercial polyester (a) and laboratory MA6AA4 polyester (b)

to the re-arrangement of polar side groups, which in our case are oxygen atoms connected with carbon atoms of the main polymer chain via double bonds. Glass to rubber transition of the matrix gives rise to a slower relaxation process (α-mode), recorded in the vicinity of 18°C. The difference between the determined values of T_g via DSC and BDS should be assigned to the dynamic nature of the glass to rubber transition effect. BDS reflects better the dynamic nature of the process and thus the determined value of T_g depends on the frequency of the applied electrical field. However, the peak depicted in Figure 9b is broad covering a range of almost 15°C, from its onset at 13°C approximately to its end point close to 28°C. This wide and intense peak is attributed to the superposition of two relaxation processes, that is α-mode (13–21°C) and Interfacial Polarization (IP) (22–28°C). IP appears in heterogeneous systems because of the accumulation of non-bonded charges at the interface between the constituents of the system, where they form large dipoles. The inertia of these dipoles to follow the alternation of the applied field is the origin of the IP relaxation process [45–49], which is the slowest recorded effect. In general, IP is strengthened with the increase of the reinforcing phase and its relaxation time is enhanced. The small shift of the loss peak to higher temperatures in the case of the specimen with the maximum filler content is in accordance with the previous remark. Figure 9a presents the loss modulus spectra versus temperature for the systems with the commercially available polyester. The general trend of the recorded response is similar to that of the MA6AA4 polyester based systems. However, differences between Figure 9a and 9b reflect varia-

tions in the systems' structure. In the commercial polyester spectra α-mode and IP are recorded distinctly. α-mode's peak (14–22°C) is present as a 'hump' on the ascending curve, while IP is clearly recorded at higher temperature (23–26°C). The variation of dynamics (peak shift rate with temperature) of both processes from the laboratory to the commercial polyester is responsible for the separation of the effects in Figure 9a. Further, the peak corresponding to β-mode is absent in the spectra of the commercial polyester. Although the accurate chemical structure of the commercial polyester is not given, the absence of β-mode is indicative for the absence of polar side groups in its main polymer chain or at least for the limited presence of such groups. γ-mode's peak is located in the vicinity of 2–8°C for both types of polyesters. Recorded relaxations in Figure 9a, 9b slightly differ with barium titanate content indicating that the dissipation of energy upon each charging cycle does not vary significantly with filler loading.

Figures 10 and 11 present the density of energy for all the examined systems with respect to commercial (a) and laboratory (b) polyester, as a function of the applied frequency (Figure 10) or temperature (Figure 11). The density of energy has been calculated via Equation (2):

$$< u > \ = \frac{1}{2} \cdot \varepsilon_0 \cdot \varepsilon' \cdot \left(\frac{V_0}{d}\right)^2 \qquad (2)$$

where ε_0 is the dielectric permittivity of vacuum, ε' the real part of dielectric permittivity of the corresponding specimen, V_0 is the applied voltage amplitude, which in our case was kept constant at 1 Volt, and d is the specimen's thickness, being equal to
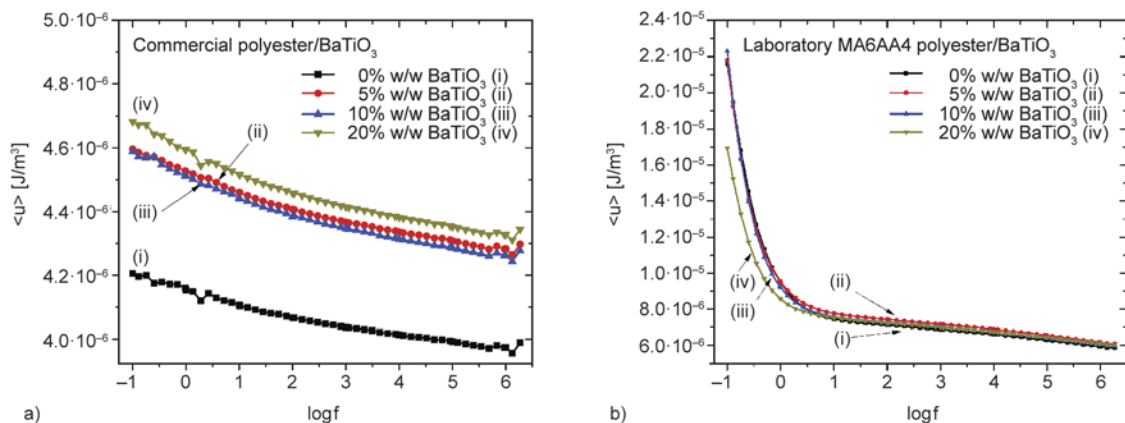

Figure 10. Energy density as a function of frequency for nanocomposites with 0, 5, 10 and 20% w/w BaTiO₃ embedded in: commercial polyester (a), laboratory MA6AA4 (b) polyester as polymer matrix at 30°C
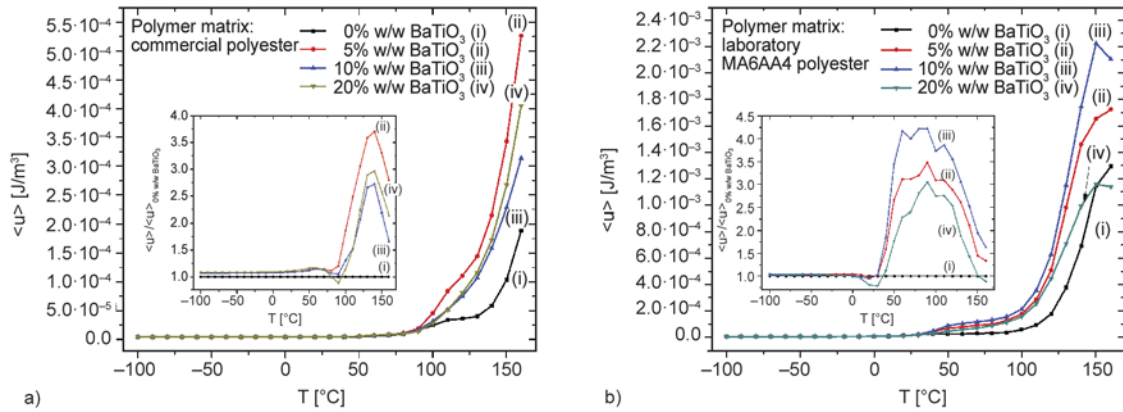
Figure 11. Energy density and normalized energy density versus temperature for nanocomposites with 0, 5, 10 and 20% w/w BaTiO$_3$ embedded in: commercial polyester (a), laboratory MA6AA4 (b) polyester as polymer matrix at 10^{-1} Hz

3 mm. Energy density is a parameter reflecting the storage capability of each nanosystem [50]. From Figure 10 becomes evident that, at constant temperature 30°C, and in the case of the commercial polyester based systems, the specimen with 20% w/w in BaTiO$_3$ exhibits the highest energy storing capability, while in the case of the laboratory polyester based systems highest energy storage is exhibited by the 10% w/w specimen. Further, energy density values for the laboratory based systems appear to be higher by almost an order of magnitude when compared to the values of the commercial polyester matrix systems.

On the other hand, Figure 11, indicates that the highest energy storage capability due to BaTiO$_3$, is displayed by the specimen with 5% w/w BaTiO$_3$ (commercial polyester) and by the specimen with 10% w/w BaTiO$_3$ (MA6AA4 polyester). Insets in Figure 11a and 11b depicts the normalized energy density of both sets of nanosystems, with respect to the pure polymer specimen. In accordance with previous comments, the energy storing capability is stronger in the laboratory polyester based nanosystems. From Figures 10 and 11 is evident that the optimum dielectric performance and/or energy storing efficiency, although is related to the ceramic filler content, does not correspond to the maximum loaded contents of barium titanate nanoparticles. It is apparent from Equation (2) that the only material property related to the density of energy is the real part of dielectric permittivity. At constant field's value, well below the material's dielectric strength, and at constant specimens' thickness, the variation of energy density reflects the variation of (ε'). The latter is influenced by the amount of the employed

barium titanate, the temperature, the frequency of the field, and the quality of dispersion of the BaTiO$_3$ nano-particles. It is well known and documented [51–53] that at low frequencies and high temperatures permittivity attains high values because sufficient time and mobility is given to permanent and induced dipoles to be oriented parallel to the applied field. Moreover, increasing the filler content results in higher values of permittivity, since (ε') of BaTiO$_3$ is much higher than that of the matrix. However, permittivity does not increase monotonically with filler content, as expected, because the quality of the achieved dispersion of the nano-particles diminishes at high BaTiO$_3$ loadings. Nano-particles tend to form clusters and agglomerates and the samples' preparation is significantly hampered. The presence of agglomerates, the weak adhesion between particles and matrix, and the possible formation of small voids lead to lower permittivity values for the nanocomposites with high barium titanate content. Therefore, the corresponding energy density values decrease. Finally, the formed peaks in the insets of Figure 11 are related to the recorded dielectric relaxations processes.

4. Conclusions

Polymer composites with embedded ferroelectric ceramic nano-particles were developed and examined, by employing two types of polyester resin (commercial and laboratory produced) as a matrix. Kinetic analysis took place relative to the polyesterification polymerization of the laboratory MA6AA4 polyester. Composites were developed through compression molding technique, via a thermo-compressor. Structural characterization of both types' nano-

composites was conducted via scanning electron microscopy assisted with electron dispersive X-ray spectroscopy, infra red spectroscopy via Fourier transformation and X-ray diffraction. Morphological investigation revealed that the laboratory polyester based systems exhibit a finer dispersion of $BaTiO_3$ nano-particles. Thermal analysis via differential scanning calorimetry was used for the detection of T_g point for all the composite systems versus barium titanate content. It was found that glass transition temperature decreases with filler content, in both types' polyester composites. Mechanical properties, such as shear and bending tests, were tested and found out that with the increase in barium titanate nano-filler, the corresponding strength values became worst. Contrariwise, dielectric properties and energy storage capability present an increase while barium titanate content increases. However, the dielectric reinforcing capability appears not to increase monotonously with ceramic filler content, implying that the optimum dielectric performance does not correspond to the maximum loaded filler. Finally, the observed dielectric relaxations were attributed, descending relaxation times, to interfacial polarization, glass to rubber transition of the polymer matrix, re-arrangement of polar side groups of the main polymer chains and motion of small parts of the macromolecular chains.

References

[1] Parthenios J., Psarras G. C., Galiotis C.: Adaptive composites incorporating shape memory alloy wires. Part 2: Development of internal recovery stresses as a function of activation temperature. Composites Part A: Applied Science and Manufacturing, **32**, 1735–1747 (2001).
DOI: 10.1016/S1359-835X(01)00022-7

[2] Gandhi M. V., Thompson B. S.: Smart materials and structures. Champan and Hall, London (1992).

[3] Psarras G. C.: Nanodielectrics: An emerging sector of polymer nanocomposites. Express Polymer Letters, **2**, 460 (2008).
DOI: 10.3144/expresspolymlett.2008.55

[4] Vinothini V., Singh P., Balasubramanian M.: Synthesis of barium titanate nanopowder using polymeric precursor method. Ceramics International, **32**, 99–103 (2006).
DOI: 10.1016/j.ceramint.2004.12.012

[5] Duran P., Gutierrez D., Tartaj J., Moure C.: Densification behaviour, microstructure development and dielectric properties of pure $BaTiO_3$ prepared by thermal decomposition of (Ba, Ti)-citrate polyester resins. Ceramics International, **28**, 283–292 (2002).
DOI: 10.1016/S0272-8842(01)00092-X

[6] Petrović M. M. V., Bobić J. D., Ramoška T., Banys J., Stojanović B. D.: Antimony doping effect on barium titanate structure and electrical properties. Ceramics International, **37**, 2669–2677 (2011).
DOI: 10.1016/j.ceramint.2011.04.015

[7] Popielarz R., Chiang C. K., Nozaki R., Obrzut J.: Dielectric properties of polymer/ferroelectric ceramic composites from 100 Hz to 10 GHz. Macromolecules, **34**, 5910–5915 (2001).
DOI: 10.1021/ma001576b

[8] Korotkov N., Gridnev S. A., Konstantinov S. A., Klimentova T. I., Barmin Y. V., Babkina I. V.: Dielectric permittivity and conductivity of amorphous $PbTiO_3$. Ferroelectrics, **299**, 171–177 (2004).
DOI: 10.1080/00150190490429637

[9] Jylhä L., Honkamo J., Jantunen H., Sihvola A.: Microstructure-based numerical modeling method for effective permittivity of ceramic/polymer composites. Journal of Applied Physics, **97**, 104104/1–104104/7 (2005).
DOI: 10.1063/1.1897071

[10] Duran P., Tartaj J., Moure C.: Sintering behaviour and microstructural evolution of agglomerated spherical particles of high-purity barium titanate. Ceramics International, **29**, 419–425 (2003).
DOI: 10.1016/S0272-8842(02)00154-2

[11] Safari A., Panda R. K., Janas V. F.: Ferroelectricity: Materials, Characteristics and Applications. Advanced Ceramic Materials: Key Engineering Materials, **122–124**, 35–71 (1996).
DOI: 10.4028/www.scientific.net/KEM.122-124.35

[12] Schumacher B., Geßwein H., Haußelt J., Hanemann Th.: Temperature treatment of nano-scaled barium titanate filler to improve the dielectric properties of high-*k* polymer based composites. Microelectronic Engineering, **87**, 1978–1983 (2010).
DOI: 10.1016/j.mee.2009.12.018

[13] Asimakopoulos I., Zoumpoulakis L., Psarras G. C.: Development and characterization of a novolac resin/$BaTiO_3$ nanoparticles composite system. Journal of Applied Polymer Science, **125**, 3737–3744 (2012).
DOI: 10.1002/app.36518

[14] Abraham R., Thomas S. P., Kuryan S., Isac J., Varughese K. T., Thomas S.: Mechanical properties of ceramic-polymer nanocomposites. Express Polymer Letters, **3**, 177–189 (2009).
DOI: 10.3144/expresspolymlett.2009.23

[15] Smay J. E., Cesarano S., Tuttle B. A., Lewis J. A.: Piezoelectric properties of 3-X periodic $Pb(Zr_xTi_{1-x})O_3$–polymer composites. Journal of Applied Physics, **92**, 6119–6127 (2002).
DOI: 10.1063/1.1513202

[16] Pradhan D. K., Choudhary R. N. P., Samantaray B. K.: Studies of structural, thermal and electrical behavior of polymer nanocomposite electrolytes. Express Polymer Letters, **2**, 630–638 (2008).
DOI: 10.3144/expresspolymlett.2008.76

[17] Dang Z-M., Yuan J-K., Yao S-H., Liao R-J.: Flexible nanodielectric materials with high permittivity for power energy storage. Advanced Materials, **25**, 6334–6365 (2013).
DOI: 10.1002/adma.201301752

[18] Dang Z-M., Yuan J-K., Zha J-W., Zhou T., Li S-T., Hud G-H.: Fundamentals, processes and applications of high-permittivity polymer–matrix composites. Progress in Materials Science, **57**, 660–723 (2012).
DOI: 10.1016/j.pmatsci.2011.08.001

[19] Ramajo L., Reboredo M. M., Castro M. S.: BaTiO$_3$–epoxy composites for electronic applications. International Journal of Applied Ceramic Technology, **7**, 444–451 (2010).
DOI: 10.1111/j.1744-7402.2009.02473.x

[20] Patsidis A. C., Psarras G. C.: Structural transition, dielectric properties and functionality in epoxy resin-barium titanate nanocomposites. Smart Materials and Structures, **22**, 115006/1–115006/8 (2013).
DOI: 10.1088/0964-1726/22/11/115006

[21] Tantis I., Psarras G. C., Tasis D.: Functionalized graphene – poly(vinyl alcohol) nanocomposites: Physical and dielectric properties. Express Polymer Letters, **6**, 283–292 (2012).
DOI: 10.3144/expresspolymlett.2012.31

[22] Dang Z-M., Yu Y-F., Xu H-P., Bai J.: Study on microstructure and dielectric property of the BaTiO$_3$/epoxy resin composites. Composites Science and Technology, **68**, 171–177 (2008).
DOI: 10.1016/j.compscitech.2007.05.021

[23] Simitzis J., Zoumpoulakis L., Soulis S.: Effect of composition and polyesterification catalysts on the optical properties of cured polyesters. Polymer International, **51**, 297–307 (2002).
DOI: 10.1002/pi.825

[24] Simitzis J., Zoumpoulakis L., Soulis S.: DSC curing study of catalytically synthesized maleic-acid-based unsaturated polyesters. Polymer International, **51**, 308–318 (2002).
DOI: 10.1002/pi.832

[25] Simitzis J., Zoumpoulakis L., Soulis S.: Review of the research results concerning the synthesis, curing, structure and properties of unsaturated polyesters. Current Trends in Polymer Science, **8**, 107–125 (2003).

[26] Pomakis I., Simitzis I.: A new method to control the polyesterification process. Prospects of application in the production plants. Die Angewandte Makromolekulare Chemie, **99**, 145–170 (1981).
DOI: 10.1002/apmc.1981.050990113

[27] Orthmann H. J., Mair H. J.: Die Prūfung thermoplastischer Kunststoffe. Hanser, München (1971).

[28] Bürger A.: Kohlenstofffasern -Verstärker Polymere und deren Ehernischer. Abbaw bis zu Kohlenstoff-Verbund-werkstoffen (in German). PhD Thesis, Karlsruhe Institute of Technology (1973).

[29] Ioannou G., Patsidis A., Psarras G. C.: Dielectric and functional properties of polymer matrix/ZnO/BaTiO$_3$ hybrid composites. Composites Part A: Applied Science and Manufacturing, **41**, 104–110 (2011).
DOI: 10.1016/j.compositesa.2010.10.010

[30] Pant H. C., Patra M. K., Verma A., Vadera S. R., Kumar N.: Study of the dielectric properties of barium titanate–polymer composites. Acta Materialia, **54**, 3163–3169 (2006).
DOI: 10.1016/j.actamat.2006.02.031

[31] Yu C-R., Wu D-M., Liu Y., Qiao H., Yu Z-Z., Dasari A., Du X-S., Mai Y-W.: Electrical and dielectric properties of polypropylene nanocomposites based on carbon nanotubes and barium titanate nanoparticles. Composites Science and Technology, **71**, 1706–1712 (2011).
DOI: 10.1016/j.compscitech.2011.07.022

[32] Darwish A. G. A., Badr Y., El Shaarawy M., Shash N. M. H., Battisha I. K.: Influence of the Nd^{3+} ions content on the FTIR and the visible up-conversion luminescence properties of nano-structure BaTiO$_3$, prepared by sol–gel technique. Journal of Alloys and Compounds, **489**, 451–455 (2010).
DOI: 10.1016/j.jallcom.2009.09.021

[33] Tangwiwat S., Milne S. J.: Barium titanate sols prepared by a diol-based sol–gel route. Journal of Non-Crystalline Solids, **351**, 976–980 (2005).
DOI: 10.1016/j.jnoncrysol.2004.12.008

[34] Ghosh S., Dasgupta S., Sen A., Maiti H. S.: Synthesis of barium titanate nanopowder by a soft chemical process. Materials Letters, **61**, 538–541 (2007).
DOI: 10.1016/j.matlet.2006.05.006

[35] Skoog D. A., Holler F. J., Nieman T. A.: Principles in instrumental analysis. Kostarakis, Athens (2005).

[36] Valavanides Th.: Basic principles in molecular spectroscopy and applications in organic chemistrie. Sichrona Themata, Athens (2008).

[37] McMurry J.: Organic chemistry. Crete University Publications, Herakleion (2007).

[38] Atta A. M., Nassar I. F., Bedawy H. M.: Unsaturated polyester resins based on rosin maleic anhydride adduct as corrosion protections of steel. Reactive and Functional Polymers, **67**, 617–626 (2007).
DOI: 10.1016/j.reactfunctpolym.2007.04.001

[39] Abdallh M., Bakir E., Yousif E.: Study the electrical conductivity of crosslinked polyester doped with different metal salts. Journal of Saudi Chemical Society, in press (2014).
DOI: 10.1016/j.jscs.2011.08.001

[40] Cho L. L.: Identification of textile fiber by Raman microspectroscopy. Forensic Science Journal, **6**, 55–62 (2007).

[41] Oswal S. L., Pandya A. K.: Synthesis and characterization of linear aromatic polyester-amides from diacid chlorides and aminophenols. Iranian Polymer Journal, **13**, 205–212 (2004).

[42] Asimakopoulos I.: Synthesis and dielectric response of composite materials polymeric matrix-barium titanate nanoparticles. Diploma Thesis, Department of Materials Science, University of Patras, Greece (2010).

[43] Kalini A., Gatos K. G., Karahaliou P. K., Georga S. N., Krontiras C. A., Psarras G. C.: Probing the dielectric response of polyurethane/alumina nanocomposites. Journal of Polymer Science Part B: Polymer Physics, **48**, 2346–2354 (2010).
DOI: 10.1002/polb.22120

[44] Simitzis J.: Polymers. National Technical University of Athens Press, Athens (1994).

[45] Psarras G. C., Manolakaki E., Tsangaris G. M.: Dielectric dispersion and ac conductivity in – Iron particles loaded – polymer composites. Composites Part A: Applied Science and Manufacturing, **34**, 1187–1198 (2003).
DOI: 10.1016/j.compositesa.2003.08.002

[46] Psarras G. C., Manolakaki E., Tsangaris G. M.: Electrical relaxations in polymeric particulate composites of epoxy resin and metal particles. Composites Part A: Applied Science and Manufacturing, **33**, 375–384 (2002).
DOI: 10.1016/S1359-835X(01)00117-8

[47] Tsangaris G. M., Psarras G. C., Kouloumbi N.: Electric modulus and interfacial polarization in composite polymeric systems. Journal of Materials Science, **33**, 2027–2037 (1998).
DOI: 10.1023/A:1004398514901

[48] Kontos G. A., Soulintzis A. L., Karahaliou P. K., Psarras G. C., Georga S. N., Krontiras C. A., Pisanias M. N.: Electrical relaxation dynamics in TiO_2 – polymer matrix composites. Express Polymer Letters, **1**, 781–789 (2007).
DOI: 10.3144/expresspolymlett.2007.108

[49] Patsidis A. C., Kalaitzidou K., Psarras G. C.: Dielectric response, functionality and energy storage in epoxy nanocomposites: Barium titanate vs exfoliated graphite nanoplatelets. Materials Chemistry and Physics, **135**, 798–805 (2012).
DOI: 10.1016/j.matchemphys.2012.05.060

[50] Dang Z-M., Yuan J-K., Zha J-W., Zhou T., Li S-T., Hu G-H.: Fundamentals, processes and applications of high-permittivity polymer–matrix composites. Progress in Materials Science, **57**, 660–723 (2012).
DOI: 10.1016/j.pmatsci.2011.08.001

[51] Patsidis A., Psarras G. C.: Dielectric behaviour and functionality of polymer matrix – ceramic $BaTiO_3$ composites. Express Polymer Letters, **2**, 718–726 (2008).
DOI: 10.3144/expresspolymlett.2008.85

[52] Patsidis A. C., Kalaitzidou K., Psarras G. C.: Carbon or barium titanate reinforced epoxy resin nanocomposites: Dielectric, thermomechanical and functional behaviour. Journal of Advanced Physics, **2**, 7–12 (2013).
DOI: 10.1166/jap.2013.1040

[53] Mathioudakis G. N., Patsidis A. C., Psarras G. C.: Dynamic electrical thermal analysis on zinc oxide/epoxy resin nanodielectrics. Journal of Thermal Analysis and Calorimetry, **116**, 27–33 (2014).
DOI: 10.1007/s10973-013-3510-8